Verification and applications of surface waves extracted from ambient noise

By

Jun Xie

A thesis submitted to Macquarie University
for the degree of Doctor of Philosophy
Department of Earth and Planetary Sciences

Australian Research Council Centre of Excellence for
Core to Crust Fluid Systems (CCFS) and GEMOC

January 2017

Acknowledgements

First, I would like to express my sincere gratitude to my advisors Prof. Sidao Ni in USTC and Prof. Yingjie Yang in Macquarie University for their continuous support of my Ph.D study and related research. I would also like to appreciate their patience, motivation, and immense knowledge. Both of their guidance helped me in my research and thesis. Their advice on both research as well as career have been priceless. I could not have imagined having better advisors and mentors for my Ph.D study.

I thank my colleagues both in USTC and Macquarie University for several useful discussions, selfless and kindness they offered me and for all the fun we had during my graduate studies.

Words cannot express how grateful I am to my mother-in law, father-in-law, my mother, and father for all their sacrifices they made on my behalf. Their prayers for me has sustained me thus far. I would also like to thank all of my friends who supported me in writing, and encouraged me to strive towards my goal. At the end, I would like to express my sincere appreciation to my beloved wife Ruiting Li, who spent sleepless nights with me and was always there to support me in moments when there was no one to answer my queries.

For my baby angel.

List of Publications

- Xie, J., Y. Yang, S. Ni, *On the accuracy of Long period Rayleigh waves extracted from ambient noise.* Geophysical Journal International **206(1)**, 48-55. (2016)

- Xie, J., X. Zeng, W. Chen, and Z. Zhan *Comparison of ground truth location of earthquake from InSAR and from ambient seismic noise: A case study of the 1998 Zhangbei earthquake.* Earthq Sci **24(2)**, 239-247, doi:10.1007/s11589-010-0788-5. (2011)

- Xie, J., S. Ni, and X. Zeng *1D shear wave velocity structure of the shallow upper crust in central Sichuan Basin.* Earthq. Res. Sichuan, **143(2)**, 20-24. (2011, in Chinese)

- Li, G., H. Chen, F. Niu, Z. Guo, Y. Yang, and J. Xie *Measurement of Rayleigh wave ellipticity and its application to the joint inversion of high-resolution S-wave velocity structure beneath northeast China.* J. Geophys. Res. Solid Earth, **121**, doi:10.1002/2015JB012459 (2016)

- Zeng, X., J. Xie, and S. Ni *Ground Truth Location of Earthquakes by Use of Ambient Seismic Noise From a Sparse Seismic Network: A Case Study in Western Australia.* Pure and Applied Geophysics **172(6)**, 1397-1407, doi:10.1007/s00024-014-0993-6. (2015)

- Xia, Y., S. Ni, X. Zeng, J. Xie, B. Wang, and S. Yuan *Synchronizing Intercontinental Seismic Networks Using the 26 s Persistent Localized Microseismic Source.* Bulletin of the Seismological Society of America doi:10.1785/0120140252. (2015)

- Bao, F., S. Ni, J. Xie, X. Zeng, Z. Li, and Z. Li *Validating Accuracy of Rayleigh-Wave Dispersion Extracted from Ambient Seismic Noise Via Comparison with Data from a Ground-Truth Earthquake.* Bulletin of the Seismological Society of America **104(4)**, doi:10.1785/0120130279. (2014) %Thesis Author Contributions: Concept (50%); Data collection (50%); Analysis (50%); Writing (20%).

- Bao, F., S. Ni., J. Zheng, J. Xie, W. Chen, and X. Zeng *Accurate earthquake location with instrumental clock error: A case study for the 19 January 2011 Anqing earthquake sequence.* Acta Seismologica Sinica, **35(2)**,10.3969/j.issn.0253-3782.2013.02.003. (2013, in Chinese)

- Lü, Y., S. Ni, J. Xie, Y. Xia, X. Zeng, and B. Liu *Crustal S-wave velocity structure of the Yellowstone region using a seismic ambient noise method.* Earthq Sci, **26(5)**, 283-291, doi:10.1007/s11589-013-0016-1. (2013)

- Chen, W., S. Ni, S. Wei, Z. Wang, and J. Xie *Effects of sedimentary layer on earthquake source modelling from geodetic inversion.* Earthq Sci, **24(2)**, 221-227, doi:10.1007/s11589-010-0786-7. (2011)

- Luo, Y., S. Ni, X. Zeng, J. Xie, Y. Chen, and F. Long *he M5.0 Suining-Tongnan (China) earthquake of 31 January 2010: A destructive earthquake occurring in sedimentary cover.* Chin. Sci. Bull., **56(6)**, 521-525, doi:10.1007/s11434-010-4276-2. (2011)

Abstract

About a decade ago, it was shown that Empirical Green's Function (EGF) between two seismic stations can be extracted from cross-correlation of ambient seismic noise. Since then, studies based on ambient noise have become a method of choice among seismologists. Noise Cross-correlation Function (NCF) has been widely used for seismic tomography (known as ANT), monitoring velocity changes, calibrating earthquake location, and so on. Almost all of these studies are based on the assumption that accurate EGF can be extracted from cross-correlations of ambient noise. However, uncertainties of the dispersion measurements from ambient noise are still not clear. It is also not certain whether surface waves at periods longer than 50 s can be extracted from ambient noise recorded at portable seismic stations or whether the resulting dispersion measurements from ambient noise are accurate enough to image lithosphere and asthenosphere structures. This thesis is to address these questions.

I investigate the accuracy of surface wave dispersion curves at both short (10-30 s) and long (50-250 s) periods from ambient noise. By comparing the waveforms and dispersion curves from ambient noise with those from earthquake data, I demonstrate that the dispersion measurements from surface waves extracted from ambient noise are as accurate as those from earthquake data. The dispersion measurements can be used in ambient noise tomography to provide complementary data, which can be used to constrain the lithospheric and asthenospheric structures.

Furthermore, I demonstrate that broadband surface waves at 10-150 s period from ambient noise can be used to construct the 3D shear wave velocity structure from the surface down to 300 km depth in the USA. I calculate NCFs among all the USAarray stations in

US continent and extract broadband (10-150 s) Rayleigh wave phase velocities, and obtain phase velocity maps by inverting the broadband dispersion curves. Then, I build a new 3D shear wave velocity model of the lithosphere and asthenosphere structure by inverting the resulting phase velocity maps.

Finally, I demonstrate that using EGFs from ambient noise, we can improve earthquake location and locate recorded historical earthquakes. Using a seismic array in central Australia, I test the accuracy of our location method using ambient noise. I find that, when the distribution of the remote station is good and the reference station is located less than 20 km away from the source, the location error is less than 2 km. I conclude that this method can be used to obtain ground truth event with location error equal or smaller than 2 km (GT2) in regions with sparsely distributed remote stations.

Declaration

I certify that the work in this thesis entitled "**Verification and applications of surface waves extracted from ambient noise**"has not previously been submitted for a degree, nor has it been submitted as partial requirement for a degree to any other university or institution other than Macquarie University.

I also verify that this thesis is an original piece of research and has been written by me. Any help and assistance that I have received in my research work and the preparation of the thesis itself have been properly acknowledged.

In addition, I certify that all data, information sources and literature used are indicated in the thesis.

Jun Xie

Student ID: 43511155

January 6, 2017

Contents

Acknowledgements **iii**

List of Publications **v**

Abstract **vii**

Declaration **ix**

List of Figures **xv**

List of Tables **xxv**

1 Introduction **1**

1.1 History of research on the characteristics and sources of ambient noise 3

1.2 The review of applications of ambient noise in seismology 9

1.3 Thesis objectives 11

1.4 Structure of this thesis 12

2 Extracting EGF from ambient noise **13**

2.1 Cross-correlation of ambient noise 14

2.2 Single station preparation 15

2.3 Temporal stacking 16

2.4 Waveform distortion caused by nonlinear stacking 18

2.5 Conclusion 30

3 Validating accuracy of Rayleigh wave dispersion extracted from ambient seismic noise via comparison with data from a Ground-Truth earthquake 33

3.1 Abstract 33

3.2 Introduction 34

3.3 Data 35

3.4 Results 38

3.5 Discussion 42

3.6 conclusion 47

4 On the accuracy of long-period Rayleigh waves extracted from ambient noise 49

4.1 Summary 49

4.2 Introduction 50

4.3 Double difference between real, theoretical earthquake data and EGF, theoretical Greens function 52

4.4 Phase velocity comparison between Earthquakes and NCFs for global data set 56

4.5 Phase velocity comparison between earthquakes and CCFs on regional scale 62

4.6 Conclusion 64

5 3D shear wave velocity model of US continent constructed from broadband ambient noise tomography 65

5.1 Abstract 65

5.2 Introduction 66

5.3 Data 68

5.4 Method of tomography 73

5.5 Phase velocity maps 76

5.6 3D shear model construction 81

  5.6.1 Model Parameterization 81

  5.6.2 Inversion scheme 83

5.7 3D Vs model and discussion 85
5.8 Conclusion 89

6 Accuracy of earthquake location based on group travel time of surface wave from ambient noise 93
6.1 Summery 93
6.2 Introduction 94
6.3 Calibration of earthquake based on ambient Noise Cross-correlation Function 96
6.4 Accuracy of earthquake location using travel time-based method and its relationship with the distance of the reference station 98
6.5 Conclusion 104

7 Conclusion 107

References 111

List of Figures

2.1 Synthetic vertical Green's Functions (GFs). GF is calculated using CPS (Herrmann & Ammon, 2002) based on 1D PREM model (Dziewonski & Anderson, 1981). Waveforms 2-4 are the Green's functions contaminated by different types of noise, and the amplitude of the noise is 50% of the GF. NN is the normal noise; AM is the noise recorded by stations of the networks of TA, II, IU, CI and US in Jan 1th, 2012 and CO is the corresponding random coda of all NCFs on that day. 19

2.2 The diagram of multiple filter technique analysis for the synthetic GF. The original GF was bandpass filtered in period bands of 5-10 s and 10-20 s, before they are added. 19

2.3 The recovered waveforms based on Time domain Linear stacking method (TL). The noise type of (a), (b) and (c) are NN, AM and CO, respectively. The black curve is the target waveform (GF), and the red curves are the recovered waveforms using 100 contaminated waveforms. The percentages shown in the figure represent the ratio between the maximum amplitude of the noise and the maximum amplitude of the GF. 20

2.4 Similar to Figure 2.3, but based on PWS stacking method. 21

2.5 Similar to Figure 2.3, but based on tf_PWS stacking method. 21

2.6 Dispersion curves extracted from the waveforms from Figure 2.3. The fast and slow velocities represent the phase velocity and group velocities, respectively. The black curve is the dispersion curve extracted from GF. It is clear the phase velocity extracted from the recovered waveform is more accurate than the group velocity. 22

2.7 Dispersion curves extracted from the waveforms from Figure 2.4. Phase velocity slower than the group velocity is due to the cycle skipping. It indicates that when the amplitude of the noise is large (50% and 100%), the waveform can not be well recovered. 23

2.8 Dispersion curves extracted from the waveforms from Figure 2.5. The dispersion curves are stable and close to the synthetics. However at the long period (>35 s), the dispersion curves show systematic discrepancies with the synthetics. 24

2.9 Comparisons of the dispersion curves resulted from the three stacking methods (TL, PWS and tf_PWS). The contaminated noise is CO, and the amplitude is 100% with respect to the GF. 600 traces are used during the stacking. See the text for detailed information. 25

2.10 An example of the NCF (between 221A/TA and SCIA/US) comparison between that from tf_PWS and TL. The interstation distance is 1695.3 km. The red curves are the results of TL and the black curves are from tf_PWS. Comparisons here include waveforms at different periods (left diagram), phases, SNR, phase velocity and traveltimes, respectively. See the text for detailed information. 26

2.11 The surface wave phase velocity difference of the NCFs between that from tf_PWS and TL. The NCFs used here are from the USArray (See Chapter 5). Positive value here means the phase velocity of NCF based on tf_PWS is larger than that from TL. a, b, c and d are the phase velocity difference for periods of 20, 30, 50 and 100 s, respectively. 27

2.12 Phase velocity difference (Figure 2.11) versus the period. The error bar is the standard error of the phase velocity difference at each period. 28

2.13 The NCF waveforms time shift between that from tf_PWS and TL, and the time shifts are measured by MWCS (left) and FTAN (right), respectively. During the time shift measurement, NCF waveforms are bandpass filtered with a narrow filter window centred in 40 s. The mean and standard error are calculated and shown in the upper left corner. Number of the measurements is 30703, with cross-correlation coefficient bigger than 0.98. Positive value here means the surface wave of NCF from tf_PWS travels faster than that from TL. 29

2.14 Surface waveform time shifts at 40 s for NCF pairs (calculated from tf_PWS and TL), which are measured by FTAN (X-axis) and MWCS (Y-axis), respectively. The points taken those two measurements as coordinates lie around the diagonal line, indicating that those two measurement is consistent with each other. 30

3.1 The location of earthquake (black triangle in the center of the circle) occurred in Suining, Sichuan province (M4.8, Jan. 30 th, 2010) and the distribution of the stations used in our research. The blank circle denotes the distance of 1000 km away from the earthquake. Right column shows the NCFs between ZHB with other stations in the period band 10-30 s. 37

3.2 (Left) Noise correlation functions and surface-wave records at far stations (>1000 km) for stations AAK, KURK, TATO, and HKPS (from top to bottom). (Right) Rayleigh-wave group velocity dispersion curves measured from earthquake data (solid line), symmetric (starred lines), and one-sided (dashed lines) NCFs for the same four stations. 39

3.3 (Left) Noise correlation functions and surface-wave records at near stations (<1000 km) for stations XAN, ENH, and KMI (from top to bottom); interstation distances are 516, 367, and 641 km, respectively. (Right) Rayleigh-wave group velocity dispersion curves measured from earthquake data (solid line), symmetric (starred lines), and one-sided (dashed lines) NCFs for the same three stations. 40

3.4 Comparison of group velocity dispersion between earthquake data (solid) and NCFs (dashed line, the stronger branch of onesided NCFs; starred line, symmetric NCFs). (a) NCFs are retrieved from normalized noise with the time-domain running-average method (Bensen *et al.* , 2007). (b) NCFs are retrieved from noise data without the time-domain running-average method. 42

3.5 (a) Group velocity dispersion curves from earthquake data (black) and from the NCF between stations SNI and AAK for different time spans (red, symmetric NCF from the whole 15 months of noise data; green, symmetric NCFs from six months of noise data; blue, symmetric NCF from three months of noise data). (b) Same as (a), but for the station pair SNI-ENH. 43

3.6 Group velocity difference between synthetic double couple source at difference depth and single force applying at the surface of the centroid of the earthquake. The distance of the station is 359 km (same as the distance between the earthquake and station ENH). 44

3.7 Mismatch of group velocity dispersion between earthquake and noise data versus SNR of the noise correlation function (NCF). "Mismatch" is defined as the standard deviation of the difference between the dispersions for the whole band (10-30 s). The label in each panel (RAM or notRAM, REV or notREV) denotes whether running average method is applied in time domain normalization and whether symmetric NCFs (REV) or one-sided NCFs (notREV) are involved. 45

3.8 Comparison of phase velocity dispersion between earthquake data after correction for focal depth (black solid line for depth of 0.6 km and red line for depth of 2.0 km) and NCFs (dashed line for the stronger branch of one-sided NCF, and starred line for symmetric NCF) at station ENH. The phase velocity dispersion from earthquake data was calibrated for effects due to earthquake focal mechanism and focal depth. 46

4.1 Distribution of the stations (black triangles) and events (red stars). The blue star is the L'Aquila earthquake occurred in Italy at April 6th, 2009. Actually there are a lot of station and event pairs in Ekström (2011) which are 100 km close with each other 100 km and some stations are 100 km close, here we only retain the closest station-event pairs to minimise the bias. 51

4.2 Examples of waveform comparisons between observed earthquake data (6th April 2009 Mw 6.3 L'Aquila earthquake), synthetic seismograms (column 1 and 3) and EGF from CCFs, synthetic EGFs (surface load of vertical single force simulations) (column 2 and 4), respectively. The synthetic waveforms using SEM are shown with red lines , and observed data withblack lines. All the waveforms are band-pass filtered in period band between 50-300 sec. The distances (in degree) are showing in the left bottom corner. The time shifts in the upper right corner are calculated based on cross-correlation, and the cross-correlation coefficients are in the right bottom corner. 55

4.3 The time shifts of the earthquake Rayleigh waves versus Greens Functions (Figure 4.2). To guarantee the quality of data, only cross-correlation coefficient bigger than 0.85 are retained. 56

4.4 CCFs between station II/TLY and other GSN stations. The waveforms are band-pass filtered in period band of 50-100sec, 100-200sec and 200-300sec respectively. The surface wave is obvious on both negative lags and positive lags and shows almost symmetric amplitude. 59

4.5 The left column shows the phase velocity difference between earthquake measurements (Ekström, 2011) (V_eq) and NCFs (V_ccf) for period from 75 s to 250 s. The middle column shows the phase velocity difference between earthquake measurements and prediction (V_pred) using program GDM52 (Ekström, 2011). The right column is the phase velocity dispersion difference between V_ccf and V_pred. The outliers with difference greater than 3% are discarded due to unrelated Gaussian distribution. It demonstrates that the phase velocity dispersion curves from NCF are very close with the phase velocity from earthquakes with the difference around 0.1%. 60

4.6 The Rayleigh wave phase velocity differences between the measurements from two-station method (Foster *et al.* , 2014) and NCFs of the western United States. Positive value indicates that the phase velocity from two-station method is faster than that from NCFs. (a) (b) (c) (d) are for periods of 50 sec, 60 sec, 75 sec and 100 sec respectively. 63

5.1 (a) The distribution of 1895 stations in US used in this study from USArray Transportable array stations (black triangle) and some other reference stations (red triangle). (b) Major geological units of Unite States modified from Fenneman (1917): Great Plain (GP), South Rocky Mountain (SRM), Basin and Range (BR), Yellowstone (YS), Rio Grande Rift (RGR), Central Valley (CV), Atlantic Coastal Plain (ACP), and Snake River Plain (SRP). Major sedimentary basins: Columbia River Sub-Flood Basalt sedimentary (CRFB), Anadarko Basin (AB), Denver Basin (DB), Green River Basin (GRB), Michigan Basin (MB), Mississippi Embayment (ME), Colorado Plateau and (CP). 69

5.2 An example of the NCFs between station ADO/CI and other stations. The NCFs are bandpass filtered between 50-100 s (left) and 100-200 s (right), respectively. The surface wave is clearly seen in both the positive and negative component, and the velocity of the surface wave is within the range of 3.0 km/s-4.5 km/s. 70

5.3 The phase travel time surface for the 50 s period surface wave centered at station NEW/US (blue star). (a) is the result before applying the SNR criteria; (b) is the result after performing 2π cycle skipping correction. 71

5.4 The ray path coverage at periods of 10, 50, 100 and 150 s, with a grid size of $1° \times 1°$. The central and western US have denser ray coverage than that in the eastern part. 72

5.5 Numbers of phase velocity measurements for each period. The black line is the number after the selection based on the SNR and inter-station distance, and the red line is the number of measurements after performing cycle skipping corrections. 72

5.6 The 40 s (top left) and 100 s (top right) Rayleigh wave phase velocity sensitivity kernels in 2D. TA.117A is the virtual source (white star) and TA.B17A is the receiver (white triangle). The reference velocities are 3.87 km/s and 4.08 km/s at 40 s and 100 s periods, respectively. The sensitivities along profiles delineated by the bold lines in the top panels are shown in the bottom panels. 74

5.7 Phase velocity maps at periods from 10 to 40 s. The first column is our result based on ray theory tomography method; The second is from Ekström (2014), which is also constructed using ambient noise data; the third column is the difference between this two data sets; the fourth column is the statistical distribution of the difference with the mean and standard deviations showing on the top left corner. 77

5.8 Phase velocity maps at periods from 50 to 90 s. The first column is our result based on finite frequency tomography method; the second is from Shen *et al.* (2013), and they have extend the result to the east of US (personal conmunication), which is Helmholtz tomography based on earthquake data; the third column is the difference between this two data sets; the fourth column is the statistical distribution of the differences with the mean and standard deviations showing on the top left corner. 78

5.9 Phase velocity maps at periods from 100 to 150 s. 79

5.10 The standard error of the tomography at periods of 50, 80, 110 and 150 s respectively. The standard error at 150 s is larger than that of other periods which is probably due to much sparser ray coverage at this period. 80

5.11 Recovered checkerboard models using finite frequency tomography. The left column is for 50 s period , and the right is for 100 s period. The size of the alternatively high and low velocity cells in the top and bottom figures is 2° × 2° and 1° × 1°, respectively. 81

5.12 Phase velocity depth sensitivity kernels of V_{sv} (black curves), V_p (red curves) and ρ (green curves) at different periods of (a) 10 s, (b) 50 s, (c) 100 s, (d) 150 s. 82

5.13 (a) The 1D velocity profile at (-120°, 30°) resulted from the probabilistic inversion method of MCMC. The reference model at this point below 200 km is from Schaeffer & Lebedev (2014). (b)-(j) are posteriori post distribution of the 9 B-spline parameters. We use the mean value of each parameter as the reference value. 84

5.14 Comparison of our shear wave velocities at the depth of 15 km with the models of USB2009 (Bensen *et al.* , 2009), USS2015 (Schmandt *et al.* , 2015) and USP2016 (Porter *et al.* , 2016). 86

5.15 The distribution of shear wave velocities at the depth of 80 km (similar to Figure 5.14). 87

5.16 Shear wave velocity maps at depths of 10, 25, 50, 100, 150 and 250 km respectively. The color represents velocity perturbations respect to the mean of each depth, which is labeled in the bottom. 88

5.17 Vertical cross sections across the US continent along with the Moho depth distribution from our MCMC inversion. 89

5.18 Vertical cross sections along and across the Yellowstone-Snake River Plain along with the Moho depth distribution from our MCMC inversion. 90

6.1 The distribution of the small seismic array in Australia used in this study. This so-called Warramunga array has 24 stations, which are located to the centre of the continent. The 12 remote stations used here have a distance of about 800 km away from the array. 99

6.2 NCFs between COEN and the stations of the array. The waveforms are bandpass filtered in the period bands of 10-30 s. The negative time lag of the NCF represents the signal traveling from COEN to the array. Since the COEN is close to the coastline, the main energy is from COEN to the array. Thus the amplitude in the negative lag is stronger than that of the positive lag. . . . 100

6.3 Group velocity dispersion curves computed from all symmetrical components of the NCFs in Figure 6.2 using FTAN (Bensen *et al.* , 2007). 101

6.4 Location of WB1 (blue star) when taking WB0 (black triangular) as the reference station and using all of the 12 remote stations. Black star is the real location of WB1. REF is the distance between WB0 and WB1, and ERR is the location error, which is ∼0.42 km. 101
6.5 The relation between the distance of the reference station and the location error. The horizontal axis is the distance between the reference station and the target station, and vertical axis is the location error. All of the remote stations are used (Figure 5.2) for the locating. The mean of the location error is 1.42 km and the standard error is 0.81 km. When calculating the mean and standard deviation, the station WB7, WB2 and WR8 are included, meaning that the real mean and standard error should be smaller. 102
6.6 The same as Figure 6.5, but with only four remote stations: KNRA, COEN, WRKA and INKA. The four remote stations are evenly distributed in four directions of the small array. 103
6.7 The same as Figure 6.5 but with only three stations: FITZ, COEN and INKA. 103
6.8 Location of WB1 (blue star) when taking WR9 (black triangular) as the reference station and using only two remote stations of WRKA and INKA. . 104

List of Tables

3.1 Source Parameters of the Suining Earthquake. 36

4.1 27 stations and events information. 56

1

Introduction

Seismology is the scientific study of earthquakes and the propagation of seismic waves within the solid earth. One of the major tasks in seismology is to use seismic waves to image the interior of the Earth. When seismic waves propagate through the Earth, they cause ground motions that can be recorded by seismometers on the Earth's surface. The ground motions recorded by seismometers are the seismic data, which seismologists use to image the Earth's interior.

There are mainly two groups of natural sources which can cause ground motions. The first group is related to energetic sources, such as earthquakes, volcano eruptions, and large storms. These energetic sources generate large ground motions that can be visualized as clear signals on seismograms, and are used in traditional seismology. The other group is related to much weaker sources, such as ocean waves and human activities, which do not generate standout signals and cannot been identified individually on seismograms. These weak ground motions which are known as ambient seismic noise are mainly characterised by high frequency energy. Ambient noise is usually considered useless in traditional seismology compared to the large amplitude signals from earthquakes. Through years of research, seismologists have found that ambient seismic noise actually carries useful information of the Earth's interior. Under the assumption that ambient noise is diffuse or its sources are spatially uniformly distributed, it is now generally believed that Empirical Green's Functions (EGF) between a pair of stations can be extracted by cross-correlating ambient noise data recorded by this station-pair.

Studies of ambient noise can be divided into two categories. The first one is studying the characteristics and distributions of ambient noise sources, and the second is using EGFs from ambient seismic noise to image the subsurface structures of the Earth. Understanding the characteristics and distributions of ambient noise sources can help to extract accurate EGFs from ambient noise. Besides, it can also help to better understand the interaction of the ocean and the atmosphere with the solid earth because the dominant ambient noise is caused by ocean waves, storms and meteorological fluctuations.

Studies using ambient noise to image the Earth's structure have become popular since it was found that EGF between two stations can be extracted from ambient Noise Cross-correlation Functions (NCFs). EGF from ambient noise is dominated by surface waves, thus most researches have been focusing on the extraction of surface wave dispersion curves from ambient noise. However, the accuracy of surface wave dispersion curves from NCFs still remains unclear. Therefore, one of the main focuses of this thesis is to evaluate the accuracy of the surface wave dispersion curves from NCF. After exploring and verifying the accuracy of broadband surface waves from ambient noise, I demonstrate that broadband surface waves at periods of 10 to 150 s can be extracted from portable seismic arrays such as the USArray and used to invert for structures from the free surface down to about 250-300 km depth. In addition, I demonstrate that earthquake location based on dispersion measurements from ambient noise can achieve an accuracy of $\sim$2 km.

1.1 History of research on the characteristics and sources of ambient noise

The study of ambient noise dates back to the very beginning of the modern seismology in the 19th century. Gutenberg is probably the first scientist who pioneered the research on ambient noise (Bonnefoy-Claudet *et al.* , 2006; Gutenberg, 1911). However, it is not until the middle of the 20th century that research on ambient noise gradually changed from qualitative description to quantitative analysis. The review paper of Gutenberg (1958) concluded that seismic noise in the frequency band of 0.05-0.1 Hz is mainly generated by ocean waves interacting with the coast line. Seismic noise of 0.1-0.25 Hz originates from meteorological fluctuation, those of 2-10 Hz are microseism of volcanos and those of 1-100 Hz are from human activities. In 1978, Asten (1978) drew a similar conclusion, but he proposed that the energy generated by oceanic waves striking the coastlines is dominated by frequencies of 0.5-1.2 Hz and the highest frequency of the urban noise is 30 Hz. The review paper of Bonnefoy-Claudet *et al.* (2006) suggested that ambient seismic noise with frequencies lower than 0.5 Hz originates from ocean waves and large-scale meteorological conditions, whereas ambient noise at frequencies around 1 Hz is caused by wind effects and local meteorological conditions. At frequencies above 1 Hz, ambient seismic noise is attributed to human activities.

All the above papers have demonstrated that ambient noise is mainly generated by two types of sources: One is related to human activities in high frequency band, recognised as microtremor; and the other is associated with natural sources of energy concentrated in the low frequency band, usually called the microseism. The dividing frequency of these two types of ambient noise sources is roughly 1 Hz.

Studies of microtremor dates back to the 1960s. Kanai (1961) first observed the microtremor in Tokyo, Japan using 30 seismic stations. He found that the daily and weekly energy variations in the microtremor band are related to human activities. The energy in the daytime is stronger than that at night, and they derived an empirical amplitude relationship between daytime and nighttime. Frantti *et al.* (1962) and Frantti (1963) studied high frequency ambient noise recorded by 48 seismic stations in the USA. They found that energy at frequencies of 0.6-1 Hz is weaker than that at higher frequencies, and ambient noise with frequency higher than 1 Hz shows stable features, but the absolute noise level varies from site to site. They also found that the high frequency ambient noise is usually correlated with human activities. Similar characteristics for microtremor were also found by Peterson (1993), Stutzmann *et al.* (2000) and Berger *et al.* (2004).

Gutenberg (1931) observed microseism signals using seismographs deployed in Europe and North America, thereby pioneering the research of ambient noise in the frequency band of microseism. It was found that the microseism becomes stronger for stations closer to the coastlines and the storms occurring inland have nothing to do with the strength of microseism. However, when the storm reaches the coastlines, the microseism is significantly enhanced. They further demonstrated that the microseism is neither from the atmosphere nor from the storm, but generated by the interaction between the storm and the steep solid coast. In contrast, Whipple & Lee (1935) found that the microseism is not generated by the storm striking the coast but in the centre of the storm in the ocean. Ramirez (1940) used a triangular array to study the microseism in St Louis, Missouri, and confirmed that the microseism is from the coast of the East Atlantic. His method for locating the source of microseism was improved by Gilmore (1946) who used it to track the hurricane in the Caribbean (Gilmore, 1946).

In the 1940s and 1950s a large number of observations indicated the close relationship between the microseism and ocean wave heights. This advanced the theory of microseism generation mechanism. The most intuitive generation theory of the microseism, which is also considered as the most probable explanation, is that the microseism comes from the pressure variation on the seabed caused by the undulation of ocean waves. However, this theory is not completely right because the wave propagation theory explains that the pressure generated by ocean wave decreases with depth exponentially. Thus it cannot explain the strong intensity of the microseism. Another problem is that some observations indicated that some energy of the microseism has a dominant frequency that is twice that of the ocean waves. For example, Haubrich *et al.* (1963) observed two peaks in the spectrum of microseism recorded in San Diego, California, with one peak having half frequency of the other peak but being 100 times stronger in amplitude than the other. They concluded that the low frequency microseism originated from the vicinity of the coast line, whereas the primary frequency component is from shallow water.

Based on previous observations and studies, Longuet-Higgins (1950) refined the theory of the microseism generation. He proposed that the microseism at the period band of 5-10 s is generated by the interaction between two groups of ocean waves with the same wavelength but travelling in opposite directions. Thus, the frequency of this microseism is twice that of the ocean waves, and the energy is proportional to the height of the ocean waves. The theory proposed by Longuet-Higgins (1950) became the fundamental theory for later-stage microseism studies, e.g., Kedar *et al.* (2008) successully used this theory to predict the timing and amplitudes of ground displacements generated by deep ocean wave-wave interaction in the North Atlantic.

Peterson (1993) studied the spectrum of the microseism using 75 global stations. During their data processing, the noise of the seismometer, irregular vibrations and earthquakes were all removed. They calculated the Power Spectral Density (PSD) of each station. It is clear in the PSDs that there are three peaks within three different bands: >1000 s, 1-20 s and <1 s. The long period noise correlated with large-scale meteorological fluctuation. He proposed a new ambient seismic noise model based on that. They defined the upper and lower bounds of the PSD curves as the Earth's New High ambient Noise Model (NHNM) and the New Low Noise Model (NLNM), respectively. They also thought the microseism is generated by the interaction between ocean waves and the coastline. The microseism at periods of 10-20 s is called the primary microseism and its period is similar to the global ocean waves. For this study, the microseism at periods of 5-10 s is called the secondary microseism, which is also thought to be generated by the interaction between two ocean waves traveling in opposite directions. They also found that the energy of the horizontal component is much stronger than that of the vertical component (Peterson, 1993).

Friedrich *et al.* (1998) located the source of microseism using frequency-wavenumber method, which provided direct evidence to support the theory that microseism is generated from the interaction between ocean waves and coastlines. Some subsequent studies also gave more observational evidence. For example, McNamara & Buland (2004) used the stations from U.S. National Seismograph Network and Advanced National Seismic System to study the ambient noise level of U.S. continent. They calculated the Probability Density Functions (PDFs) and analyzed them statistically. They also analyzed the microseism in U.S. continent and found there are seasonal variations in the strength of the microseisms.

Ardhuin *et al.* (2011) performed the first comprehensive numerical model of microseismic generations. They clustered the noise generation events into three classes: wind waves, sea states with contribution of coastal reflections and interaction of two dependent waves. They suggested the secondary sources are associated with shoreline reflections, indicating the mechanism of the generation of secondary microseism is coastal reflections. The following numerical modeling showed that the opposite-propagating wave trains is a significant source of microsisms for period shorter than 13 s. Waves propagating over a sloping ocean bottom can generate the microseism from 13 to 300 s (Ardhuin & Herbers, 2013; Ardhuin *et al.* , 2015).

Stehly *et al.* (2006) were the first to use NCFs to study the source of microseism. Their analyses are based on the fact that uneven distribution of noise sources lead to asymmetry in the amplitude of the positive and negative time lags of NCF. Based on this, Stehly *et al.* (2006) used many seismic arrays in U.S. and Europe to locate the source of microseism. They found that, during the summer of the northern hemisphere, the main source of the microseism is located in the north Atlantic Ocean and, during the Northern Hemisphere winter, most of the noise originates from the southern Indian Ocean and the southern Pacific. It is clear from this study that the sources of microseism are seasonally variable.

Yang & Ritzwoller (2008) also studied the sources of microseism based on NCF. They located the sources of the primary and secondary miscroseism using the seismic arrays at Europe, Africa and America. Different from Stehly *et al.* (2006), Yang & Ritzwoller (2008) suggested that the primary and secondary microseism are both generated by the nonlinear interactions between the sea waves and the seabed near the coast line. They also found that the ambient noise at periods longer than 20 s does not show seasonal variations both in amplitude and directivity.

Ambient seismic noise at periods longer than 50 s, i.e, 2-20 mHz, is typically called Earth's Hum, and can be observed across the globe in both vertical and horizontal components (Nishida, 2013). The mechanism of Earth's Hum generation is thought to be totally different from that of the microseism. The Earth's Hum is suggested to be generated by the infragravity waves, which is the result of the interaction between the atmosphere, the ocean and the continent (Kobayashi & Nishida, 1998; Nawa *et al.* , 1998; Nishida, 2013; Nishida *et al.* , 2000; Roult & Crawford, 2000; Suda *et al.* , 1998; Tanimoto, 2005; Webb, 2007, 2008).

The observation and studies of the Earth's Hum came later than those of the microseism. Nawa *et al.* (1998) first observed the incessant excitation of the Earth's free oscillations, which are mainly the fundamental spheroidal modes in the frequency range of 0.3-5 mHz (Nawa *et al.* , 1998). They did some synthetic tests based on the assumption that the oscillation results from a bunch of earthquakes. However, their synthetic results are inconsistent with the observations, which indicates that the long-lasting free oscillations are generated by other sources rather than the earthquakes. Traditionally, the free oscillation was thought to be generated by big earthquakes. Suda *et al.* (1998) found that the free oscillation can also be observed in times when there are no large earthquakes. Their synthetic test also implied that the free oscillation is not from the summation of small earthquakes. Nishida *et al.* (2000) found seasonal variation of this free oscillation, and he first introduced the term "Hum" to describe the oscillation. His observation indicated that the source of this hum is not inside the solid earth. Some other observation found that the resonance between the atmosphere and the solid earth is overlapping in the period band of the Hum (e.g., Fukao *et al.* , 2010; Rhie & Romanowicz, 2004, 2006; Webb, 2007, 2008). These studies suggested that the hum is generated by sources on the surface of the Earth. Rhie & Romanowicz (2004) found that the energy of the Earth's Hum is similar to that from an earthquake with magnitude of 5.75 to 6, and the Hum was also located in the ocean. They also found that, during the winter of the Northern Hemisphere the original sources of the hum are in the northern ocean, whereas during the summer of the northern hemisphere, they are in the southern oceans. All of these observations demonstrated that the hum is also unevenly distributed both in time and space.

Apart from the ubiquitous ambient noises described above, there are also some localized ambient noise sources. These localized noise sources have fixed locations and are confined to a small region. For example, Shapiro *et al.* (2006) observed a 26 s microseism signal in the global seismic stations and its source is located in the Gulf of Guinea. Xia *et al.*

(2013) confirmed that there are two persistent signals originating from the Gulf of Guinea. Zeng & Ni (2010) observed a persistently localized microseismic source near the Kyushu Island within the period band of 0.07-0.12 Hz. The generation mechanisms of these localized ambient noise sources are still not completely understood, but usually are considered to be related with the microseisms of volcanoes.

Research on the origin and composition of ambient noise is still ongoing. The sources of the ambient noise are usually correlated with ocean waves, and ambient noise is mainly composed of surface wave energy. Lee (1932) observed Rayleigh waves in the microseism at periods from a few seconds up to 10 s. In addition, there is also body wave energy in ambient noise. Backus *et al.* (1964) studied the ambient noise in the frequency band of 0.5-5 Hz and found surface waves propagating with a velocity of 3.5 to 4.5 km/s. They also found there are body waves signals in this frequency band. Yamamoto (2000) showed that microtremor energy is composed of 50% Love wave in the frequency band of 1 to 10 Hz, whereas the percentage of Rayleigh wave is relatively small. Fukao *et al.* (2010) found that the noise sources at the surface of the Earth can produce body waves in the microseism band. Koper *et al.* (2010) studied the ambient noise in the frequency of 0.4-4 Hz, and found that the dominant composition of ambient noise is Love wave (50%), the second largest component is P wave (28%), and Rayleigh wave is the least significant component. The composition studies of the ambient noise varies from one study to another due to the differences of seismic arrays, frequency bands and the data processing methods used in respective studies. In summary, it is important to study the composition of ambient noise, because it can help us understand the source mechanism of the ambient noise, which benefits the extraction of EGFs from ambient noise.

There are a large number of published papers on the studies of ambient noise, and a lot of the early works were published in German, Italian and Japanese languages. Therefore, our review of the history of ambient noise research cannot cover all of those articles. People know little about the source and characteristics of ambient noise in the early stage. With more and more advanced modern seismographs deployed around the world, our understanding of the characteristics and sources of ambient noise becomes clearer and clearer. To date, studies of noise source characteristics reduce gradually, while the research on the application of ambient noise in seismology becomes more prominent.

1.2 The review of applications of ambient noise in seismology

Applications of ambient noise based on array techniques were first developed by Aki (1957), who found that surface wave dispersion curves can be extracted through spatial cross-correlation of ambient noise data recorded among several close seismic stations. He then developed the SPatial Auto-Correlation (SPAC) method to infer velocity structures beneath a seismic array (e.g., Bettig *et al.* , 2001).

Claerbout (1968) extended the research into ambient noise cross correlations. His work confirmed that the autocorrelation of the transmission response of the Earth corresponds to the superposition of the reflection response and its acausal counterpart. This study laid the foundation for the later ambient noise cross-correlation research. However, this study did not attract much attention in the beginning until it was found that the cross-correlation of ambient noise approximates the seismic wave in helioseismology (Rickett & Claerbout, 1999). Lobkis & Weaver (2001) extended this technique to acoustic field, and motivated a series of other studies on both the theory and applications of ambient noise (e.g., Larose *et al.* , 2004; Malcolm *et al.* , 2004; Roux *et al.* , 2004; Sabra *et al.* , 2005a,b; Weaver & Lobkis, 2001, 2003). Shapiro & Campillo (2004) first applied this technique to extract surface waves from ambient noise. Meanwhile, it was also found that EGF can also be extracted from cross-correlations of earthquake coda waves (e.g., Campillo & Paul, 2003; Snieder, 2004). Tibuleac & Seggern (2012) discovered that autocorrelation of ambient noise can reveal the crust-mantle boundaries. In addition, Yokoi & Margaryan (2008) and Tsai & Moschetti (2010) examined the relationship between the time domain cross-correlation and the SPAC method (Aki, 1957) from a theoretical point of view, and found that the cross-correlation of ambient noise is indeed equivalent to the SPAC method (Aki, 1957).

The theory behind ambient noise cross-correlation has been intensively studied. Lobkis & Weaver (2001) first described the incoherent wavefields as a sum of equipartitioned modes and demonstrated that the cross-correlation of two records of such wavefield records is able to yield the EGF. Other types of theorems emerge subsequently, such as the fluctuation-dissipation theorem (van Tiggelen, 2003); reciprocity theory (Wapenaar, 2004) and the stationary phase deviation theory (Snieder, 2004). In spite of the diversity of these theorems, almost all of them are based on the assumption that the wavefield of ambient seismic noise is diffuse, or the noise sources are uniformly distributed. In reality, such condition is rarely met.

The emergence of EGF from the NCF enabled the applications of ambient seismic noise to many fields. For example, one of the main applications is using the ambient noise for surface wave tomography, which is known as Ambient Noise tomography (ANT). Shapiro *et al.* (2005) first applied ANT to constructing the group velocity maps of southern California. Compared to the traditional earthquake-based surface wave tomography, ANT has many advantages as detailed below.

First, in traditional earthquake tomography, the earthquake sources usually contain many uncertainties, including the original time, the centroid location, the depth and source moment tensor. All of these uncertainties could propagate to the subsequent tomography results. The ANT method based on cross-correlations of ambient noise data between two stations can avoid these uncertainties of source terms because the ”sources” in ANT, which are actually seismic stations used in cross-correlation, are known, and the initial phase is also clear and constant (Lin *et al.* , 2008).

Second, the resolution of traditional earthquake-based surface wave tomography methods relies on the distribution of both earthquakes and seismic stations. It is hard to achieve high-resolution maps in aseismic regions due to the lack of regional earthquakes. Moreover, because earthquakes mainly occur at plate boundaries, tomography using earthquake data usually has very uneven path coverage. Unlike traditional tomography methods, data used in ANT are EGFs from the cross-correlations of two stations. So densely and evenly distributed path coverages can be obtained if a dense seismic array is deployed.

Third, the uncertainty of surface wave data from ambient noise can be estimated by repeating measurements from ambient noise recorded at different times; whereas there are rarely large earthquakes occurring in an exactly same location and with an exactly same focal mechanism

Fourth, it is hard to retrieve short-period (<20 s) surface waves from earthquakes because surface waves at these periods from the telesiesmic earthquakes are scattered and attenuated during the long-distance propagation. In contrast, high-quality short-period surface waves can be extracted from the cross-correlation of ambient noise.

Due to these advantages, ANT has been widely used to study the crustal and upper mantle structure. Besides, ambient noise is also used in exploration seismology (Bakulin *et al.* , 2007; Draganov *et al.* , 2007; Schuster *et al.* , 2004); monitoring of velocity changes for seismic hazards (Duputel *et al.* , 2009; Hadziioannou *et al.* , 2009; Larose *et al.* , 2004; Meier *et al.* , 2010; Sabra *et al.* , 2007); engineering geophysics (Snieder & afak, 2006); detecting the seismometer inner clock error (Stehly *et al.* , 2007; Xia *et al.* , 2015); testing Earth's model (Ma *et al.* , 2008) and calibrating earthquake centroid location (Barmin *et al.* , 2011; Xie *et al.* , 2011; Zeng *et al.* , 2014; Zhan *et al.* , 2011). Most of these applications use surface waves obtained from EGF.

1.3 Thesis objectives

Most of the applications mentioned above are based on dispersion measurements from the inter-station surface waves. However, the accuracy of dispersion measurements from ambient noise is still not clear. It is uncertain whether surface waves at periods longer than 50 s can be extracted from ambient noise recorded at portable seismic stations or whether the resulting dispersion measurements from ambient noise is accurate enough to image lithosphere and asthenosphere structures. The goal of this thesis is to address these questions, and the specific objectives include:

(1) To investigate if broadband surface waves at periods ranging from a few second to more than 100 second can be extracted from portable seismic stations, which are usually deployed for two years, such as the USArray.

(2) To evaluate the accuracy of the broadband (both short and long period) dispersion curves extracted from ambient noise and determine if these dispersion measurements are as accurate as those from earthquake data.

(3) To demonstrate how broadband surface waves extracted from ambient noise can be used to image lithosphere and asthenosphere structures from the surface down to ∼300 km using portable seismic arrays like USArray.

(4) To explore how accurate it is to use dispersion measurements from ambient noise to calibrate the earthquake location.

1.4 Structure of this thesis

This thesis is composed of seven chapters, and the content of each chapter is briefly summarised below.

In Chapter 1 (this chapter), we review the history of research on the characteristics and sources of ambient noise, the developments of ambient noise applications and the objectives of this thesis.

In Chapter 2, we firstly review the ambient noise data processing procedures and then explore the best way to extract high quality signals from ambient noise.

In Chapter 3 (published in *Bulletin of the Seismological Society of America*), we design an experiment to validate the accuracy of the short period (10-30 s) surface wave from ambient noise. The experiment is based on a ground truth event which occurred in the shallow crust.

In Chapter 4 (published in *Geophysical Journal International*), we investigate the accuracy of the long period surface wave (50-250 s) from NCF by comparing the waveforms and dispersion measurements from ambient noise with those from earthquake data.

In Chapter 5 (in preparation for *Geophysical Journal International*), after validating the accuracy of broadband surface waves from ambient noise in Chapter 3 and 4, we apply broadband (10-150 s) surface wave from ambient noise to construct a 3D isotropic shear wave velocity model of the US continent.

In Chapter 6 (in preparation for *Bulletin of the Seismological Society of America*), using a seismic array in Australia, we investigate the accuracy of earthquake location using short period surface waves from ambient noise.

Finally, in Chapter 7 we draw conclusions and also discuss possible future research.

2

Extracting EGF from ambient noise

Ambient noise tomography (ANT) is based on the fact that the Empirical Green's Function (EGF, hereafter) between two stations can be extracted from ambient Noise Cross-correlation Function (NCF). The mathematical relationship between the NCF and EGF can be expressed as follows:

$$\frac{dC_{ab}}{dt} \approx -\frac{1}{2}(G_{ab}(t) - G_{ba}(-t)), \tag{2.1}$$

where $C_{ab}(t)$ is defined as the NCF between station A and B. G_{ab} is the causal component of EGF and represents the signals travelling from station A to station B, and G_{ba} is the anti-causal component which represents signals travelling from B to A. The two sides of Equation 2.1 are not equal to each other because of the unknown amplitude factor (Weaver & Lobkis, 2001).

EGF is usually dominated by surface wave, and at most times, the amplitude of casual and anti-casual parts of the signals are different from each other, due to the uneven distribution of the ambient noise sources (Stehly *et al.* , 2006; Yang & Ritzwoller, 2008). The main component of the EGF is surface wave, however, some precursors exist in both G_{ab} and G_{ba}. These precursors come from noise sources situated in the area between seismic station A and B (Zhan *et al.* , 2010). In this chapter, the data processing of NCF calculation is reviewed and different stacking techniques are investigated.

2.1 Cross-correlation of ambient noise

The NCF, $C_{ab}(t)$ between station A and B can be expressed as

$$C_{ab}(t) = \int_0^T u_a(\tau)u_b(t+\tau)d\tau, \tag{2.2}$$

where u_a and u_b are the time series of ambient noise recorded at station A and B respectively and T is the length of time series. To compute the Cross-Correlation (CC) more effectively, we can use Fast Fourier Transform (FFT) method, in this case Equation 2.2 can be transformed into:

$$C_{ab}(t) = F^{-1}(F(u_a(t))F^*(u_b(t))), \tag{2.3}$$

where F is the forward FFT transformation, F^{-1} is the backward FFT transformation and $*$ is complex conjugate transformation.

Schimmel (1999) presented a procedure to compute the coherence function, called Phase Cross-Correlation (PCC) before getting the NCF. The formula of the PCC is expressed as:

$$pcc(t) = \frac{1}{2N}\sum_{\tau=\tau_0}^{\tau_0+T} |e^{i\phi(t+\tau)} + e^{\psi(\tau)}|^{\nu}, \tag{2.4}$$

where $e^{\phi(\tau)}$ and $e^{\psi(\tau)}$ are the amplitude-normalized analytical signal of the ambient noise $u_a(t)$ and $u_b(t)$, respectively. $2N$ is the number of samples at the length of the time series and the ν controls the sharpness of the waveform. The analytical signal $S(t)$ is defined as:

$$S(t) = u(t) + iH[u(t)] = A(t)e^{i\phi(t)}, \tag{2.5}$$

where H stands for Hilbert transform; $A(t)$ is the amplitude and $\phi(t)$ is instantaneous phase. Since PCC does not require the amplitude information, the single station preparation can be simplified by removing both time domain normalization and spectral whitening. Schimmel *et al.* (2011) showed that the waveforms after applying PCC and normal CC are similar to each other; however PCC is more time consuming than normal CC. For example, normal CC needs the operation of $O(3NlogN)$ (where $NlogN$ is the number of operation for a FFT both backward and forward, and N for multiply in frequency domain), while the PCC needs the operation of about $O(4NlogN + N^2)$.

Bensen *et al.* (2007) provided a detailed description of data processing procedures for extracting NCF from ambient noise. Here we just give a brief review of these procedures, which mainly consist of three parts, including single station preparation, cross-correlation and stacking. The procedure proposed by Bensen *et al.* (2007) was developed to minimize the effect of earthquake, irregularity interferences and expand the period of extractions.

2.2 Single station preparation

Continuous seismic records of ambient noise are first cut into a series of daily segments (or several hours' segments). The daily records are decimated to one sample per second, and then the linear trend, mean and instrument responses are all removed from the seismograms. Subsequently, the daily seismograms are band-pass filtered. The period band used to filter the ambient noise and the sampling rate depends on the period band of interest.

The next step, which is the most important step in single station preparation, is time domain normalization. As it is well known, for calculating NCF, some unwanted signals, such as earthquake events and instrumental irregularities, could severely contaminate the result. There are various ways to suppress these unwanted signals through time domain normalization. For this study, the running-absolute-mean normalization method is adopted (Bensen *et al.* , 2007). The running-absolute-mean normalization is mathematically expressed as:

$$u_n(i) = u_0(i) / \sum_{j=i-N}^{i+N} |u_0(j)| / (2N+1), \tag{2.6}$$

where $u_o(i)$ is the original waveform, and $u_n(i)$ is the time domain normalized waveform. The width of the normalization window is $2N + 1$, and N is chosen to be approximately half of the maximum period of the bandpass filter. However, varying this value gives a similar result (Bensen *et al.* , 2007). By trying a variety of time domain normalization methods, Bensen *et al.* (2007) demonstrated that running-absolute-mean normalization method is a robust and efficient method to suppress unwanted signals.

Shen *et al.* (2012b) proposed an improved technique to do time domain normalization, which can be expressed as:

$$FTN(t) = \sum_{k=1}^{nf} s[t|(f_k, f_{k+1})|]/|H\{s[t|(f_k, f_{k+1})|]\}|, \tag{2.7}$$

where the $FTN(t)$ is normalized waveform, $s[t|(f_k, f_{k+1})|]$ is a narrow frequency band filtered time series and H is for Hilbert transform. They demonstrated that by applying this new technique, the Signal-to-Noise Ratio (SNR) of resulting EGF can be significantly improved and the period range of the resulting signal can also be extended. Here SNR is defined as the ratio between the peak amplitude and the root-mean-square of the tailing series of the narrow bandpass filtered waveform. However, their conclusion is made based on the comparison of their results with that from one-bit normalisation. Comparing their method with the running-absolute-mean normalization, we find that the results from both methods are comparable. Therefore, we prefer the running-absolute-mean method in performing our time domain normalization.

After the time domain normalization, the temporally normalized signals are then whitened in frequency domain to balance the frequency energy, which can expand the period range when the dispersion curves are automatically extracted. This procedure concludes the single station preparation. The second stage involves the cross-correlation of each one-day-long (or several hours) time series between each station pair.

2.3 Temporal stacking

The second step of extracting EGF from ambient noise is temporal stacking. This step is important, because the SNR for short-time (e.g., one-day) cross-correlation is usually not good enough to obtain high SNR surface wave signals. In addition, ambient noise source is not diffuse enough, which usually results in contaminations and uncorrelated noise in

NCF. Fortunately, the incoherent signals can be minimized by stacking lots of daily NCF together, thereby enhancing the coherent signals. Yang & Ritzwoller (2008) demonstrated that one-year stacking is good enough to obtain stable and reliable EGFs. Most studies routinely apply the linear stacking technique to stack the short time NCFs. In order to get higher SNR signal, Schimmel & Paulssen (1997) proposed a Phase Weighted Stacking (PWS) method to suppress the noise, and later Schimmel & Gallart (2007) improved the PWS stacking method by introducing the S-transformation. This new and improved stacking method is called time and frequency Phase Weighted Stacking (tf_PWS). The PWS can be mathematically expressed as:

$$s_{pws}(t) = \frac{1}{N}\sum_{j=1}^{N} c_j(t)\Big|\frac{1}{N}\sum_{k=1}^{N} exp[i\Phi_k(t)]\Big|^{\nu}, \tag{2.8}$$

where $s_{pws}(t)$ is the final stacked waveform, $c_j(t)$ is the daily NCF, $\Phi_k(t)$ is the instantaneous phase mentioned before. Power ν controls the sharpness of the final coherent signal. The tf_PWS is expressed as:

$$S_{tf\_pws}(t) = S^{-1}(c_{ps}(\tau, f)S_l(\tau, f)), \tag{2.9}$$

where $S_{tf\_pws}(t)$ is the final stacked waveform, S^{-1} is the backward S transform. $S_l(\tau, f)$ is S transform of linear stacking waveform and c_{ps} is time frequency phase stack as expressed below,

$$c_{ps}(\tau, f) = \Big|\frac{1}{N}\sum_{j=1}^{N}\frac{S_j(\tau, f)e^{i2\pi f\tau}}{|S_j(\tau, f)|}\Big|^{\nu}. \tag{2.10}$$

S-transform is defined as:

$$S(\tau, f) = \int_{-\infty}^{\infty} u(t)\omega(\tau - t, f)e^{-i2\pi ft}dt, \tag{2.11}$$

where $\omega(\tau - t, f)$ is a Gaussian window function centered at time τ, with the window width proportional to $|1/f|$.

$$\omega(\tau - t, f) = \frac{|f|}{k\sqrt{2\pi}}e^{\frac{-f^2(\tau-t)^2}{2k^2}} \tag{2.12}$$

Both of these two methods are based on phase weighted stacking, which can avoid the amplitude interference. For example, when a daily NCF is dominated by some local source signals, which are strongly coherent, the final stacked trace will be contaminated if they are stacked linearly. These two phase weighted stacking methods have been used to process seismic data for tomographic study (e.g., Dias *et al.* , 2014; Yang, 2014) or receiver function study (e.g., Crotwell & Owens, 2005). However, these two methods are non-linear stacking techniques and the resulting NCF waveforms could be distorted. Even though these stacking techniques denoise the traces and help to enhance the useful signal significantly, especially the tf_PWS (e.g., Baig *et al.* , 2009), we need to investigate whether the NCF from these stacking technique is accurate enough for the subsequent analysis.

2.4 Waveform distortion caused by nonlinear stacking

In order to investigate the extent to which the waveforms are distorted by nonlinear stacking techniques, we designed a synthetic test. First, we compute a synthetic seismic waveform, then different types of noise are added to generate a series of contaminated waveforms. After that, different stacking methods including the time domain linear stacking (TL), PWS and tf_PWS, are employed to stack the waveforms, respectively. Subsequently, the waveform and dispersion information from each stacking method are compared with that from the original synthetic waveform.

The CPS program (Herrmann & Ammon, 2002) is used to calculate the fundamental mode Rayleigh wave response (Green's Function (GF)). To meet the far field approximation, the receiver is placed at an epicentral distance of 1000 km. The 1D PREM velocity model (Dziewonski & Anderson, 1981) is used for the computation (Figure 2.1).

To make the waveform similar to a real NCF, the original GF is bandpass filtered in the period range of 10-20 s and 5-10 s, respectively before they are added together (Figure 2.2). Three different types of noise namely: normal noise (NN) with random amplitude at every time point (which is also known as white noise), real ambient noise record (AM) with a random time series and coda waves (CO) of random NCFs are tested (Figure 2.1).

The maximum amplitude of ambient noise varies as 10%, 20%, 50% and 100% of the maximum amplitude of the GF. TL, PWS and tf_PWS are applied to 100, 200, 300, 400, 500 and 600 traces respectively (Figure 2.3-Figure 2.5).

The PWS obviously has changed the waveform with NN noise added (left column in

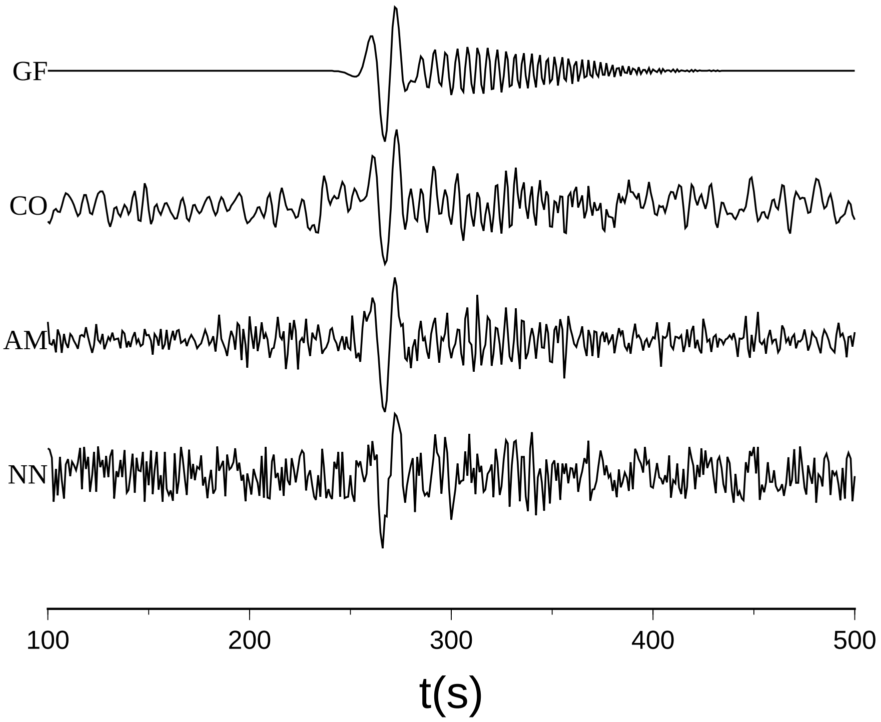

Figure 2.1: Synthetic vertical Green's Functions (GFs). GF is calculated using CPS (Herrmann & Ammon, 2002) based on 1D PREM model (Dziewonski & Anderson, 1981). Waveforms 2-4 are the Green's functions contaminated by different types of noise, and the amplitude of the noise is 50% of the GF. NN is the normal noise; AM is the noise recorded by stations of the networks of TA, II, IU, CI and US in Jan 1th, 2012 and CO is the corresponding random coda of all NCFs on that day.

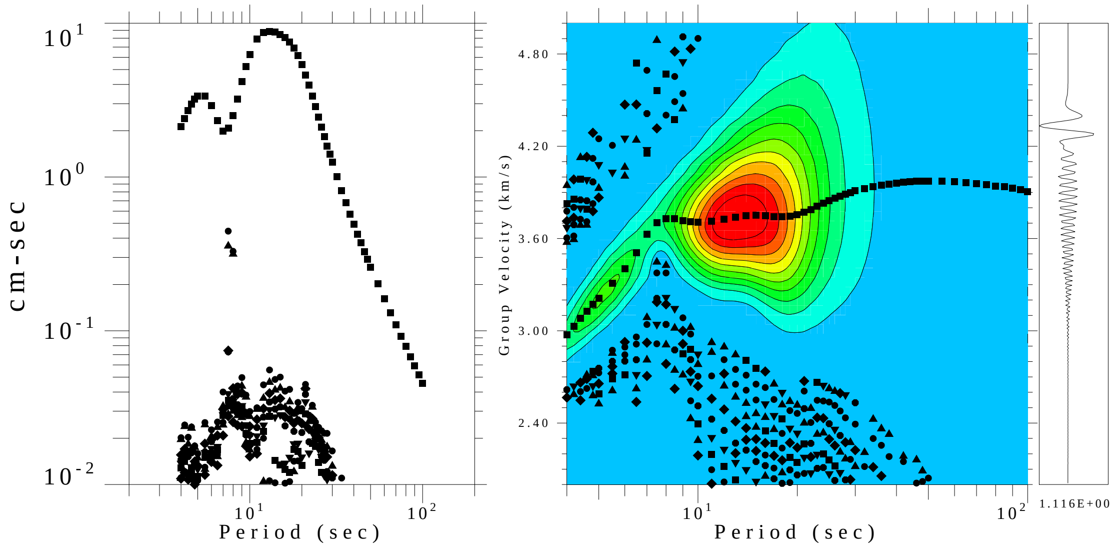

Figure 2.2: The diagram of multiple filter technique analysis for the synthetic GF. The original GF was bandpass filtered in period bands of 5-10 s and 10-20 s, before they are added.

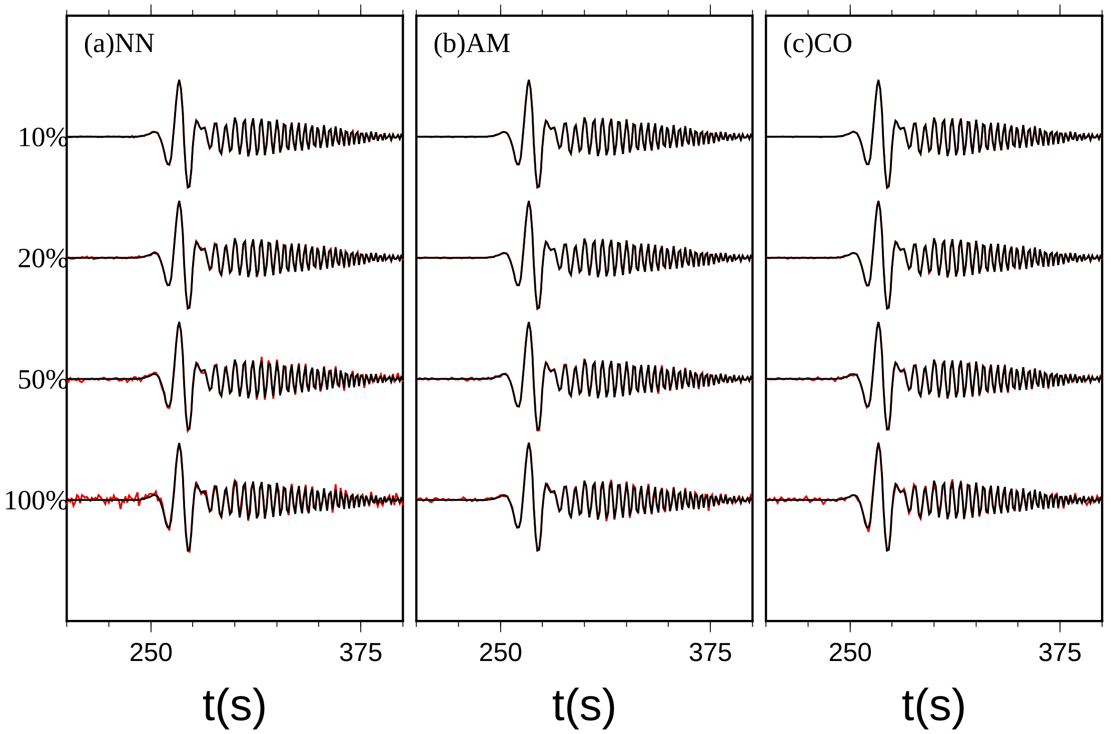

FIGURE 2.3: The recovered waveforms based on Time domain Linear stacking method (TL). The noise type of (a), (b) and (c) are NN, AM and CO, respectively. The black curve is the target waveform (GF), and the red curves are the recovered waveforms using 100 contaminated waveforms. The percentages shown in the figure represent the ratio between the maximum amplitude of the noise and the maximum amplitude of the GF.

Figure 2.4). And small wiggles can be found in the recovered waveform using TL. It seems that tf_PWS recovered waveforms are the best with almost no uncorrelated signals. The group velocity and phase velocity at the period band of 5-50 s are extracted using the Frequency and Time Analysis Technique (FTAN) as used in Bensen *et al.* (2007) (see a more detailed description in Chapter 5). The resulting dispersion curves are shown in Figure 2.6-Figure 2.8.

The tf_PWS stacking results in very stable SNR values at each period (Figure 2.8), which is probably due to a large number of traces in stacking. The dispersion curves extracted from the waveforms using tf_PWS are the closest to the measurements from original GF when compared to the other two stacking methods. Though the TL and PWS method recover the waveforms equally well, the group velocity measurements from these two methods are different. Also the group velocity measurements are not well recovered compared to the

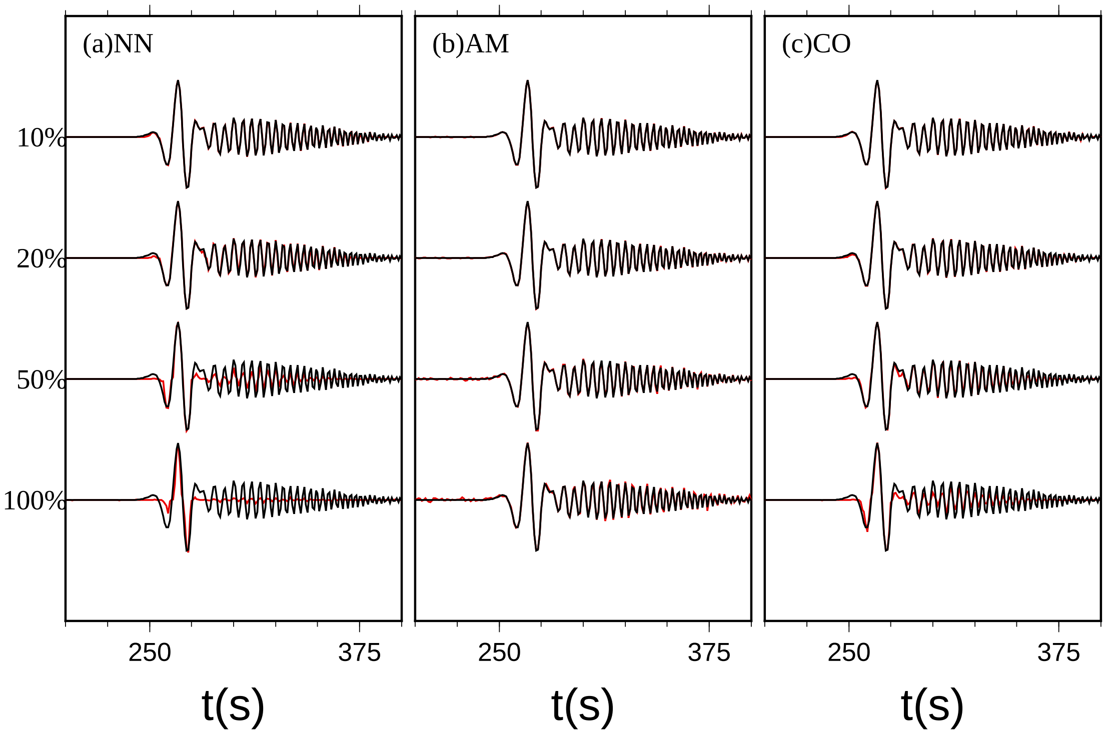

Figure 2.4: Similar to Figure 2.3, but based on PWS stacking method.

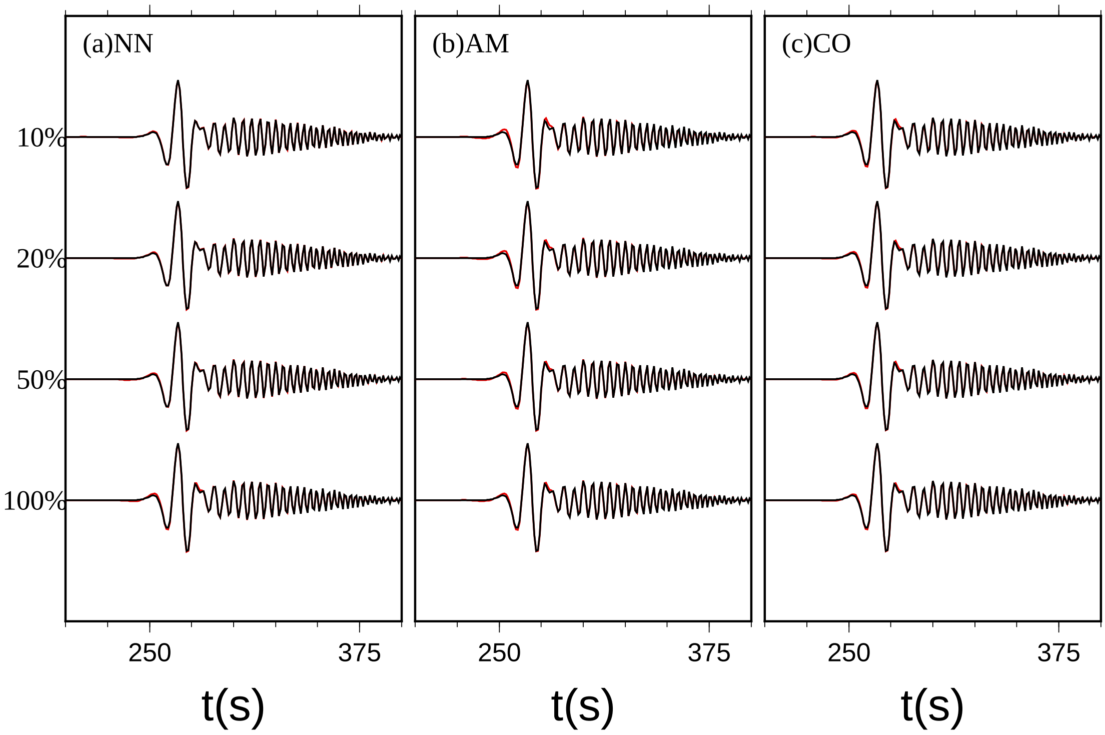

Figure 2.5: Similar to Figure 2.3, but based on tf_PWS stacking method.

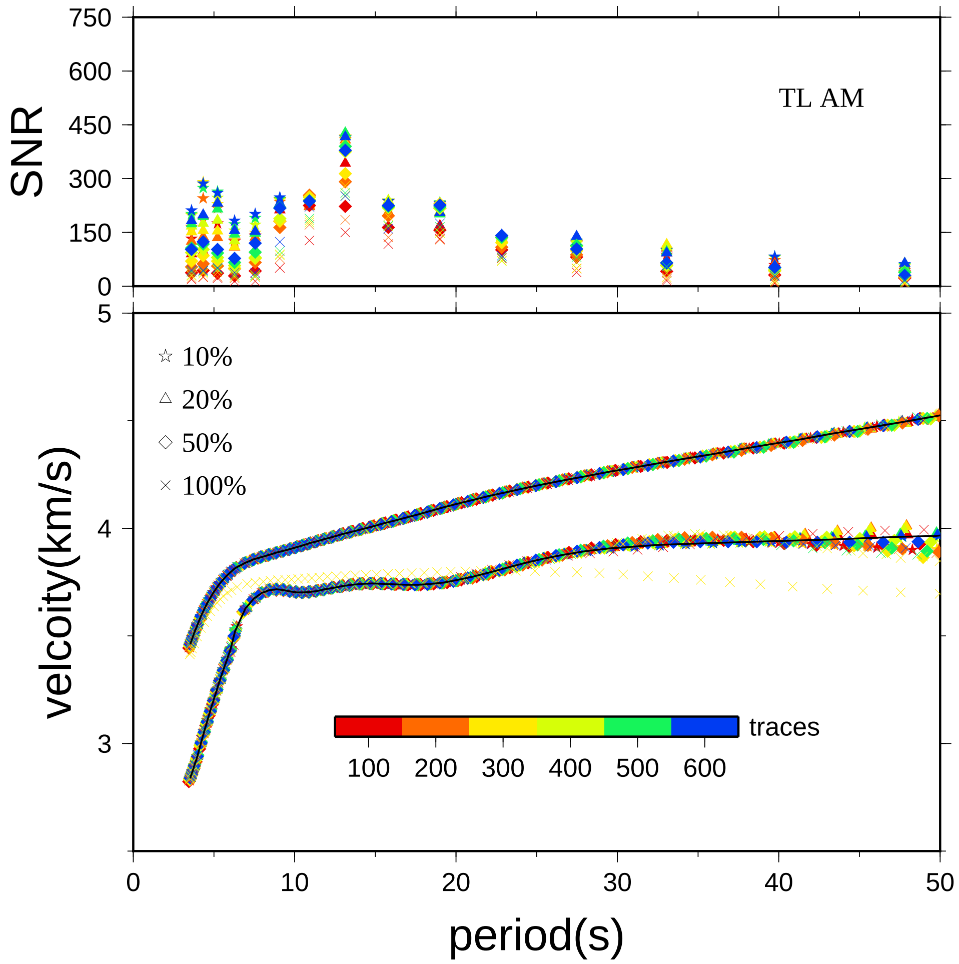

FIGURE 2.6: Dispersion curves extracted from the waveforms from Figure 2.3. The fast and slow velocities represent the phase velocity and group velocities, respectively. The black curve is the dispersion curve extracted from GF. It is clear the phase velocity extracted from the recovered waveform is more accurate than the group velocity.

phase velocities (Figure 2.6 and Figure 2.7). Compared with TL, the phase involving stacking method is more efficient in recovering the coherent phase signal, however TL recovers signals better with high energy.

The comparison of these three stacking methods (Figure 2.9) shows that tf_PWS works much better in recovering the waveform than TL and PWS. However, in the long period band around 50 s, the phase velocity measurement extracted from the waveforms using tf_PWS stacking method is slightly faster than that of the real waveform. Meanwhile, the phase velocity at long periods measured from waveforms stacked using tf_PWS is sometimes lower than that from the other two methods, which indicates that the waveform is distorted.

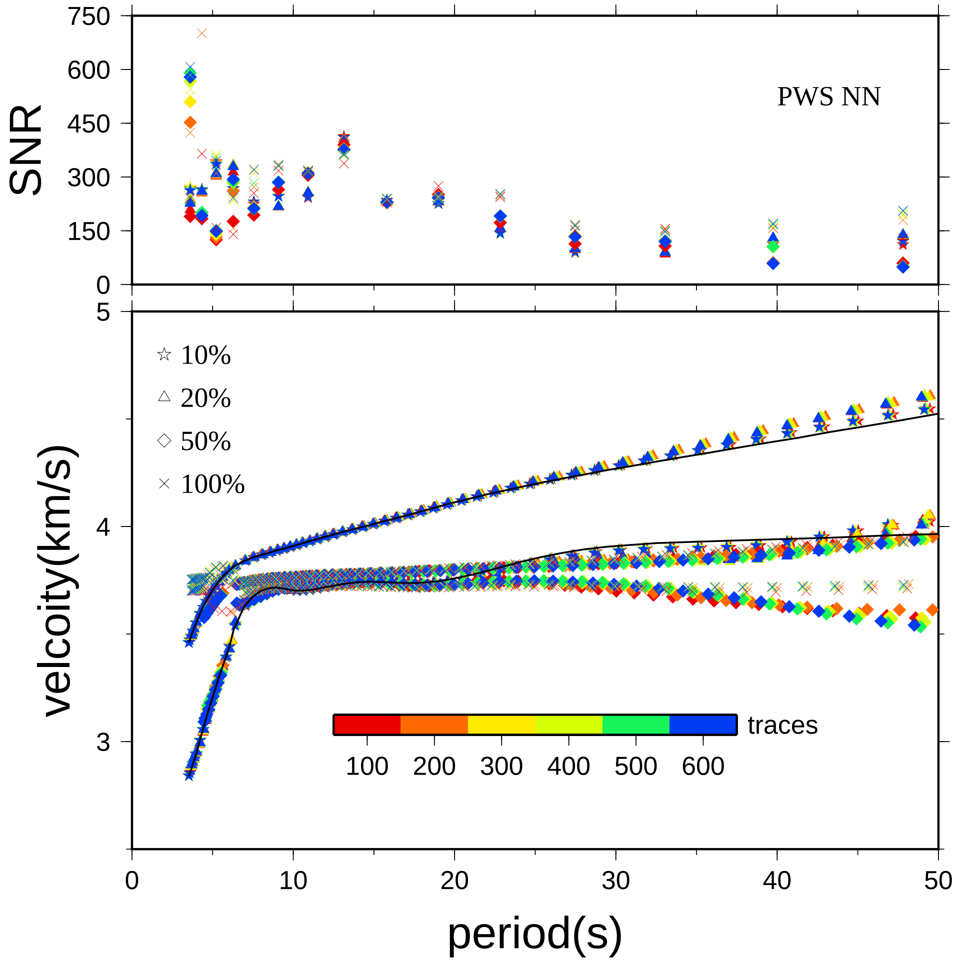

Figure 2.7: Dispersion curves extracted from the waveforms from Figure 2.4. Phase velocity slower than the group velocity is due to the cycle skipping. It indicates that when the amplitude of the noise is large (50% and 100%), the waveform can not be well recovered.

However, we are not sure how tf_PWS modifies the real data.

To understand how tf_PWS modifies the real data, we apply the TL and tf_PWS stacking technique to ambient noise data from USArray seismic stations. We calculated NCFs among all the USArray seismic stations (the detailed descriptions of data processing can be found in Chapter 5). We used TL and tf_PWS to compute the final NCFs, respectively. We compared both the waveforms and phase velocities of these two stacking methods. Figure 2.10 is an example of the waveform and phase velocity comparison for station pairs 221A/TA and SCIA/US.

The left column in Figure 2.10 shows the waveform comparison at different period bands, where the red waveform is from TL, and the black is from tf_PWS. We calculated the time

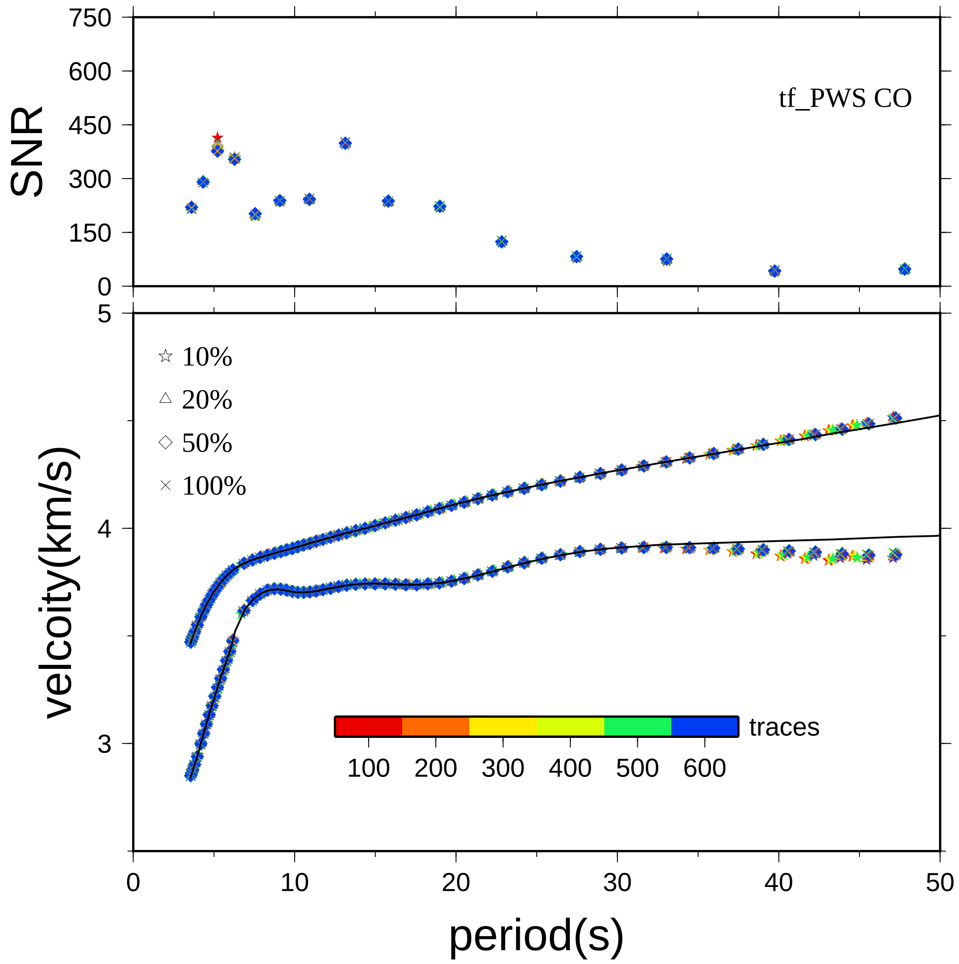

FIGURE 2.8: Dispersion curves extracted from the waveforms from Figure 2.5. The dispersion curves are stable and close to the synthetics. However at the long period (>35 s), the dispersion curves show systematic discrepancies with the synthetics.

shifts of these two waveforms using cross-correlation method, and results are shown in the middle. The surface waves at different period bands arrive at different times, indicating that the surface waves are dispersive, with longer period surface waves travelling faster. It is clear that time shifts exist at the period bands of 30-50 s, 50-100 s and 200-300 s. Phase difference can be observed from the recovered waveforms from tf_PWS and TL (The top right of Figure 2.10). The second figure in the right column of Figure 2.10 shows the SNR as a function of period, and obviously tf_PWS shows higher SNR than TL. The phase velocity dispersion curves plotted in the third row in the right column (Figure 2.10) are extracted using FTAN (see Chapter 5). The mismatches are mostly observed at the periods of 50,100 and 200 s, which is consistent with the waveform comparison.

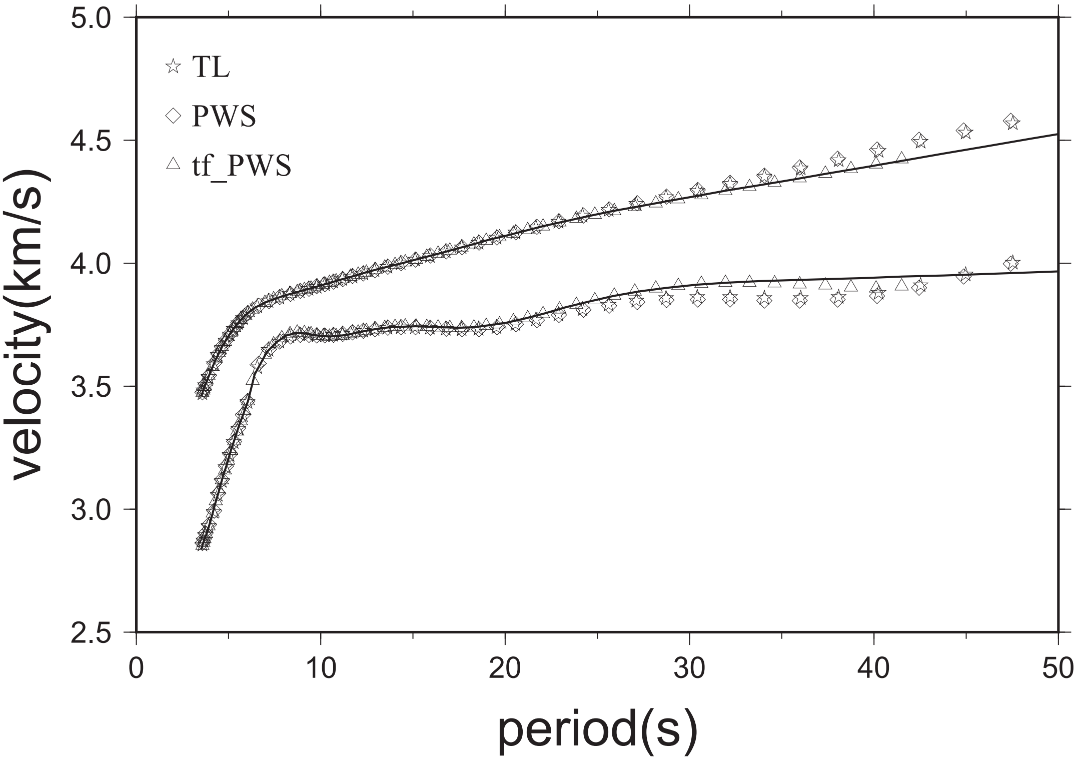

FIGURE 2.9: Comparisons of the dispersion curves resulted from the three stacking methods (TL, PWS and tf_PWS). The contaminated noise is CO, and the amplitude is 100% with respect to the GF. 600 traces are used during the stacking. See the text for detailed information.

A surprising observation is that although the tf_PWS enhances the signal significantly, the longest period of the phase velocity that can be extracted is shorter than that from the TL. The bottom figure in the right column (Figure 2.10) shows the phase velocity difference (red curves, positive value represents the surface wave from tf_PWS travelling faster than that of TL) and travel time difference converted from the phase velocity (black curves, the positive value means that the surface wave from tf_PWS travels slower than that of TL). There are constant differences in the waveforms, phases, phase velocities and travel times between tf_PWS and TL, indicating the tf_PWS distorts the waveforms.

Figure 2.11 shows the distributions of two phase velocity differences between velocities from tf_PWS and those from TL at four different periods, where a, b, c and d represents 20, 30, 50 and 100 s respectively. The mean and the standard error are shown on the left corner, with the positive value implying that the phase velocity from tf_PWS is faster than that from TL.

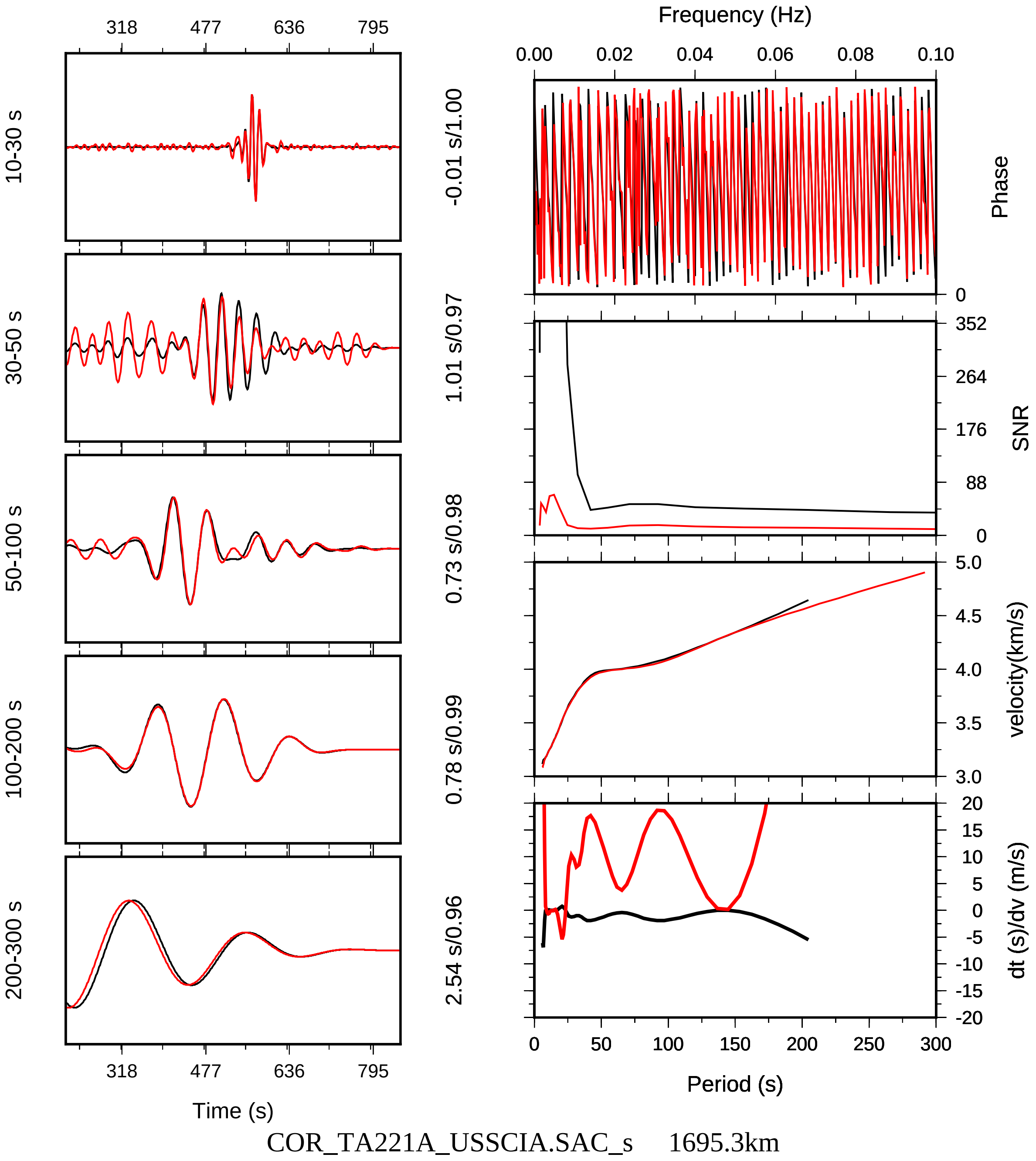

FIGURE 2.10: An example of the NCF (between 221A/TA and SCIA/US) comparison between that from tf_PWS and TL. The interstation distance is 1695.3 km. The red curves are the results of TL and the black curves are from tf_PWS. Comparisons here include waveforms at different periods (left diagram), phases, SNR, phase velocity and traveltimes, respectively. See the text for detailed information.

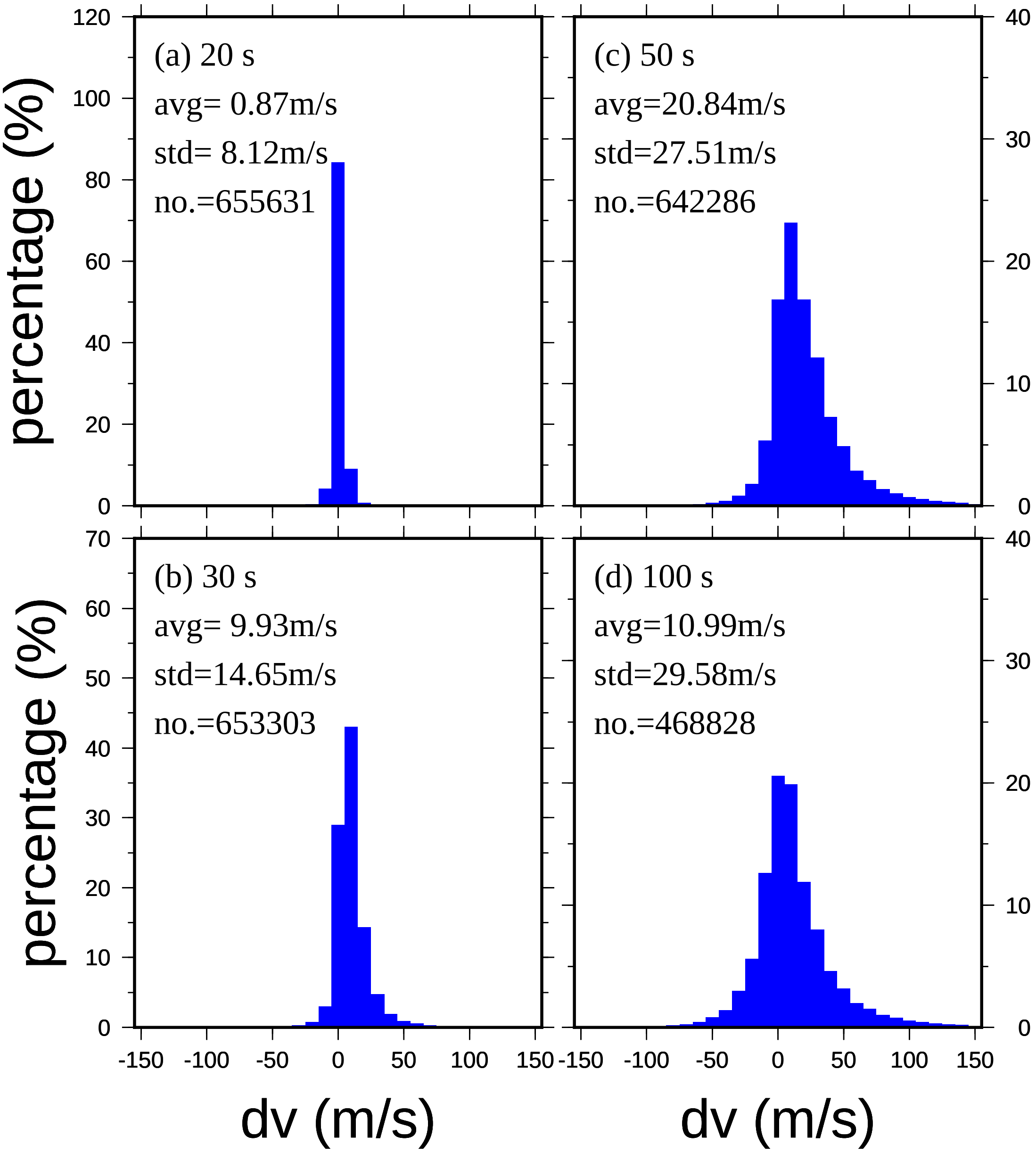

Figure 2.11: The surface wave phase velocity difference of the NCFs between that from tf_PWS and TL. The NCFs used here are from the USArray (See Chapter 5). Positive value here means the phase velocity of NCF based on tf_PWS is larger than that from TL. a, b, c and d are the phase velocity difference for periods of 20, 30, 50 and 100 s, respectively.

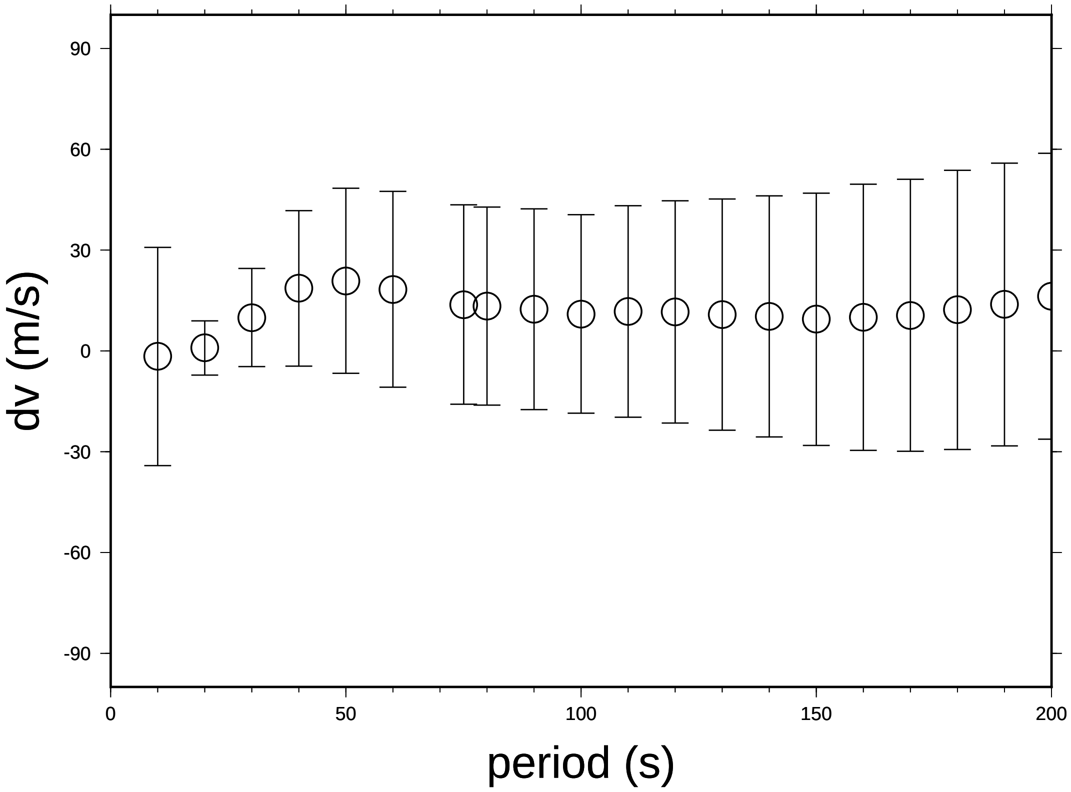

Figure 2.12: Phase velocity difference (Figure 2.11) versus the period. The error bar is the standard error of the phase velocity difference at each period.

The phase velocity values from tf_PWS are always higher than those of TL at all periods (Figure 2.12). The maximum difference is observed at the period of 50 s (~20 m/s) and the minimum is around 10 and 20 s (close to 0.) The phase velocity difference shows contrary features with the New Noise Model (NNM) (Peterson, 1993), where NNM shows high energy at about 10 and 20 s, and reaches the minimum at about 50 s. It is consistent with the SNR curves, which shows the largest value around 20 s and decrease on both sides of period. However, the standard error of the phase velocity differences shows an opposite trend. This indicates that the phase velocity measurements are correlated with the SNR.

The phase velocity difference may also be caused by the measurement method. In order to investigate this, Moving-Window Cross-Spectral Analysis (MWCS) is used to measure the waveform time shift between that of the tf_PWS and TL. MWCS is usually used to measure the velocity change of the medium with high accuracy (Brenguier *et al.* , 2008). In the time shift measurement we first apply a narrow bandpass filter centred at each period to the waveforms. The surface wave window is determined as a two period long time sequence centered at the maximum amplitude of the bandpass filtered waveform. We keep the waveform pairs with cross-correlation coefficient larger than 0.98.

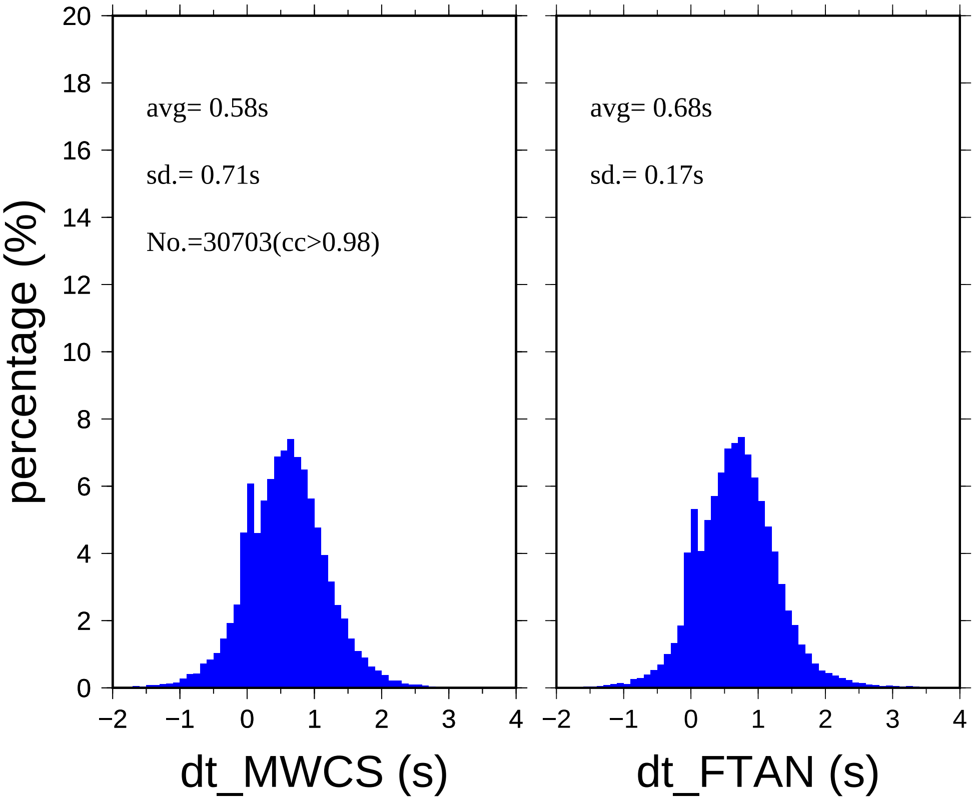

Figure 2.13: The NCF waveforms time shift between that from tf_PWS and TL, and the time shifts are measured by MWCS (left) and FTAN (right), respectively. During the time shift measurement, NCF waveforms are bandpass filtered with a narrow filter window centred in 40 s. The mean and standard error are calculated and shown in the upper left corner. Number of the measurements is 30703, with cross-correlation coefficient bigger than 0.98. Positive value here means the surface wave of NCF from tf_PWS travels faster than that from TL.

Figure 2.13 shows the time shifts at the period of 40 s, where the positive value implies that the surface waves from tf_PWS arrive earlier than that from TL. The left figure shows the time shifts measured using MWCS, and the right figure is the travel time difference converted based on the phase velocity. Both of them show a systematic bias, which implies that the difference between the two stacking techniques does not arise from the measurement method.

Since each NCF pair has two measurements (Figure 2.13), a comparison is made by using the time shifts of each NCF pair measured from MWCS and FTAN, and plotted in

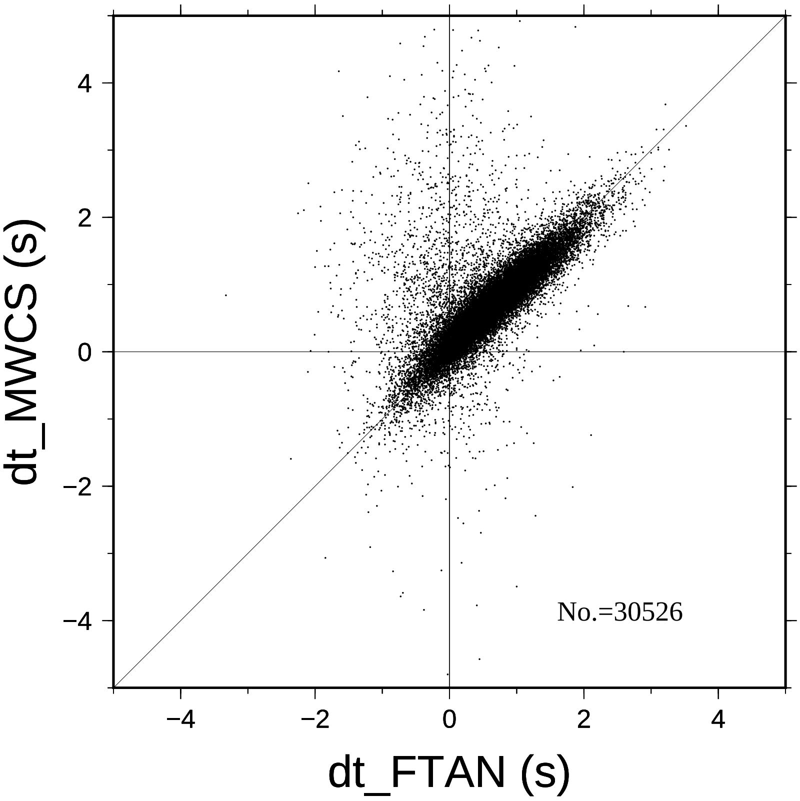

FIGURE 2.14: Surface waveform time shifts at 40 s for NCF pairs (calculated from tf_PWS and TL), which are measured by FTAN (X-axis) and MWCS (Y-axis), respectively. The points taken those two measurements as coordinates lie around the diagonal line, indicating that those two measurement is consistent with each other.

Figure 2.14. The two measurements are consistent with each other, which indicates that the discrepancies are constant and reliable.

2.5 Conclusion

In this chapter, we review the data processing procedures for extracting EGF from ambient noise. Through the synthetic test, we find that the stacking methods (tf_PWS and PWS), which are based on phase coherence, slightly distort the waveforms, especially at periods longer than 50 s. We also use real ambient noise data to investigate the waveforms stacked by tf_PWS and TL. The phase velocity shows a systematic bias between tf_PWS and TL. Thus, in this thesis, we use the linear stacking method to stack the daily NCFs rather than using the tf_PWS method even though tf_PWS can significantly enhance the SNR of the resulting surface waves.

3

Validating accuracy of Rayleigh wave dispersion extracted from ambient seismic noise via comparison with data from a Ground-Truth earthquake

3.1 Abstract

In order to validate the accuracy of estimated Green's functions (EGFs), which are widely used in ambient seismic noise tomography, a broadband seismograph was installed in the epicentral area of an M 5 earthquake, with ground-truth location from Interferometric Synthetic Aperture Radar observations. EGFs between this station and permanent stations are

compared with surface waves excited by the earthquake. The group velocity dispersion measured from EGFs at large interstation distances (∼1000 km or longer) are consistent with measurements from the earthquake, and the EGFs from symmetric noise correlation functions (NCFs) are usually more accurate. At shorter interstation distances (300-1000 km), the match between noise and earthquake dispersion is good for most stations, although we observed mismatch for a few stations. The mismatch is probably caused by low signal-to-noise ratio of NCFs or nondiffusive noise wavefield at short distances.

3.2 Introduction

Ambient noise tomography (ANT) is a recent breakthrough in seismic imaging technologies. Based on theoretical derivations and acoustic experiments, the full Green's function is demonstrated to be retrievable from cross correlation of ambient noise recorded on a pair of receivers (stations) (Shapiro & Campillo, 2004; Snieder, 2004; Weaver & Lobkis, 2001). Based on group or phase velocity dispersion measured in noise correlation functions (NCFs), ANT studies have been conducted to image crustal and upper-mantle velocity structure on both regional and continental scales (Ritzwoller *et al.* , 2011). Compared to earthquake surface-wave tomography, which features longer period and suffers from inaccurate source parameters (location, depth, origin time, etc.), the resolution of ANT is substantially improved and tectonic features are revealed in unprecedented detail.

The validity of ANT requires evenly distributed noise source, diffusiveness, or equipartition of energy in the noise wavefield (Snieder, 2004; Zhan *et al.* , 2010). Ambient noise in the 2-30 s frequency band, also called microseism, is mostly generated by ocean waves (Bromirski, 2009). However, microseismic source distribution is inhomogeneous, as manifested by spatially varying ocean wave height (Kedar *et al.* , 2008; Young, 1999), and the inhomogeneity of noise sources is usually used to explain the asymmetry of NCF and the precursors to interstation surface waves (Stehly *et al.* , 2006; Zhan *et al.* , 2010). Furthermore, recent studies about the 26 s microseism and the Kyushu Island signal demonstrate another case of extremely spatially inhomogeneous microseismic source, the persistent and localized noise sources (Shapiro *et al.* , 2006; Xia *et al.* , 2013; Zeng & Ni, 2010). Numerical simulation with smooth distribution of noise sources suggests that noise source inhomogeneity does not substantially affect the accuracy of the estimated Green's function (EGF) when signal-to-noise ratio (SNR) of the interstation surface wave is high (Yang & Ritzwoller, 2008). However, the real distribution of noise sources on the Earth is not well resolved, and independent validation of EGF is needed.

Shapiro & Campillo (2004) demonstrated that EGFs from NCFs provide similar Rayleigh-wave group dispersion to that predicted by 3D earthquake surface tomography between 0.008 and 0.07 Hz. EGFs are also very close to surface waves in the 0.05-0.1 Hz band from earthquakes in California(Shapiro & Campillo, 2004). However, directly comparing EGFs and earthquake records requires accurate source parameters, such as origin time, locations, focal depth, and focal mechanisms (Barmin *et al.* , 2011; Xie *et al.* , 2011; Zhan *et al.* , 2011). The horizontal location error of moderate earthquakes may be up to a dozen kilometers, which may introduce significant arrival shift (∼5 s for 15 km mislocation for shortperiod surface wave) in surface-wave dispersion measurement, especially for short epicentral distances (∼5% for 300 km). To minimize the effect due to mislocation in comparing noise and earthquake data, it is necessary to use seismic records from shallow ground-truth events. We therefore designed a field experiment by installing a broadband seismic instrument in the epicentral area of a shallow earthquake (∼M5) to compare the dispersion between noise derived EGFs and earthquake surface wave and then assess the accuracy of EGFs.

3.3 Data

On 30 January 2010, an Ms 4.8 earthquake occurred near Suining, a city in the center of Sichuan basin of China (Fig. 1a), and the strong short-period Rg wave and short interval between teleseismic pP and P waves argue for a very shallow depth of 2 km or less (Luo *et al.* , 2011). One coseismic interferogram was formed from a pair of Advanced Land Observation Satellite (ALOS)/PALSAR images (20100119-20100306) using the Jet Propulsion Laboratory/Caltech ROI_PAC software (version 3.1 beta; Rosen *et al.* (2004)). The topographic phase contribution was removed using a version of the Shuttle Radar Topography Mission 3 arcsec (∼90 m) spacing digital elevation model that has the voids filled with other data sources (Jarvis *et al.* , 2008), and the interferograms were unwrapped using the SNAPHU algorithm (Chen & Zebker, 2000) to obtain line-of-sight displacements of ∼10 cm (Fig. 1b). Modeling the event as an elastic dislocation (e.g., Li *et al.* , 2011) suggests that this moderate event had a very shallow centroid depth of 0.44 km with a centroid location of 30.284° N, 105.696° E. From the coseismic deformation observed with Interferometric Synthetic Aperture Radar (InSAR), the rupture length is shorter than 2 km (Fig. 1b), which is consistent with an earthquake weaker than M5. Such a very shallow moderate event is very valuable for validating noise EGFs due to their compact source dimension.

Table 3.1: Source Parameters of the Suining Earthquake.

Origin Time (yyyy/mm/dd hh:mm:ss.s)	Latitude 1(°E)	Longitude 1(◦N)	Focal Depth 1(km)	Magnitude 1(Ms)	Latitude 2(°N)	Longitude 2(°E)	Focal Depth 2(km)	Magnitude 2(Mw)
2010/01/30 21:36:57.4	30.28	105.71	5	4.8	30.28398	105.6956	0.6	4.68

Because the location of Suining earthquake is accurately determined, a broadband temporary seismograph (SNI station, short for SuiNIng) consisting of a Güralp CMG-3ESPCD with flat response in the 0.02-60 s band, was installed in its epicentral area in March 2011. Because the centroid location is near a river and roads that cause substantial noises, the station was installed about 1.5 km from the centroid location to alleviate contamination from cultural noises. Fifteen months of continuous high-quality data were acquired. Continuous vertical-component seismic data for the same time span were requested from Incorporated Research Institutions for Seismology Data Management Center (IRIS-DMC), including seismic stations from the Global Seismic Network (GSN) (IC/II/IU network; Fig. 1a). We also collected continuous waveform data from the China Earthquake Network Center (CENC) to complement the sparse GSN stations.

---

[a] Latitude 1, longitude 1, and depth 1 are from the earthquake catalog (see the text). Latitude 2, longitude 2, and depth 2 are inverted from Interferometric Synthetic Aperture Radar (InSAR) ground deformation data.

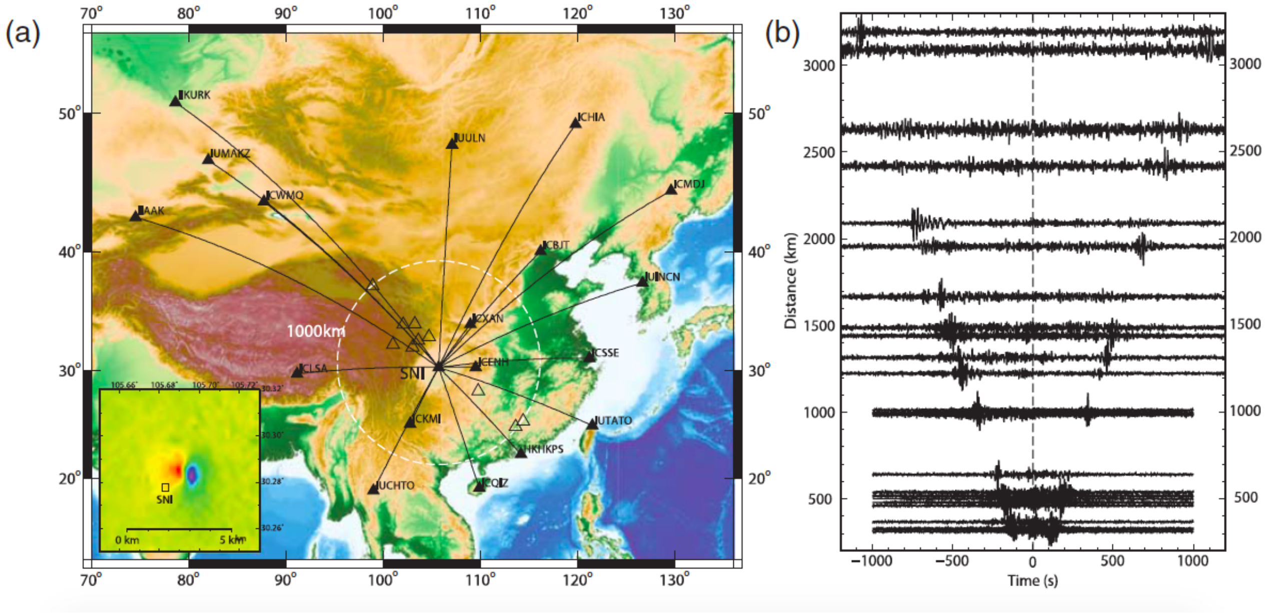
(a)
70°
80°
90°
100°
110°
120°
130°
50°
40°
30°
20°
IIKURK
IUMAKZ
ICWMQ
IIAAK
IUULN
ICHIA
ICMDJ
ICBJT
IUINCN
ICXAN
1000km
ICENH
ICSSE
ICLSA
SNI
ICKMI
IUTATO
HKHKPS
ICQIZ
IUCHTO
105.66°
105.68°
105.70°
105.72°
30.32°
30.30°
30.28°
30.26°
SNI
0 km
5 km
(b)
3000
2500
2000
1500
1000
500
Distance (km)
−1000
−500
0
500
1000
Time (s)

Figure 3.1: The location of earthquake (black triangle in the center of the circle) occurred in Suining, Sichuan province (M4.8, Jan. 30 th, 2010) and the distribution of the stations used in our research. The blank circle denotes the distance of 1000 km away from the earthquake. Right column shows the NCFs between ZHB with other stations in the period band 10-30 s.

Similar to the standard noise cross-correlation processing methods (Bensen *et al.* , 2007), linear trend and instrument responses were removed as the first step of data preprocessing. In order to investigate whether time-domain normalization influences surface-wave dispersion, the noise data was processed in two ways. That is, we generated two sets of NCFs, one with the time domain running-average method as proposed by Bensen *et al.* (2007) and the other without the time-domain normalization. Because recent research demonstrates that convergence toward a stable NCF is faster for waveform segments shorter than one day (Seats *et al.* , 2012), the 15-month continuous waveform data are partitioned into two-hour segments. After the preprocessing, the two-hourlong segments of the 15 permanent stations were cross correlated with those of the SNI temporary station to obtain NCFs, which are then stacked to get final NCFs for the entire 15 months. Some authors proposed that symmetric NCFs (summation of the positive time-lag section and the negative time-lag section of NCFs) may suppress directivity of noise fields (Yang & Ritzwoller, 2008). In order to investigate whether symmetric NCFs outperform one-sided NCFs, we get final NCFs by stacking the one-sided NCFs and symmetric NCFs.

The group velocity dispersion measurement is based on the multiple-filter technique, and the CPS software package is used (Herrmann & Ammon, 2002). Usually the interstation distance has to be three time longer than the surface wavelength (Bensen *et al.* , 2007), and all the station pairs used in this study meet the requirement for surface-wave periods up to 30 s. Group velocity dispersion for the earthquake is measured on the vertical ground velocity seismograms with instrument response removed. The location of the earthquake is taken from the estimated centroid location from InSAR observations, and the hypocentral origin time of the earthquake is obtained from P arrivals (Table 1). The origin-time error is expected to be less than 0.5 s due to the 1D-like structure of the Sichuan basin. Theoretically, the group dispersion measurement should be based on centroid origin time (the hypocentral origin plus half of the source duration); however, for the Suining earthquake with magnitude less than M 5, the time difference is expected to be minor (less than 0.5 s).

3.4 Results

Various studies demonstrated that directivity of the noise field is mostly from coastal toward inland regions (Stehly *et al.* , 2006), and the directivity is thought to have some bias on surface-wave dispersion. Therefore, we first compare dispersion for stations near the sea (TATO and HKPS) and then for stations far inland (AAK and KURK, in central Asia). NCF waveforms and earthquake waveforms are displayed on the left side of Figure 3.2, and comparisons of the group velocity dispersion measured from NCFs and the earthquake waveforms are displayed on the right. In this figure, all four stations are at least 1000 km away from the earthquake (and from station SNI), and we refer to this distance range (1000 km) as "far distances". Because studies that image the crust and upper mantle with the ambient seismic noise at regional or continental scale mostly use the period band between 5 and 40 s, we only present a comparison of surface wave dispersion for wave periods between 10 and 30 s. EGFs, including symmetrical (time-reversed) and one-sided (using the stronger energy branch) cross correlations, were used to compare dispersion measured from earthquake waveforms. From the left side of Figure 3.2, the Rayleigh waves in the NCFs waveforms overall match earthquake waveforms after being band-pass filtered between 10 and 30 s, and

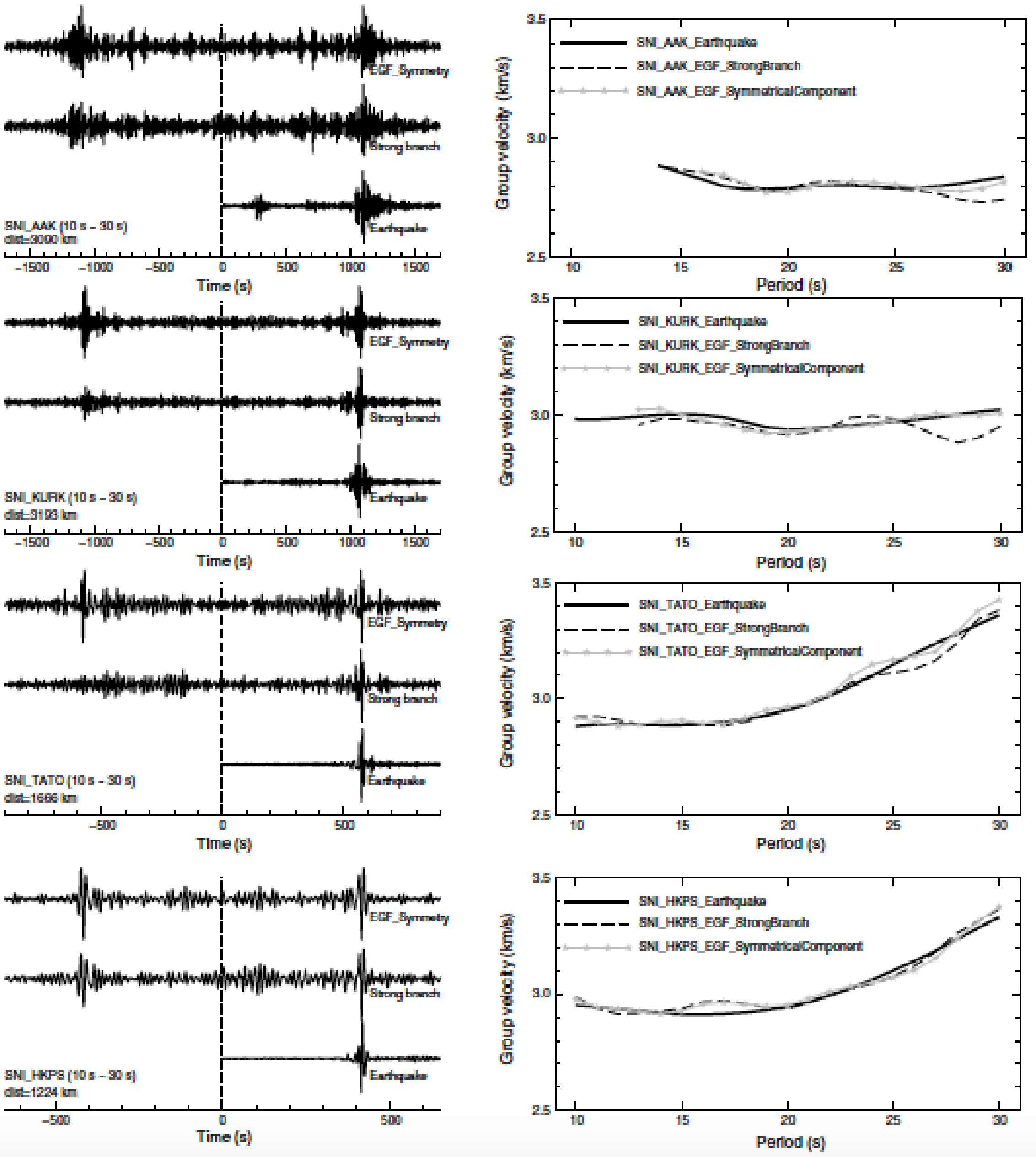

Figure 3.2: (Left) Noise correlation functions and surface-wave records at far stations (>1000 km) for stations AAK, KURK, TATO, and HKPS (from top to bottom). (Right) Rayleigh-wave group velocity dispersion curves measured from earthquake data (solid line), symmetric (starred lines), and one-sided (dashed lines) NCFs for the same four stations.

the Rayleigh wave group velocity dispersion curves from NCFs and the earthquake data also agree well with each other. Moreover, dispersion from symmetric NCFs matches dispersion from the earthquake data better than that measured on one-sided NCFs (the strong energy branch is chosen). The difference between dispersion from symmetric NCFs and earthquake data is mostly less than 0.03 km/s (or less than 1%), which falls in the error bounds of dispersion measurement in many ANT studies.

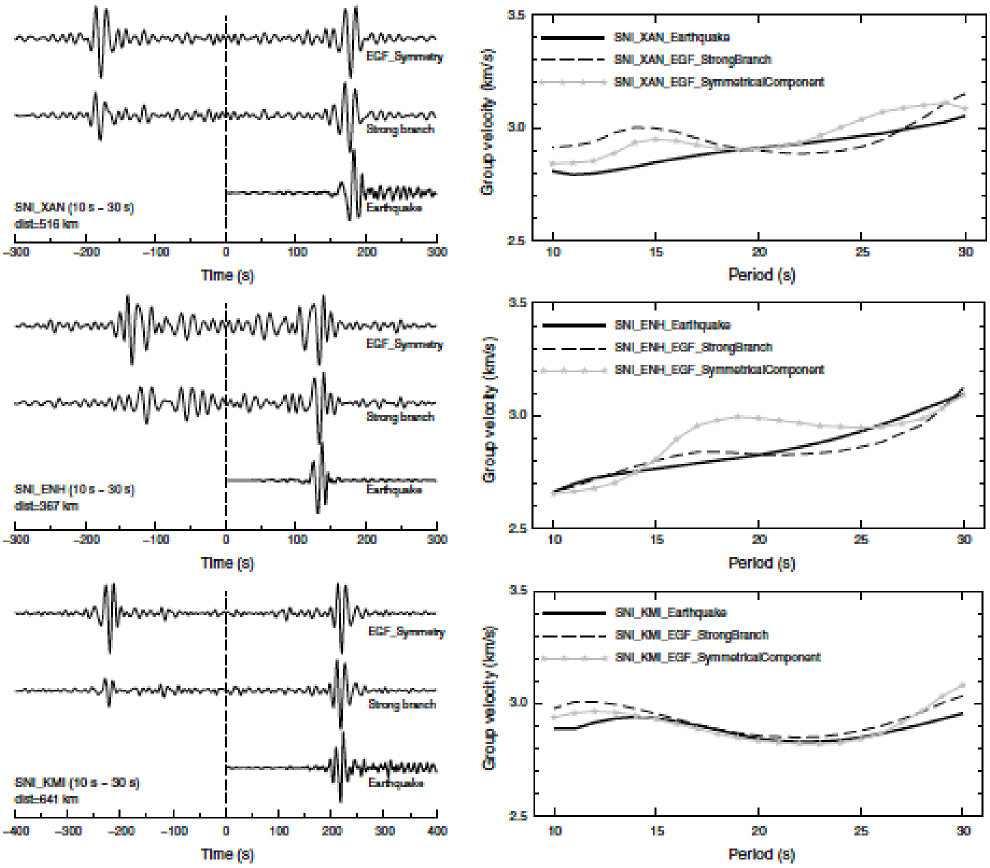

Figure 3.3: (Left) Noise correlation functions and surface-wave records at near stations (<1000 km) for stations XAN, ENH, and KMI (from top to bottom); interstation distances are 516, 367, and 641 km, respectively. (Right) Rayleigh-wave group velocity dispersion curves measured from earthquake data (solid line), symmetric (starred lines), and one-sided (dashed lines) NCFs for the same three stations.

Then we investigate the difference of Rayleigh-wave group velocity dispersion between NCFs and earthquakes for distances less than 1000 km. There are three permanent stations in GSN within 1000 km from the Suining earthquake: ENH (367 km), XAN (516 km), and KMI (641 km). Waveforms of NCFs and earthquake records are displayed on the left side of Figure 3.3, and a comparison of dispersion from NCFs and earthquakes is displayed on the right. Although the waveforms of NCFs and the earthquake have similar shape, dispersion measurements show noticeable differences. For the closest station (ENH), the difference in group velocity is larger than 0.2 km/s (or about 6%) at the period from 15 to 25 s. Unexpectedly, the dispersion curve extracted from one-sided NCFs is more similar to the one from the earthquake data than from symmetric NCFs. In contrast, for the XAN station, which lies to the northeast of SNI, the dispersion curves from symmetric NCFs. In contrast, for the XAN station, which lies to the northeast of SNI, the dispersion curves from symmetric NCFs and earthquake data match better, although still with difference up to 0.1 km/s (or 3%). For station XAN, dispersion from the one-sided NCF is different from that from the earthquake data up to 0.2 km/s, suggesting that symmetric NCFs produce more accurate dispersion than do one-sided NCFs for this station. For both ENH and XAN, a mismatch of 3% between dispersion from NCFs and earthquake data is observed. For KMI, which is southwest of SNI and further away, the match between dispersion measured from NCFs and earthquake data is much better than those for XAN and ENH.

As there are only three GSN stations within 1000 km, the observed mismatch is not statistically meaningful. We then processed data at 10 more stations from CENC, covering distances of 300-1000 km (Figure 3.4), for a total of 13 stations within 1000 km. We observe that 9 of the 13 stations show a good match between earthquake and noise dispersions (the group velocity difference is within 0.1 km/s). Only four stations show differences up to 0.2 km/s (ENH, XAN, GSWXT, and SCSPA).

Seats *et al.* (2012) demonstrated that the accuracy of NCFs also depends on the time span of ambient seismic noise data; therefore, we compare dispersion from the earthquake and from NCFs for different time spans of noise data. In Figure 3.5, dispersion curves from NCFs computed with 3-month data, 6-month data, and all the 15-month data are compared with the dispersion from earthquake data for stations AAK and ENH. Indeed, there are some differences between dispersion from NCFs of different time spans, but the three dispersion curves are overall very similar. For AAK (epicentral distance of 3090 km), dispersion curves from NCFs of all three time spans match the earthquake data measurements well. In contrast, for ENH, the mismatch between the dispersion curves from NCFs and the earthquake data

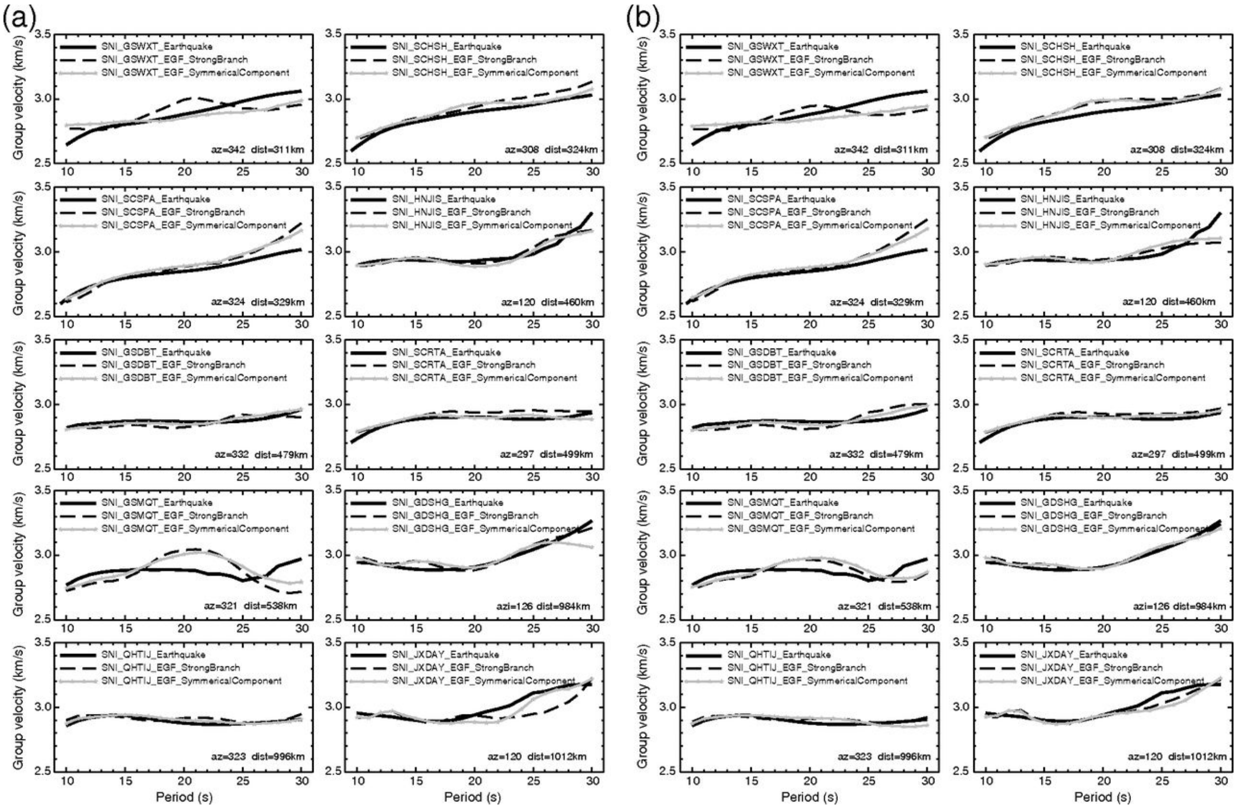

Figure 3.4: Comparison of group velocity dispersion between earthquake data (solid) and NCFs (dashed line, the stronger branch of onesided NCFs; starred line, symmetric NCFs). (a) NCFs are retrieved from normalized noise with the time-domain running-average method (Bensen *et al.* , 2007). (b) NCFs are retrieved from noise data without the time-domain running-average method.

persists for all three time spans. Therefore, differences in group velocity dispersion between NCF and earthquake data should be a stable feature for ENH and XAN and is not due to a limited time span of noise data. Yang & Ritzwoller (2008) also propose that noisy data longer than one year usually led to stable NCFs.

3.5 Discussion

The difference between dispersion from NCFs and earthquake data might be due also to differences in source mechanisms and focal depth. NCFs between vertical components approximate the Green's function with vertical single forces loading on one of the stations, whereas the earthquake source is usually double couple and buried at depth. To explore the effects due to differences in source mechanism and focal depth, we compute synthetic

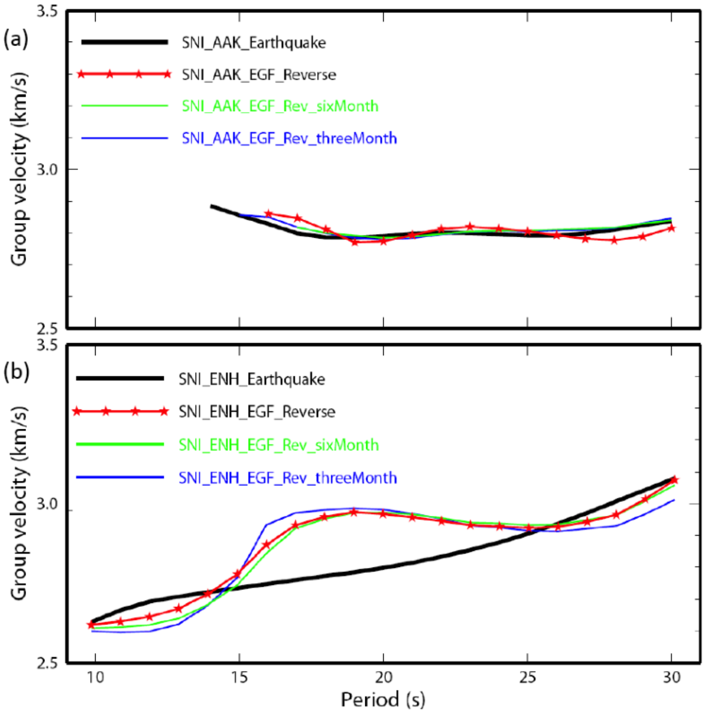

FIGURE 3.5: (a) Group velocity dispersion curves from earthquake data (black) and from the NCF between stations SNI and AAK for different time spans (red, symmetric NCF from the whole 15 months of noise data; green, symmetric NCFs from six months of noise data; blue, symmetric NCF from three months of noise data). (b) Same as (a), but for the station pair SNI-ENH.

seismograms at station ENH for a source located at the portable station SNI with a single vertical force acting on the free surface and for a double-couple source with focal depths from 1 to 11 km. The focal mechanism for the Suining earthquake (strike/dip/rake 356°/69°/95°) is taken from Luo *et al.* (2011). Velocity model by Xie *et al.* (2012) is used in computing the synthetic seismograms. We next measured the difference between Rayleigh-wave group velocity from the synthetic seismograms for the single force and double-couple source. From Figure 3.6, the difference in dispersion due to single force and double couple is small (<0.03 km/s) for shallow depth (<5 km) for the 10-30 s period. Therefore, for the Suining earthquake, which is very shallow (<2 km (Luo *et al.* , 2011)), the difference in dispersion from NCF and earthquake data at ENH is not due to differences in source mechanism and focal depth. This is also consistent with the study by Levshin *et al.* (1999), who proposed that source effects are not pronounced at short periods when measuring Rayleigh-group velocities.

The group velocity dispersion mismatch at station ENH could be partly due to the low

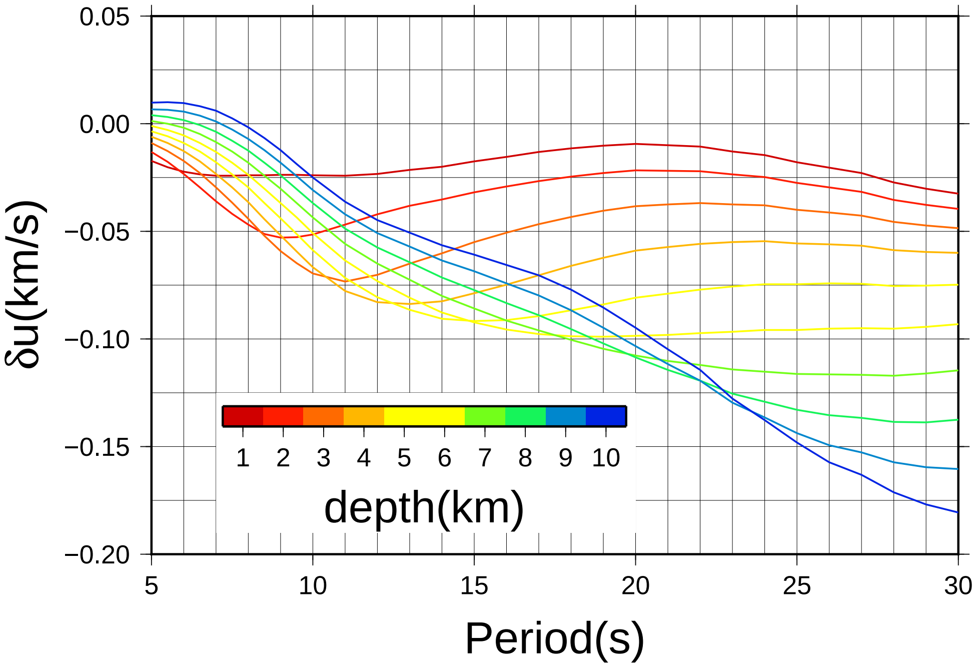

Figure 3.6: Group velocity difference between synthetic double couple source at difference depth and single force applying at the surface of the centroid of the earthquake. The distance of the station is 359 km (same as the distance between the earthquake and station ENH).

SNR of surface waves on the NCF (Figure 3.3). In order to test the possible link between SNR and dispersion mismatch, we compute the SNR and dispersion mismatch for all 17 stations. The SNR of the NCF is defined as the ratio between the peak amplitude of an inter-station Rayleigh wave and the standard deviation of the NCF data for the time window before the arrival of the Rayleigh wave. The dispersion mismatch is defined as the standard deviation of the difference between earthquake and noise Rayleigh-wave group dispersion for the period between 10 and 30 s.

As expected, the dispersion mismatch generally decreases with larger SNR, but with some scattering (Figure 3.7). Therefore, SNR could be one of the factors in causing the mismatch. We also test another line of evidence for the role of SNR in causing the group dispersion match by comparing phase velocity dispersion at ENH, because phase velocity dispersion measurement is usually more stable in the low-SNR situation. Because phase velocity dispersion measurement depends on earthquake source parameters, we calibrate the earthquake source parameter effects using a similar approach to group velocity dispersion calibration.

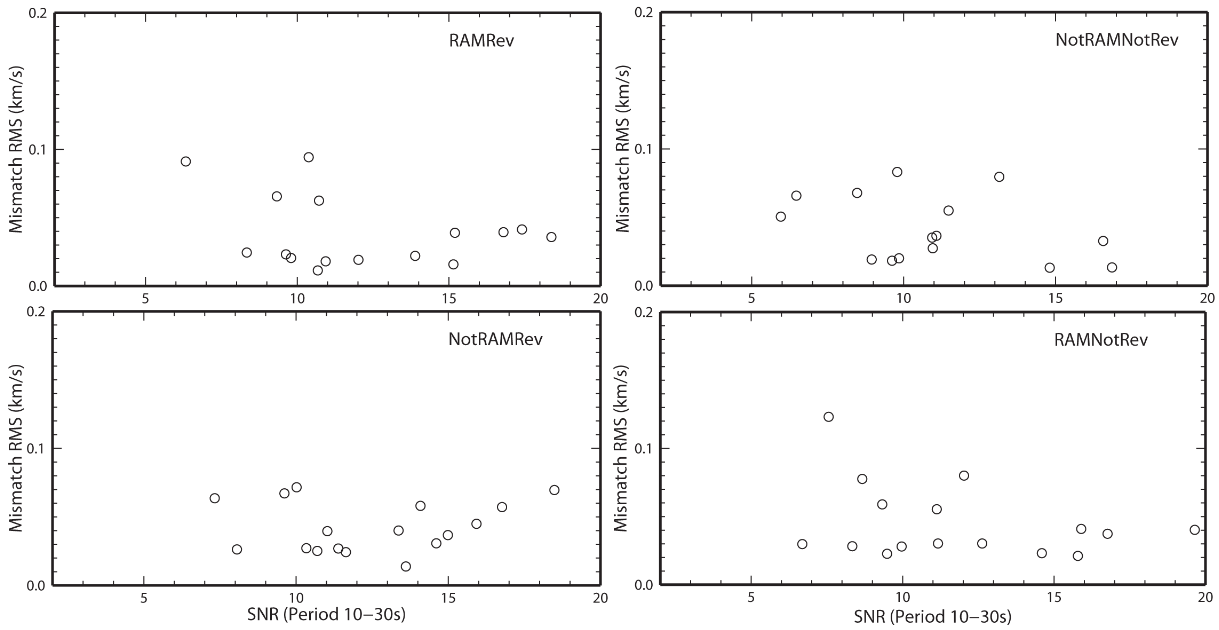

Figure 3.7: Mismatch of group velocity dispersion between earthquake and noise data versus SNR of the noise correlation function (NCF). "Mismatch" is defined as the standard deviation of the difference between the dispersions for the whole band (10-30 s). The label in each panel (RAM or notRAM, REV or notREV) denotes whether running average method is applied in time domain normalization and whether symmetric NCFs (REV) or one-sided NCFs (notREV) are involved.

The match in phase velocity is much better than that for group velocity, supporting the proposition that high-SNR NCFs are necessary for accurate ambient-noise group velocity dispersion. However, there is a small systematic difference of about 0.1 km/s (Figure 3.8) for the whole period band (10-30 s). Because source terms (focal mechanism and depth) have been taken into account, one of the factors for the phase velocity difference could be inaccurate origin time. But origin time cannot fully account for the mismatch, because inaccurate origin time would bias group velocity measurement in the same way as phase velocity measurement and group velocity mismatch for most stations is less than 0.1 km/s. The systematic difference in phase velocity mismatch between earthquake and noise data at ENH suggests that NCF may serve as a very good approximation of Green's function, instead of an exact solution to it.

Though group velocity dispersion from NCFs is consistent with earthquake data, there are some stations showing observable mismatch at short distances (300-500 km). The distance effect on the discrepancy between dispersion from NCFs and earthquake data might be due

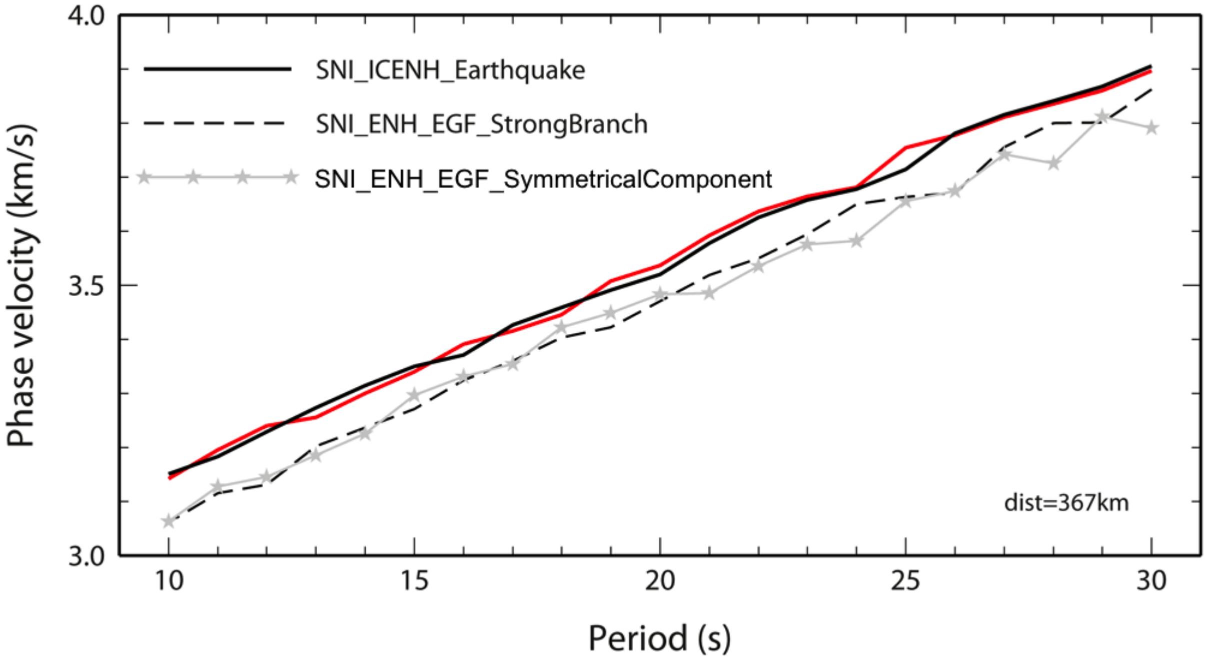

Figure 3.8: Comparison of phase velocity dispersion between earthquake data after correction for focal depth (black solid line for depth of 0.6 km and red line for depth of 2.0 km) and NCFs (dashed line for the stronger branch of one-sided NCF, and starred line for symmetric NCF) at station ENH. The phase velocity dispersion from earthquake data was calibrated for effects due to earthquake focal mechanism and focal depth.

to two effects: the dependence of Fresnel's zone upon inter-station distance or the spatial distribution of the ambient seismic noise field. Therefore, NCFs at shorter distances are more sensitive to inhomogeneity in the ambient noise field. Alternatively, the seismic noise field could be less diffusive for small regions (a few hundred kilometres or less) than at longer distances (1000 km or longer). As the seismic noise field is hypothesised to be partly caused by random scattering in the crust (Shapiro & Campillo, 2004), a length scale of a few hundred kilometres might not be enough for scattered wave to be completely diffusive, assuming a mean free path of 100 km (Wu, 1985). To decipher which factor is responsible for the distance effect on surface-wave dispersion mismatch, NCFs between two dense arrays may be helpful for assessing diffusivity of the ambient noise field and for quantifying Fresnel's zone effects.

The match between dispersion from NCFs and earthquake data reaffirms that NCFs provide valuable tools for tomographic studies. But the mismatch in dispersion measurements between noise and earthquake data at some short distances demands more systematic studies to validate the accuracy of NCFs as an accurate proxy of Green's functions.

3.6 conclusion

A broadband digital seismograph was installed in the epicentral region of the 2010 Suining Ms 4.8 earthquake, which occurred in the Sichuan basin of China. The ground-truth location of the event is accurately resolved with InSAR. NCFs of vertical-component seismic noises were calculated with 15 months of data between this station with 17 remote ones, and the Rayleigh-wave group velocity dispersion curves from the 10 to 30 s period were measured using the multiple-filter analysis technique. Dispersion curves from NCFs match those from earthquake data for most stations. The match is particularly good for large inter-station distances (1000 km+), but there are noticeable differences for smaller distances (<∼500 km) at some stations.

The overall match between dispersion curves from the earthquake data and the NCFs reaffirms that ANT is reliable. However, our study only involves comparison between dispersion from earthquake data and noise data for one ground-truth location event. Over the long term, more similar studies installing seismic stations in the epicentral region of ground-truth location events are necessary in many regions worldwide to systematically investigate the accuracy of NCF as a proxy of Green's functions. Very shallow moderate earthquakes (M5 or less) are ideal for this purpose because their ground-truth locations can be accurately resolved with InSAR, and their rupture length is small (usually less than 3 km). Quite a few such events have been identified in stable cratonic regions such as Australia Dawson *et al.* (2008); these events would provide valuable opportunities for testing the accuracy of ANT.

4

On the accuracy of long-period Rayleigh waves extracted from ambient noise

4.1 Summary

The aim of this paper is to assess the accuracy of the long-period (50-250 s) surface waves extracted from cross-correlation functions (CCF) of ambient noise. First, we compare waveforms of Empirical Green's functions (EGF) converted from CCF with their synthetics, and also compare seismograms from a ground truth earthquake with their synthetics, through numerical simulations using a common 3-D model. We then quantify the accuracy of EGFs by comparing two sets of time-shifts between the observed waveforms and the synthetics: one set for the ground truth earthquake and the other set for EGFs. Second, we compare Rayleigh wave phase velocity dispersion measurements from ambient noise and those from

earthquake data in both global and regional studies. Through these comparisons, we conclude that both the dispersion curves and waveforms from noise data are consistent with their counterparts from earthquake data in the long-period band. The long-period surface waves from ambient noise are as accurate as those from earthquake data, and can be included in both global and regional ambient noise tomography and provide complementary data to constrain the lithospheric and asthenospheric structures.

4.2 Introduction

Since Campillo & Paul (2003) and Shapiro & Campillo (2004) have demonstrated that surface wave empirical Green's function (EGF) between a pair of stations can be extracted from cross-correlation function (CCF) of earthquake coda waves or ambient seismic noise, studies based on EGF have extended into many areas, including ambient noise surface wave tomography (ANT) (e.g., Bensen *et al.* , 2008), monitoring velocity changes of Earth's media (e.g., Brenguier *et al.* , 2008), detecting the inner clock error of seismometers (Stehly *et al.* (2007); Xia *et al.* (2015)), testing tomographic earth models (e.g., Ma *et al.* , 2008) and calibrating earthquake centroid location (Barmin *et al.* , 2011; Xie *et al.* , 2011; Zhan *et al.* , 2011). EGF from ambient noise provides an effective and efficient tool to explore the Earth in complementary to earthquake data. Because EGF can be obtained from continuous waveform data of a pair of stations, ANT based on EGFs provides better ray coverage via deploying portable seismic arrays and overcomes the limitation of uncertainties of earthquake source parameters in earthquake-based tomography, such as, location, depth and original time. In the past decade, ANT has become a well-established method in imaging crustal structure and uppermost mantle structure.

However, to date, most of ANT studies focus on short-period surface waves with period ranging from a few second to ∼50 s which are mostly sensitive to the crustal and uppermost mantle structure. The period range is often used because ambient seismic noise in this period band is particularly energetic with the noise sources dominated by microseisms from oceans, so-called single frequency microseism (10-20 s) and double frequency microseism (5-10 s). Long period (>50 s) ambient seismic noise, usually known as Earth's seismic hum, is

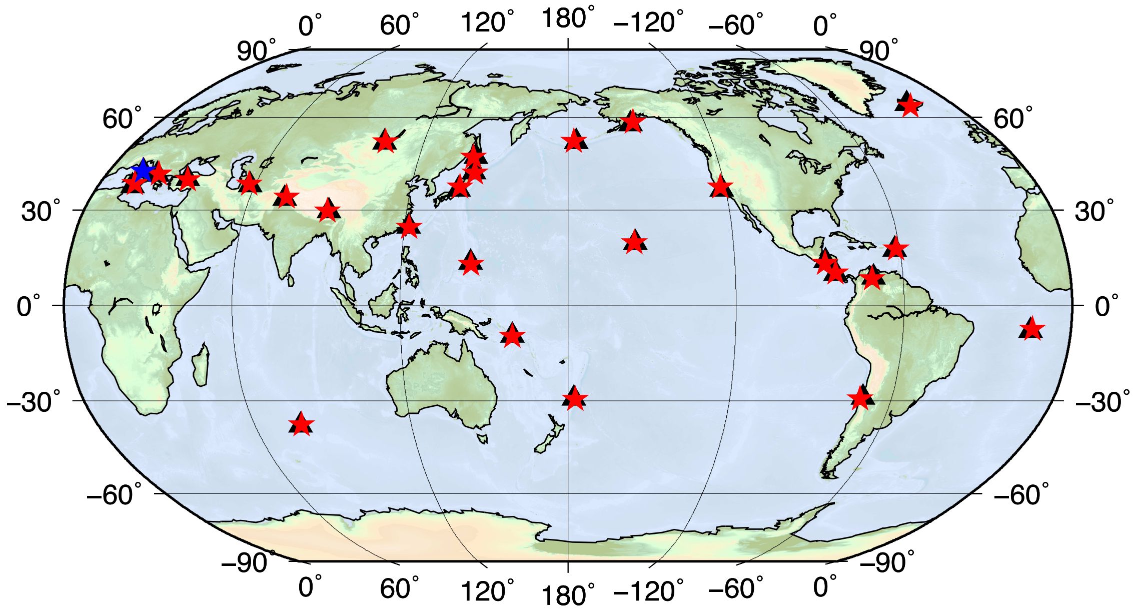

Figure 4.1: Distribution of the stations (black triangles) and events (red stars). The blue star is the L'Aquila earthquake occurred in Italy at April 6th, 2009. Actually there are a lot of station and event pairs in Ekström (2011) which are 100 km close with each other 100 km and some stations are 100 km close, here we only retain the closest station-event pairs to minimise the bias.

also observed at globally distributed stations. It is suggested that the dominant sources of seismic hum are the ocean infragravity waves. The possible excitation mechanism of the hum is the random shear traction on the seafloor induced by the infragravity waves, which has much weaker energy compared to the microseismic band (Nishida, 2013). Long-period EGF gets much less attention in ANT, even though a few studies have shown that long-period surface waves (>50 s) can also be extracted from the earth hum (e.g., Nishida *et al.* , 2009; Schimmel *et al.* , 2011; Shen *et al.* , 2012b; Yang, 2014) and can be used in regional (Yang, 2014) and global surface wave tomography studies (Nishida *et al.* , 2009). Long-period surface waves (50-250 s) are used in imaging the lithosphere and asthenosphere structure. Traditionally, long-period surface waves are obtained from teleseismic earthquakes. However, most large earthquakes occur at plate boundaries, leading to uneven distribution of ray coverage in earthquake-based surface wave tomography and in turn limiting the resolution of surface wave tomography. Surface waves extracted from ambient noise recorded at a pair of stations are free of these problems. However, applications using long-period surface waves from the earth hum to perform ANT are still very limited. That is probably because the signal-to-noise ratio (SNR) of EGF from ambient noise peaks at around 15-25 s periods (e.g., Yang & Ritzwoller, 2008) and decreases towards longer periods, and the errors of phase velocity measurements at long periods could become larger. In this case, errors of long-period dispersion measurements of surface waves from noise are of great concern in ANT studies. In this study, we investigate whether dispersion measurements of long-period surface waves (50-250 s) from ambient noise are compatible with those from earthquakes and whether they are accurate enough for tomography studies. First, we compare the differences between EGF waveforms from ambient noise and their synthetics with those differences between teleseismic waveforms from a ground truth earthquake and their synthetics. Then, we compare dispersion observations from ambient noise with those from earthquake data in both global and regional scales.

4.3 Double difference between real, theoretical earthquake data and EGF, theoretical Greens function

To verify the accuracy of long period surface waves from CCFs, the straightforward approach is to compare the EGF waveforms from ambient noise with true Greens Functions (GF) from powerful localized seismic sources such as earthquakes or explosions. However, there are very few strong natural surface sources of vertical single force, which can excite Greens Functions of long period (>50 s) surface waves. Instead, we can retrieve GF from earthquake seismograms, which are the convolution of GF with earthquake source function and instrument responses. In order to extract the GF from earthquake data, both the instrument response and the source term have to be removed from raw earthquake seismograms. The instrument response is usually known from seismometer manufacturers, and the earthquake source term can be calculated if the earthquake focal mechanism and epicentre location are known. Thanks to progress in Interferometric Synthetic Aperture Radar (InSAR) and GPS techniques, a moderate earthquake (with magnitude about M6) occurring in the shallow crust can be accurately located, and the focal mechanism can be well determined in combination of seismic waveforms (Lohman *et al.* , 2002). One of such events is the 6th

April 2009 Mw 6.3 L'Aquila earthquake (Figure 4.1), which is chosen to be compared with EGF from ambient noise in this study.

There are several reasons to choose this earthquake. Firstly, there is a station AQU/MN deployed very close to this event, about only 4.3 km away from the L'Aquila earthquake (13.449° E, 42.333° N). Secondly, both the centroid depth and focal mechanism of this earthquake are well determined with InSAR, GPS and seismic data (Cirella *et al.* , 2009; Pino & Di Luccio, 2009; Walters *et al.* , 2009). Thirdly, the magnitude (Mw 6.3) is moderate; therefore the earthquake can be treated as a point source at long periods, avoiding the complexity of finite fault. Fourthly, the centroid depth (7.3 km) of this earthquake is shallow, which guarantees that the strong fundamental-mode surface waves are excited and dominate in the seismograms.

However, although the ground truth location is well determined, the location of the earthquake and the closest station (AQU/MN) are not exactly co-located. Thus, if we want to directly compare the EGF from noise with GF from earthquake; we have to account for the difference of location between the station and the earthquake. In this study, rather than performing direct comparison, we compare two sets of waveform differences: one between observed and synthetic seismograms, and the other between observed and synthetic EGFs. If the 3D earth model used in the simulation of synthetic seismic waveforms and synthesis EGF is exactly accurate, both waveforms of earthquake data and EGFs should be matched and travel time differences of two pairs of data should be close to zero. However, if the 3D earth model is not perfect, the phase travel time differences between observed and synthetic waveforms of earthquake data and noise data would be similar because the earthquake source and the station are located very close to each other. Intuitively, the effects of 3D structures on phase travel time along the propagation path should be similar for both synthetic data, which is the case as illustrated below.

The synthetic earthquake waveforms and GF are computed with the SPECFEM3D_GLOBE package of the Spectral Element Method (SEM) (Tromp *et al.* , 2008). In our simulation, seismic waves are simulated down to 34 s because we are interested to investigate surface waves at periods longer than 50 s. The global model used in the simulation is constructed by taking the mantle model of S362ANI (Kustowski *et al.* , 2008) as the whole mantle part and the crustal model Crust2.0 as the crustal part (Bassin *et al.* , 2000). The focal mechanism (strike: 144°, dip: 54°, slip: -105°), and centroid depth (7.3 km), location (13.449E, 42.333N) of L'Aquila earthquake are taken from (Walters *et al.* , 2009). The source half duration is set to 3.5 s according to Global CMT (Dziewonski *et al.* , 1981). For the synthetic vertical Greens function simulation, a smooth vertical force with Gaussian time function ($f(t) = 1/\sqrt{t_0\pi}e^{(t/t_0)^2}$) is exerted on the surficial location of station AQU/MN (Ma *et al.* , 2008). Therefore, the synthetic waveforms for the vertical force correspond to the GFs convolved with the applied source time function.

In order to get the vertical-vertical EGF from station AQU/MN, the vertical ambient noise velocity records (with instrument response removed) between AQU/MN and remote GSN stations are cross-correlated using the standard ambient noise processing procedures described in Chapter 2, which gives rise to 126 station-to-station CCFs with good azimuthal coverage over the globe. Five years of continuous data from 2007 to 2012 are used in the cross-correlations to achieve high quality surface waves from ambient noise.

Here we give a very brief description of the standard ambient noise processing procedures. Continuous seismic waveform records are cut into one-day-long time series, and decimated into 1 sample per second. Linear trend, mean and instrument response are removed, and then filtered with band pass between 5 s and 300 s. Next, in order to remove unwanted signals (earthquake events and instrumental irregularities), running average is applied, which is also known as the time domain normalisation. Running average has proven to be a robust method to suppress unwanted signals. The temporally normalised signals are then whitened in the frequency domain to broaden the frequency range. Then cross-correlation is performed for each day, and is stacked linearly to get monthly CCF, which are then further stacked to get the final CCFs. The EGF is derived from the negative time-derivative of symmetry CCF (e.g., Lobkis & Weaver, 2001; Roux *et al.* , 2005; Snieder, 2004). The final EGFs are convolved with the Gaussian time function when compared to the simulated GF.

Figure 4.2 illustrates the vertical components of observed and synthetic waveform from earthquakes and noise. All of the waveforms are band-pass filtered between 50-300 s periods. Both of the EGF and earthquake waveforms are well matched by the corresponding synthetic

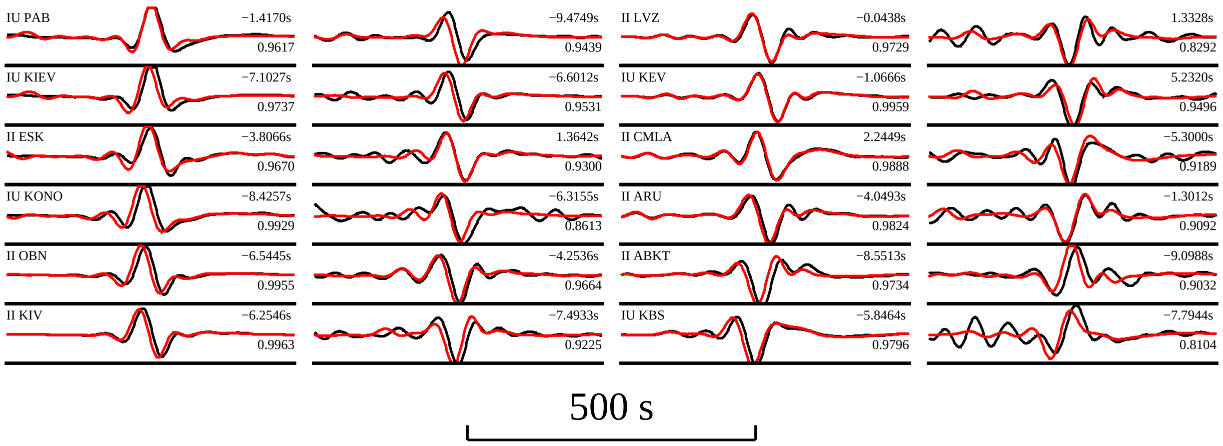

Figure 4.2: Examples of waveform comparisons between observed earthquake data (6th April 2009 Mw 6.3 L'Aquila earthquake), synthetic seismograms (column 1 and 3) and EGF from CCFs, synthetic EGFs (surface load of vertical single force simulations) (column 2 and 4), respectively. The synthetic waveforms using SEM are shown with red lines , and observed data withblack lines. All the waveforms are band-pass filtered in period band between 50-300 sec. The distances (in degree) are showing in the left bottom corner. The time shifts in the upper right corner are calculated based on cross-correlation, and the cross-correlation coefficients are in the right bottom corner.

data. However, there are noticeable time shifts between the synthetic and observed waveforms for both earthquake and EGF waveforms, which are likely caused by the imperfect 3D model used in the simulation. As discussed in the previous paragraph, if this is the case, the time shifts between the synthetics and observations for both earthquake data and EGF should be similar.

To compare the two sets of time difference, we measure the time shifts between synthetic and observed waveforms using the cross-correlation method. In the cross-correlation, surface wave time window is defined with 1200 s length centred at the peak amplitude of surface wave. The calculated time shifts between synthetic and observed waveforms for both earthquake data and EGF from ambient noise are plotted in Figure 4.3. Only those measurements with cross-correlation coefficients greater than 0.85 are included for comparison. As expected, the two time shifts are close to the diagonal line of equal difference, indicating both seismic waveforms and EGF from noise are matched nearly equally well by the synthetic data. This furthermore implies that EGF from noise can match nearly surface wave dispersion features along the propagating paths, that is, the phase travel times measured from EGFs are consistent with those from real earthquake seismograms.

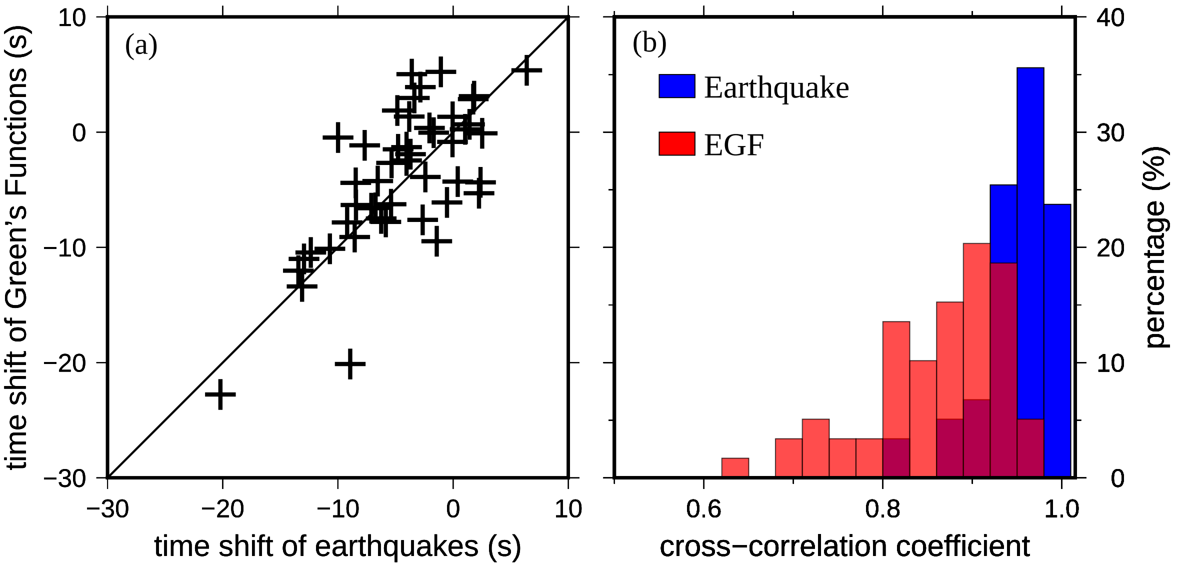

Figure 4.3: The time shifts of the earthquake Rayleigh waves versus Greens Functions (Figure 4.2). To guarantee the quality of data, only cross-correlation coefficient bigger than 0.85 are retained.

4.4 Phase velocity comparison between Earthquakes and NCFs for global data set

Although a ground-truth earthquake provide the valuable opportunity to verify the accuracy of surface waves from ambient noise with respect to earthquakes, the number of ground-truth event pairs like the case described above is rare. With only several tens of measurements used in the comparison (Figure 4.2), it is not sufficiently convincing to make conclusion about the accuracy of surface waves from ambient noise. Since there are not enough ground true earthquakes near seismographic stations available for comparison, we compare surface wave dispersion curves extracted from earthquake data and CCFs of ambient noise. We first demonstrate comparison of these dispersion data on a global scale.

Table 4.1: 27 stations and events information.

Earthquake ID	Station name	Event longitude (°)	Event latitude (°)	Station longitude (°)	Station latitude (°)	Distance (km)

200904071747A	AQU-MN	13.390	42.310	13.405	42.354	4.919
200901081921A	HDC-G	-84.110	10.230	-84.112	10.000	25.653
200808270135A	TLY-II	104.020	51.760	103.644	51.681	27.298
010800A	HNR-IU	159.990	-9.780	159.947	-9.439	38.163
051502B	TATO-IU	121.660	24.660	121.497	24.973	38.605
200909062149A	TIR-MN	20.360	41.370	19.863	41.347	41.562
200712262347A	ANTO-IU	33.050	39.550	32.793	39.868	41.562
200702010014A	AIS-G	77.980	-37.590	77.569	-37.797	42.880
200610151707A	POHA-IU	-155.940	19.830	-155.533	19.757	43.161
092503K	ERM-II	143.620	41.750	143.157	42.015	48.343
200810081407A	LSA-IC	90.570	29.760	91.127	29.703	54.106
082200D	ABKT-II	57.570	38.180	58.119	37.930	55.518
102700D	ANWB-CU	-61.240	17.760	-61.786	17.669	58.654
200805020133A	ADK-IU	-177.540	51.960	-176.684	51.882	59.310
043002A	RAO-IU	-177.390	-29.550	-177.929	-29.245	62.372
200902200348A	NIL-II	73.790	34.140	73.269	33.651	72.557
200708020237A	YSS-IU	141.820	46.840	142.760	46.959	72.624
122101B	SDV-IU	-71.110	8.400	-70.634	8.884	75.048
071201A	ASCN-II	-13.760	-7.520	-14.360	-7.933	80.463
101201E	GUMO-IU	145.080	12.880	144.868	13.589	82.070

062100A	BORG-II	-20.850	63.980	-21.327	64.747	88.263
012004B	KDAK-II	-151.440	58.330	-152.583	57.783	90.590
102304L	MAJO-IU	138.740	37.250	138.204	36.546	91.652
200710310304A	SCZ-G	-121.780	37.370	-121.403	36.598	92.126
200511281633A	LCO-IU	-71.540	-29.450	-70.700	-29.011	94.996
200602200656A	TGUH-CU	-87.620	13.240	-87.273	14.057	98.276
090602A	CLTB-MN	13.570	38.420	13.216	37.578	98.620

We choose Rayleigh wave dispersion curves collected by Ekström (2011) from the earthquakes. Ekström (2011) extracted one-station surface wave dispersion measurements from 3300 earthquakes to construct global surface wave dispersion maps (GDM52) at 25 to 250 s periods for both fundamental-mode Rayleigh wave and Love wave. In their data set, there are 27 earthquakes (Figure 4.1, table 4.1) which happens to be near a broadband seismic station within distance of 100 km. If we extract surface wave dispersion curves from ambient noise cross-correlations of those 27 stations with other stations, these 27 stations can be treated as virtual sources. Then, similar to the comparison in the previous section, the effect on heterogeneities along tele-seismic paths from the source/station to another station should be similar, because the location of earthquakes and stations are very close to each other. In other words, the dispersion curves from earthquakes and EGFs at the remote stations should be similar to each other if the long period dispersion measurements from EGFs are accurate.

To obtain long period dispersion measurements from ambient noise, we calculate the

---

[a] Actually, there are a lot of station-event pairs which are 100 km close with each other, and some stations are 100 km with each other, we only retain the closest station-event pairs to minimise the bias.

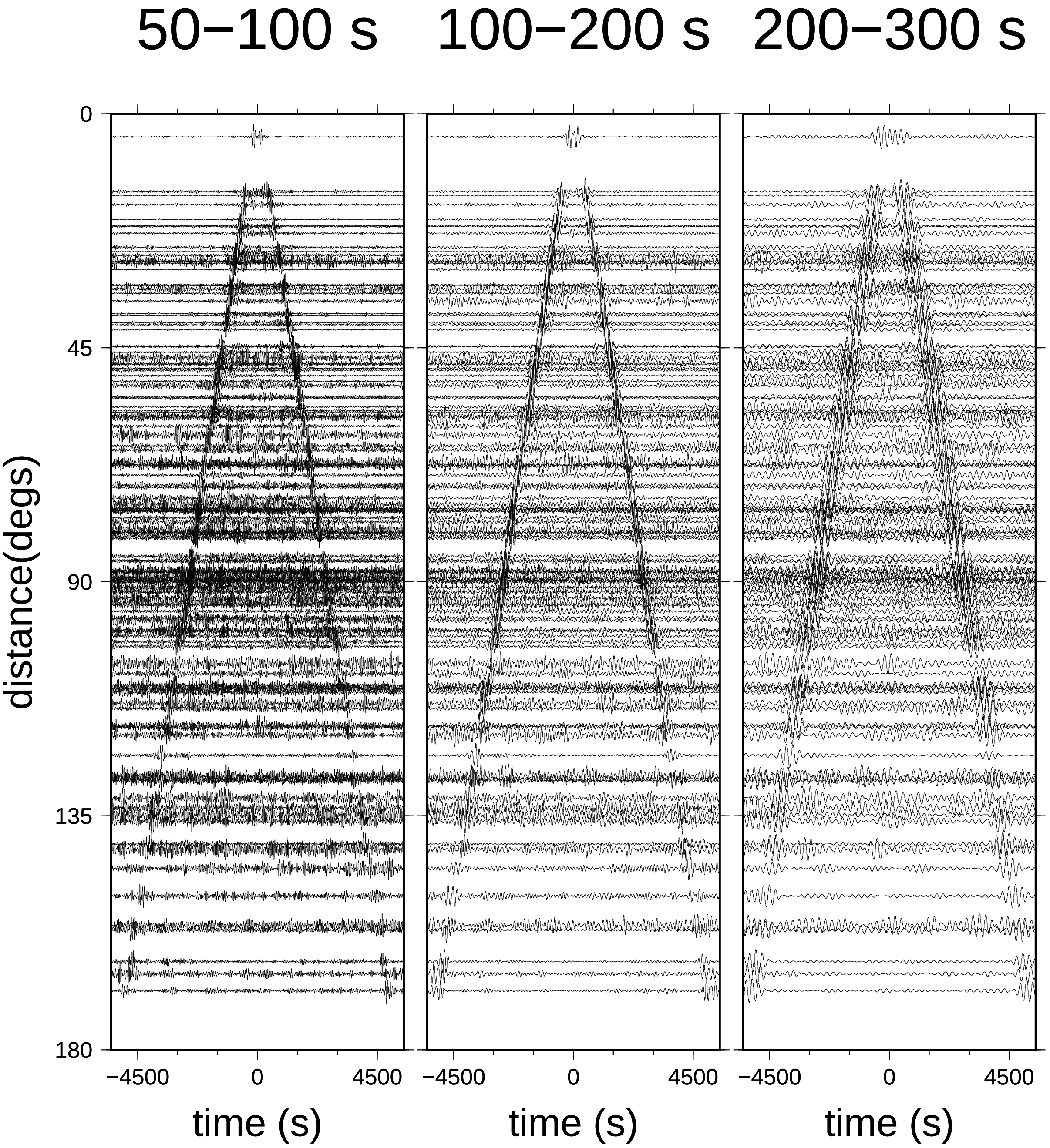

Figure 4.4: CCFs between station II/TLY and other GSN stations. The waveforms are bandpass filtered in period band of 50-100sec, 100-200sec and 200-300sec respectively. The surface wave is obvious on both negative lags and positive lags and shows almost symmetric amplitude.

NCFs between these 27 stations (Figure 4.1, table 4.1) with 126 stations from Global Seismic Network (II, IU), which gives rise to 3402 inter-station NCFs with good azimuthal coverage over the globe. NCFs are retained with their inter-station distances between 25° and 150°, consistent with the cut-off distance for earthquakes data in Ekström (2011)). Only Rayleigh waves are considered in our subsequent analysis, thus six years (2006-2011) of continuous vertical components of seismic records are processed for cross-correlations. The data processing procedures are same as those described in the previous section.

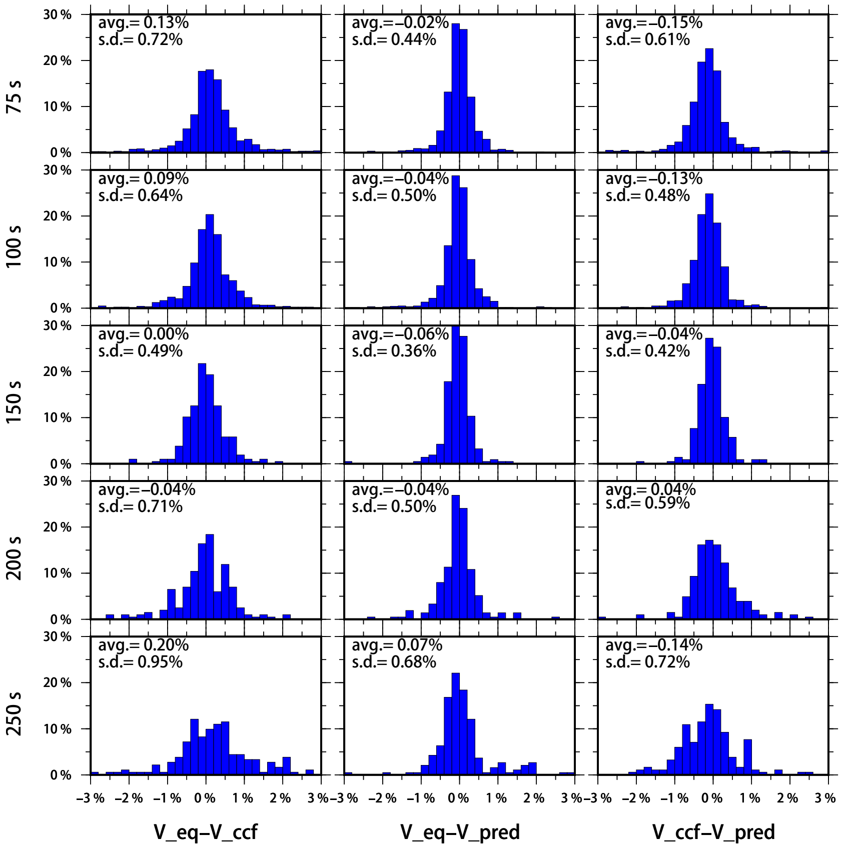

Figure 4.5: The left column shows the phase velocity difference between earthquake measurements (Ekström, 2011) (V_eq) and NCFs (V_ccf) for period from 75 s to 250 s. The middle column shows the phase velocity difference between earthquake measurements and prediction (V_pred) using program GDM52 (Ekström, 2011). The right column is the phase velocity dispersion difference between V_ccf and V_pred. The outliers with difference greater than 3% are discarded due to unrelated Gaussian distribution. It demonstrates that the phase velocity dispersion curves from NCF are very close with the phase velocity from earthquakes with the difference around 0.1%.

Examples of NCFs between station TFY/II and the other GSN stations are shown in Figure 4.4. Obvious coherent fundamental surface wave signals show up on both positive and negative legs with normal dispersion characteristics (With longer period surface waves arrive earlier than shorter periods). Signals on both negative and positive legs have almost the same amplitude, indicating that the earth hum in this period band is nearly diffusive. We add the negative and positive lags together to form the symmetric component in order to improve the SNR (Yang *et al.* , 2007). The inter-station dispersion curves are then measured using an automated, frequency-time analysis method (FTAN) (Bensen *et al.* , 2007). Only those NCFs with SNR larger than 10 are retained for dispersions analysis. The SNR is determined in the same way as Yang & Ritzwoller (2008), which is defined as the ratio between the peak amplitude of the envelope of narrow band-pass filtered NCF and the root-mean-square of the trailer noise. During comparison with data of Ekström (2011), the numbers of final Rayleigh wave phase velocity measurements for each period are about several hundreds.

Rayleigh wave phase velocities from these 27 events are calculated based on phase anomalies by Ekström (2011). The phase anomalies of earthquake Rayleigh waves are measured with respect to prediction based on the PREM model (Dziewonski & Anderson, 1981), through phase-matched filtering and minimisation of residual dispersion between an observed waveform and a synthetic one of fundamental mode surface wave.

We compare the phase velocity differences between earthquakes measurements (denoted as V_eq) and NCFs (denoted as V_ccf) for period range of 75 to 250 s (column 1, Figure 4.5). The phase velocity differences are normalised, for example the difference between V_eq and V_ccf (column 1 of Figure 4.5) is evaluated by (V_eq-V_ccf)*100%/V_ccf. The distributions of the phase velocity differences nearly follow a Gaussian distribution, thus the means and the standard deviations are calculated (Figure 4.5). During the calculation, a few outliers with anomalies greater than 3% are discarded. The mean difference of V_eq and V_ccf is very close to zero, indicating that the phase velocities from NCFs are consistent with earthquake measurements.

Furthermore, to evaluate the uncertainty level of dispersion measurements from ambient noise, we calculate the predicted phase velocities from the tomographic maps of GDM52 and compare the predicted phase velocities with measurements from earthquake. The distributions of differences between V_eq and velocity predictions (denoted as V_pred) are plotted in the second column of Figure 4.5 and the phase velocity differences between V_ccf and

V_eq in the third column. And the means and the STDs of the difference are also calculated and shown. The distributions of differences between these two pairs of comparison are very similar, almost having nearly close to zero means and less than 1% STD, indicating again the long period dispersion measurements from earthquake and from noise are consistent with each and have similar levels of uncertainty. That also means the phase velocity measurements from CCFs can be incorporated in global tomography.

4.5 Phase velocity comparison between earthquakes and CCFs on regional scale

After demonstrating the accuracy of long period surface wave dispersion from noise data in global scale, we proceed to perform the comparison on a continental scale in USA using data from Earthscope/USArray.

We first compare dispersion curves from noise with those from two-station measurements of earthquakes based on a regional data set from Foster *et al.* (2014), who measure Rayleigh and love wave two-station phase velocities in Western United States in a period band from 25-100 s. Multiple phase velocity measurements from different earthquakes for one station pair are obtained by the two-station method in Foster *et al.* (2014). We take the mean velocity as the final value for comparison.

Following the data processing procedures of ambient noise as described in Chapter 2, we obtain NCFs from noise among TA, CI and US stations as used in Foster *et al.* (2014) and then measure the inter-station dispersion curves. We only select those dispersion measurements with inter-station distance longer than one wavelengths and SNR larger than 10 for comparison. Thanks to the large number of USArray/TA stations, we obtain over 170,000 of paths for the comparison. Figure 4.6 shows the histograms of phase velocity differences between NCFs from noise and two-station measurements at 50-100 s period (Foster *et al.* , 2014). The differences between these two data sets exhibit nearly Gaussian distributions with the largest mean of difference less than 15m/s, which is about 0.38% for typical phase

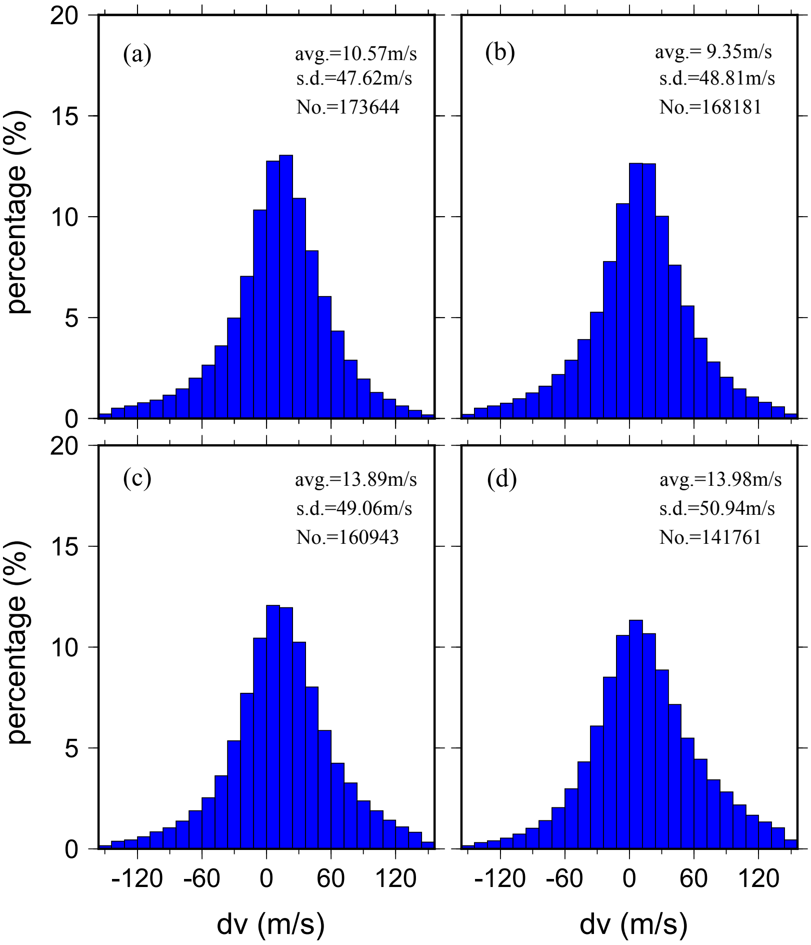

Figure 4.6: The Rayleigh wave phase velocity differences between the measurements from two-station method (Foster *et al.* , 2014) and NCFs of the western United States. Positive value indicates that the phase velocity from two-station method is faster than that from NCFs. (a) (b) (c) (d) are for periods of 50 sec, 60 sec, 75 sec and 100 sec respectively.

velocity of 4 km/s in this period range. The standard deviations is about 50 m/s, alternatively close to relative difference of 1%. Positive values here represent that the phase velocity of two-station method measurement (Foster *et al.* , 2014) is faster than that from CCFs.

One issue worthy of notion is that the average of two-station measurements is slightly higher than the EGF phase velocities, about 10 m/s that is ∼0.25% of the average phase velocity. The differences between these two kinds of data could be due to the differences of their sensitivities to heterogeneities. Surface waves from CCFs are mainly sensitive to structures within the two stations; while for two-station measurements, the sensitives are not just confined in the inter-station regions, and they are also significantly sensitive to areas beyond the inter-station part (Vos *et al.* , 2013). In other words, for these long period surface waves, the finite frequency sensitivity kernel between two-station measurements and measurements from noise is different.

Another possible contribution to the difference could be due to the off-great-circle propagation of tele-seismic surface waves used in two-station measurements, which could lead to shorter propagating distances of surface waves recorded by a pair of stations than the inter-station distance. If the off-great-circle propagation is not corrected, two-station measurements would be higher than the structural phase velocity. That difference could reach 1.5% as observed by Yao *et al.* (2006) in comparing the dispersion measurements between earthquake data and noise data at 10-30 s periods. However, Foster *et al.* (2014) has corrected the effect of off-great-circle propagation on two-station measurements by finding the arrival angles of incoming surface waves using a mini-array method. Thus this effect should be not the main contributor.

4.6 Conclusion

In this paper, we have demonstrated that dispersion measurements of long-period Rayleigh waves from CCFs of ambient noise are consistent with those from earthquake data, through three comparisons: (1) comparison of CCFs waveforms and phase traveltimes with those of a ground truth earthquake, (2) comparison of phase velocity extracted from CCFs with single-station measurements form earthquakes on a global scale and (3) comparison of phase velocity extracted from CCFs with two-station measurements from earthquakes on a regional scale. The close match of data between CCFs and earthquake data in these comparisons suggests that dispersion measurements from long-period EGFs are as accurate as those from earthquake data and can be included in seismic tomography on both global and regional scales. These long-period surface waves extracted from noise provide us complementary data to image lithospheric and asthenospheric structures. They can improve the path coverage in tomography, especially in aseismic areas. In addition, these long-period surface waves can be extracted from station pairs with short interstation distances, like one or two wavelengths, and thus provide better constraints on small-scale deep structures.

5

3D shear wave velocity model of US continent constructed from broadband ambient noise tomography

5.1 Abstract

Since Shapiro *et al.* (2005) successfully applied ambient noise tomography (ANT) method to image the subsurface using group velocity maps in southern California, ANT has been widely used to study crustal structures. Compared to traditional earthquake surface wave tomography, ANT has many advantages as described in Chapter 1. However, most of the previous ANT research has concentrated on the use of period band between a few seconds to about 50 s.

In this chapter, we broaden the period range of ANT and demonstrate the feasibility of using broadband (10-150 s) Rayleigh wave phase velocity maps for imaging continental scale structures. Broadband Rayleigh waves are extracted from cross-correlations of ambient noise data between all the station pairs of USArray seismic stations. We extract the dispersion curves from these cross-correlations at the period bands of 10 to 150 s and generate Rayleigh wave phase velocity maps at 10-150 s periods. These broadband dispersion maps from ambient noise tomography are then used to construct the 3D lithospheric and asthenospheric velocity structures from the surface down to ∼300 km beneath the whole USA.

5.2 Introduction

Since ANT makes use of interstation surface waves extracted from cross-correlation of ambient noise recorded at a pair of stations, ANT reduces the dependence of traditional surface wave tomography on earthquake data. ANT has effectively become a tomography method in which data are controllable like that of active seismology. This is because the path coverage in ANT is completely controlled by the configurations of seismic stations.

To date, most ANT studies have focused on surface waves at periods shorter than 40/50 s because ambient noise in this period range is strong and surface waves with high signal-to-noise ratio (SNR) can be obtained. These periods are used to constrain the crustal structure (e.g., Ekström, 2014; Lin *et al.* , 2008; Luo *et al.* , 2012; Yang *et al.* , 2007). In order to constrain upper mantle structures, teleseismic surface wave tomography is usually used to obtain long-period surface waves. Then, the dispersion curve at short periods from ambient noise and at long periods from teleseismic surface wave tomography are combined together to constrain the whole lithosphere structure from the surface down to ∼200-300 km (e.g., Moschetti *et al.* , 2010; Porter *et al.* , 2016; Shen *et al.* , 2013; Yao *et al.* , 2008; Zhou *et al.* , 2012). However, due to different data and methods used in the ANT and teleseismic surface wave tomography, there are typically small gaps in dispersion curves at overlapping periods, around 20-40 s, between ANT and teleseismic surface wave tomography, leading to large uncertainties in the overlapping periods. In addition, uneven distributions of teleseismic events could result in uneven azimuthal coverage of paths in the study regions, leading to smearing in tomography.

ANT could overcome the above problems if we could obtain broadband dispersion curves from ambient noise data. Chapter 4 have demonstrated that the long-period surface waves from ambient noise are as accurate as those from earthquake data, and can be included in both global and regional ambient noise tomography.

In this chapter, we demonstrate the feasibility of generating broadband (10 -150s) Rayleigh surface wave phase velocity maps from ambient noise and use them to image the lithosphere and asthenosphere structure in a continental scale across the contiguous USA.

In North American continent, most of the previous surface wave tomography from both regional studies (e.g., Godey *et al.* , 2003), and global studies (e.g., Ekström, 2011; Ritzwoller *et al.* , 2002; Schaeffer & Lebedev, 2014; Trampert & Woodhouse, 2003) are based on teleseismic earthquakes. With the development of ANT and the installation of USAarray seismic stations, a number of ANT have been carried out to imagine the crust and upper mantle structures (e.g., Southern California Shapiro *et al.* (2005); Yang *et al.* (2011); the western US (Lin *et al.* , 2008; P. Moschetti *et al.* , 2007; Shen *et al.* , 2013); over US continent (Bensen *et al.* , 2008; Ekström, 2014)). These ANT studies mostly use surface waves at periods shorter than 50 s. In this thesis, broadband surface waves (10-150 s) from ambient noise recorded at all the USArray seismic stations were used for the first time to image the lithosphere and asthenosphere structures.

In this study, we calculate NCFs among all of the TA stations and the other permanent networks across the US continent, including CI (Caltech Regional Seismic Network), US (United States National Seismic Network), BK (Berkeley Digital Seismograph Network), II, IU (Global Seismograph Network), totaling 1895 stations. Broadband dispersion curves were measured from the resulting NCFs. This thesis follows a two-step method to invert them for the 3D shear wave velocity structure of the US continent. First, Rayleigh wave phase velocity maps were generated at 10-150 s using tomography methods. In the second step, we extract local dispersion curves at each geographic point from the phase velocity maps and invert for 1D depth profiles of isotropic shear wave velocity. All of the 1D depth profiles at individual grid points are assembled to form a 3D shear wave velocity model.

5.3 Data

The USArray Transportable Array (TA) uses 400 high-quality broadband seismographs to sweep across the entire United States from the west to the east. Each instrument is deployed in a temporary site for two years and then moved to another location. Upon completion in 2013, USArray achieve a nearly uniform seismic network with a station interval of ~75 km covering the whole United States, resulting in a total of more than 1800 station locations. Continuous ground motions from earthquake and ambient noise are all recorded by these stations.

Vertical component seismic noise data recorded at these seismic stations (Figure 5.1) operating from January, 2004 to December, 2014 are obtained from IRIS/DMC. All of the TA stations are deployed for 24 months, however, the actual length of the data varies due to the installation and down time of the stations. The other stations from the USArray reference Network are also used in this study. These station are permanent stations, so the ambient seismic noise recorded at these stations is continuous from 2004 to 2014.

We follow the procedures described in Chapter 2 to preprocess the ambient noise data for every single station, including cutting the continuous data to one-day segments, removing the instrumental response, mean and trend. Then time domain normalization is applied to suppress the earthquake signals and irregularities. In order to balance the energy spectrum, the spectral whitening in the period band of 5-800 s is performed, which helps expand the bandwidth of the automated broadband dispersion measurements (Bensen *et al.* , 2007).

After that, daily cross-correlations are computed between all station pairs and then linearly stacked to form the final NCFs (Figure 5.2). The negative and positive time lags of each NCF are folded and stacked to form the symmetric component. From the symmetric component of NCFs, phase velocities between 10 and 150 s period were measured using the Automatic Frequency and Time Analysis method (AFTAN) (Bensen *et al.* , 2007). During the phase velocity extraction the phase velocity model of Ekström (2011) was used as a reference to unwrap the measured phase.

In order to select reliable measurements for the subsequent tomography, we perform quality control based on three criteria. In most ANT study, the interstation distance is required

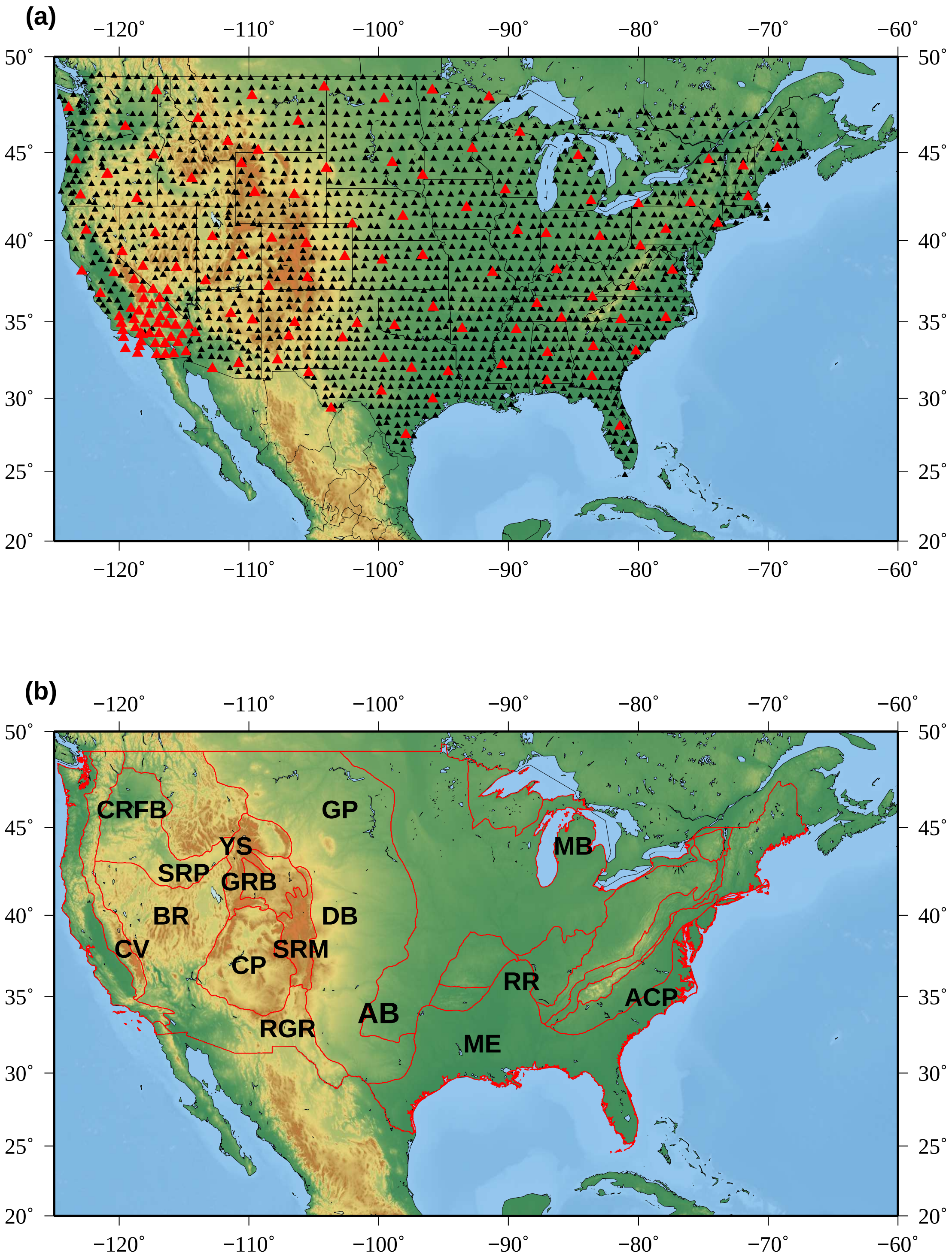
(a)
−120°
−110°
−100°
−90°
−80°
−70°
−60°
50°
45°
40°
35°
30°
25°
20°
(b)
CRFB
GP
YS
SRP
GRB
MB
BR
DB
CV
SRM
CP
RR
ACP
AB
RGR
ME

FIGURE 5.1: (a) The distribution of 1895 stations in US used in this study from USArray Transportable array stations (black triangle) and some other reference stations (red triangle). (b) Major geological units of Unite States modified from Fenneman (1917): Great Plain (GP), South Rocky Mountain (SRM), Basin and Range (BR), Yellowstone (YS), Rio Grande Rift (RGR), Central Valley (CV), Atlantic Coastal Plain (ACP), and Snake River Plain (SRP). Major sedimentary basins: Columbia River Sub-Flood Basalt sedimentary (CRFB), Anadarko Basin (AB), Denver Basin (DB), Green River Basin (GRB), Michigan Basin (MB), Mississippi Embayment (ME), Colorado Plateau and (CP).

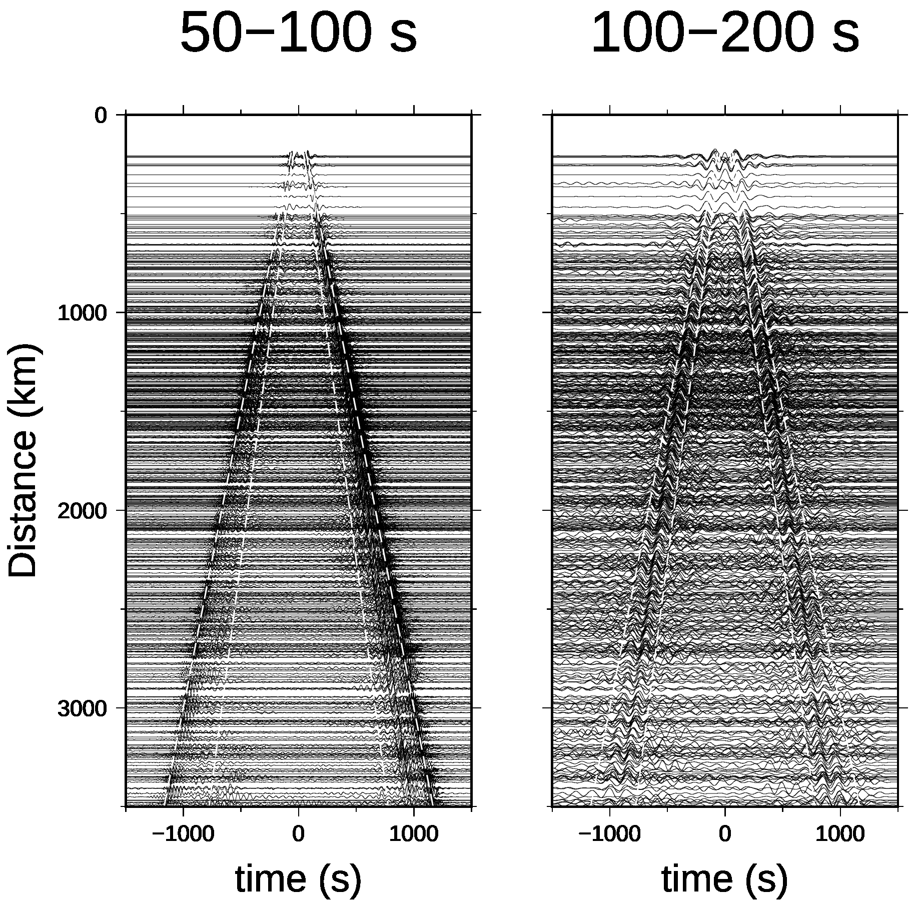

FIGURE 5.2: An example of the NCFs between station ADO/CI and other stations. The NCFs are bandpass filtered between 50-100 s (left) and 100-200 s (right), respectively. The surface wave is clearly seen in both the positive and negative component, and the velocity of the surface wave is within the range of 3.0 km/s-4.5 km/s.

to be longer than three wavelengths. However, because long-period surface wave from ambient noise are extracted and used in this study, if the interstation distance is limited to three wavelengths, long period measurements will be lost. However, the measurements from short interstation distance are vital to constrain small-scale heterogeneities. For example, surface waves at 100 s period typically have a wavelength of ∼400 km. Therefore, the three wavelength cut-off would discard all the dispersion curves with interstation distance less than 1200 km. Fortunately, a recent study by Luo *et al.* (2015) has demonstrated that the dispersion measurements from station pairs with interstation distances as short as one wavelength are accurate enough to be included in ANT. So in this study, the first selection criterion is to discard dispersion curves with interstation distance less than one wavelength.

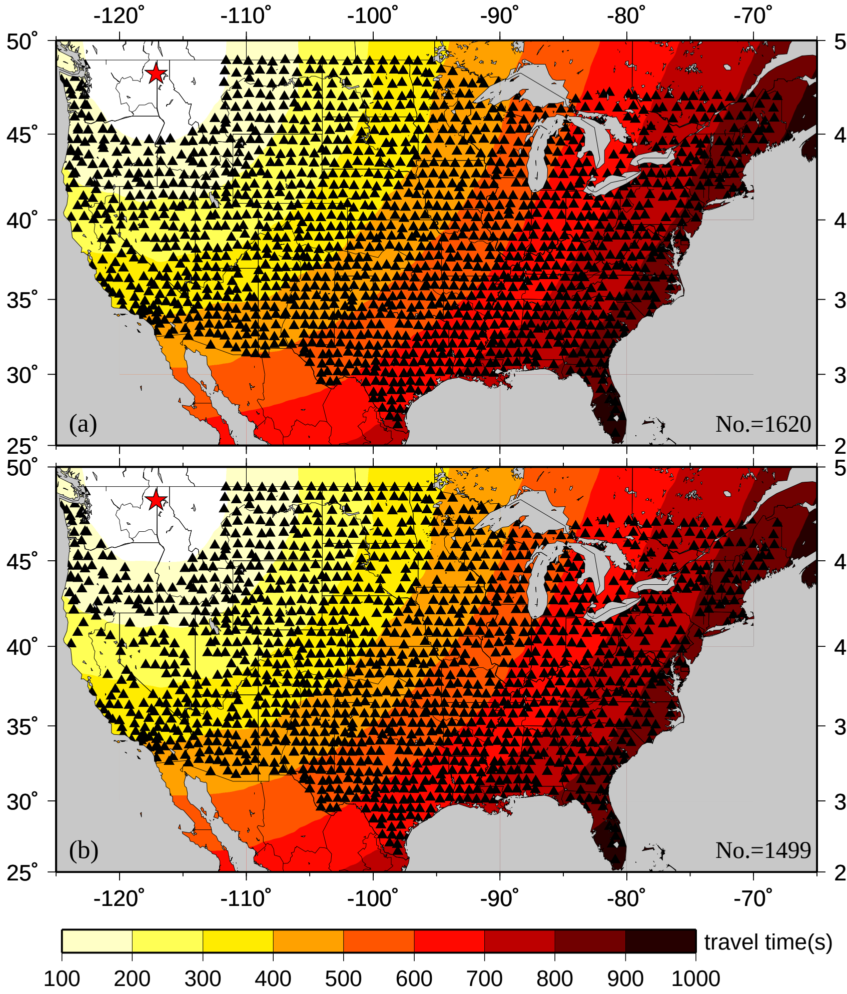
-120°
-110°
-100°
-90°
-80°
-70°
50°
45°
40°
35°
30°
25°
(a)
No.=1620
(b)
No.=1499
travel time(s)
100
200
300
400
500
600
700
800
900
1000

FIGURE 5.3: The phase travel time surface for the 50 s period surface wave centered at station NEW/US (blue star). (a) is the result before applying the SNR criteria; (b) is the result after performing 2π cycle skipping correction.

Second, the SNR (defined in Chapter 2) of the surface waves has to be larger than 10. Lastly, errors caused by cycle skipping are corrected using the curvature of the travel time surface (Figure 5.3), and dispersion curves with phase travel time anomaly larger than 6 s were discarded. Here, the travel time anomaly represents the difference between the measured and predicted travel time calculated from all the other stations. We plot the final numbers of Rayleigh wave phase velocity measurements that meet these criteria at each period in Figure 5.5. As can be seen, the number of reliable phase velocity measurements peaks at the 20 s period, and decreases with increasing period.

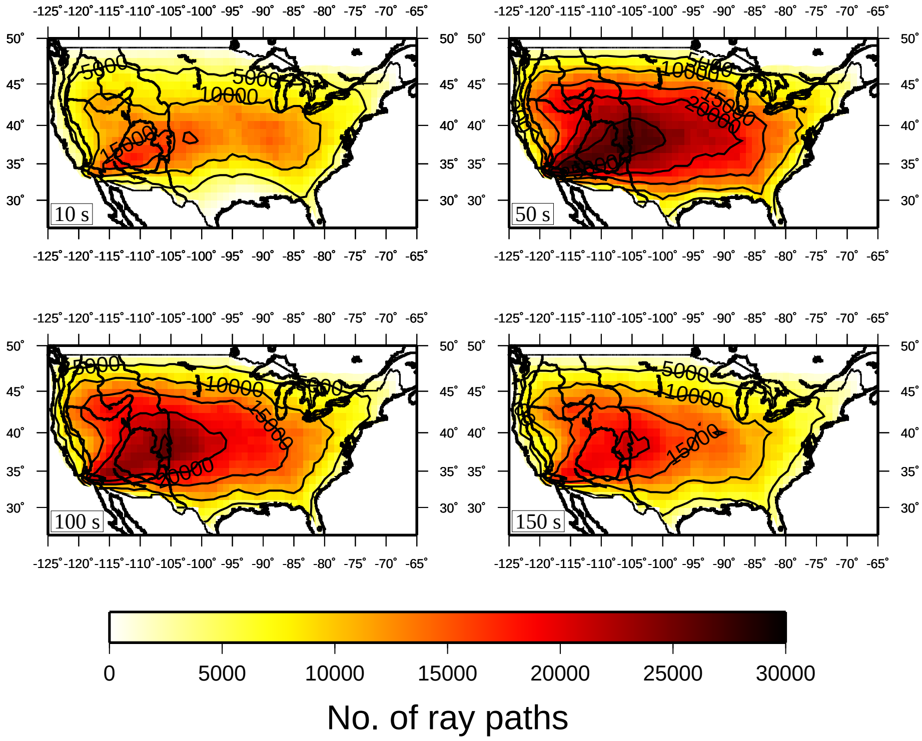
10 s
50 s
100 s
150 s
5000
10000
15000
20000
-125° -120° -115° -110° -105° -100° -95° -90° -85° -80° -75° -70° -65°
50° 45° 40° 35° 30°
0
5000
10000
15000
20000
25000
30000
No. of ray paths

FIGURE 5.4: The ray path coverage at periods of 10, 50, 100 and 150 s, with a grid size of 1° × 1°. The central and western US have denser ray coverage than that in the eastern part.

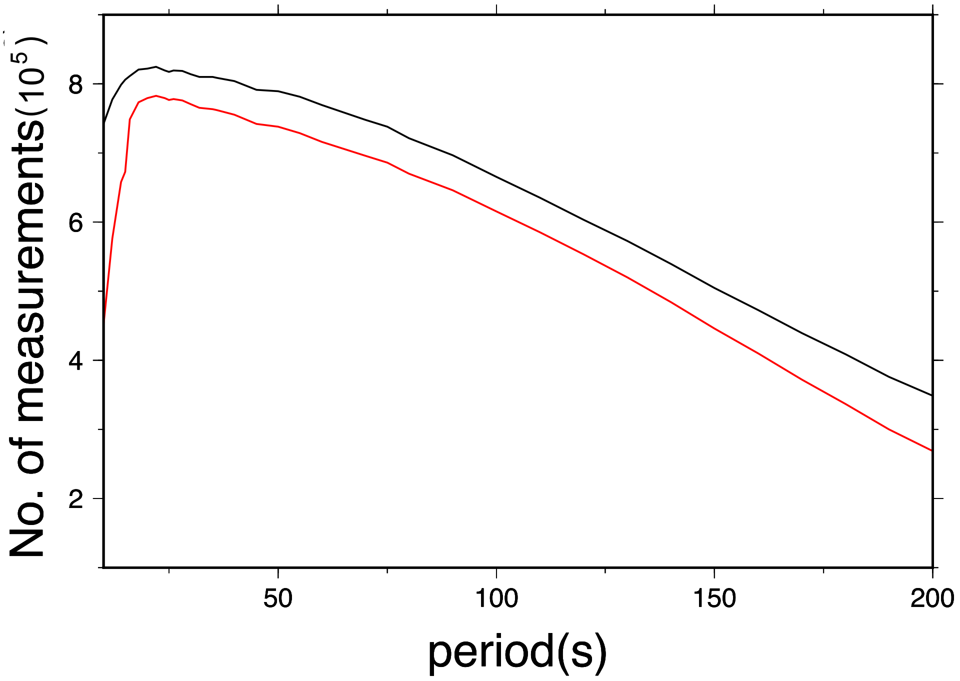

FIGURE 5.5: Numbers of phase velocity measurements for each period. The black line is the number after the selection based on the SNR and inter-station distance, and the red line is the number of measurements after performing cycle skipping corrections.

5.4 Method of tomography

Broadband surface waves from ambient noise can be inverted for structures at depths from the surface down to the lithosphere and asthenosphere. The question is how to construct broadband dispersion maps using these broadband surface waves. Most ANT studies performed to date use methods based on ray theory (e.g., Ekström, 2014; Lin *et al.* , 2008; Luo *et al.* , 2012; Yang *et al.* , 2007), which assumes that surface waves from ambient noise propagate along a great-circle path linking a pair of stations and ignores the finite-frequency effects. At periods shorter than ∼50 s, which is the main period band for most ANT, there is no significant difference between dispersion maps based on ray theory or finite-frequency theory (Shen *et al.* , 2013). Therefore, ray theory works well for constructing short period (<50 s) dispersion maps. However, to include surface waves at periods longer than 50 s in tomography, the finite-frequency effects must be considered. For long period surface waves (>50 s), the structures away from the geometrical ray may affect the travel time especially for long inter-station distance and the finite frequency effect cannot be ignored. In this case, the ray theory is not able to recover small-scale structures with a lateral length smaller than one wavelength or the width of the Fresnel zone.

In this work, we calculate 2-D phase sensitivity kernel based on the Born approximation for interstation surface wave between each station pair. A standard linearized inversion technique (Tarantola & Valette, 1982) is used to perform tomography to obtain phase velocity maps at individual period. Zhou *et al.* (2004) showed that the 2D phase sensitivity kernel to a local phase velocity perturbation could be defined as follows:

$$d = \iint_{\oplus} K(r,\omega)(\frac{c-c_0}{c_0})dx^2, \tag{5.1}$$

where the integration is over the study region, c_0 is the average phase velocity, c is the phase velocity at a geographic point, $K(r,\omega)$ is the phase sensitivity kernel, and d is phase delay. To obtain an Empirical Green's Function (EGF) for a pair of station, one station is regarded as the receiver and the other as the "virtual" point source. In contrast to the traditional sensitivity kernel for an earthquake source, the "virtual" source is assumed to be a vertical point source. According to Nishida (2011), by using a far-field approximation of a Green's function and presuming the earth model is spherically symmetric, and the distribution of

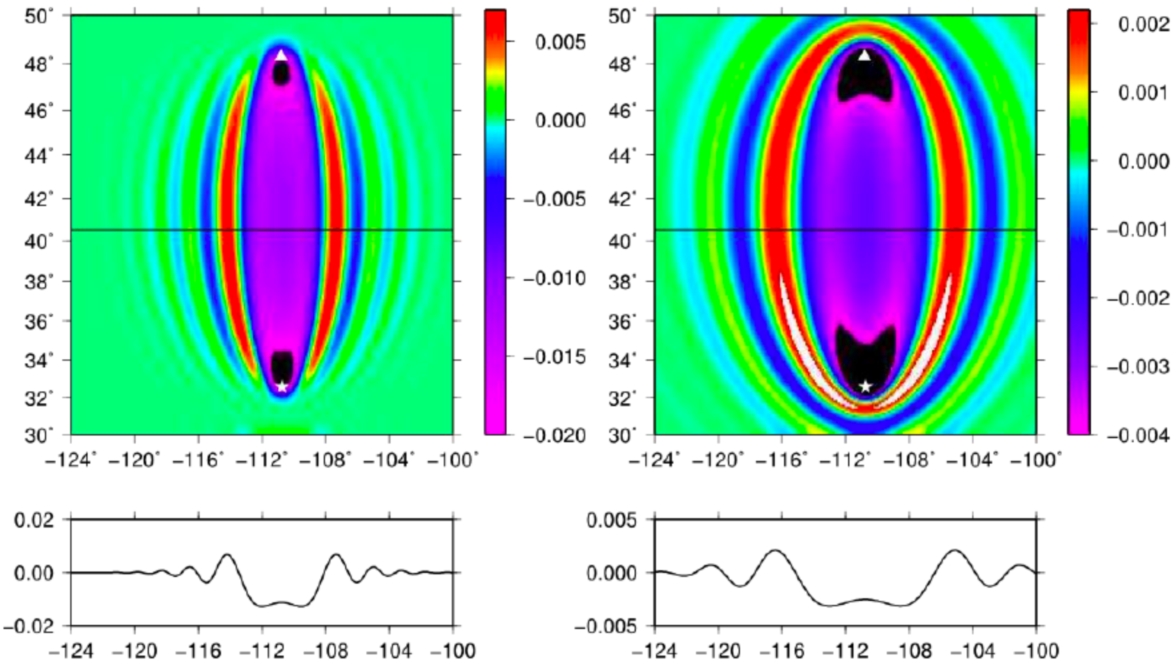

Figure 5.6: The 40 s (top left) and 100 s (top right) Rayleigh wave phase velocity sensitivity kernels in 2D. TA.117A is the virtual source (white star) and TA.B17A is the receiver (white triangle). The reference velocities are 3.87 km/s and 4.08 km/s at 40 s and 100 s periods, respectively. The sensitivities along profiles delineated by the bold lines in the top panels are shown in the bottom panels.

ambient noise sources is homogeneous, the 2D phase sensitivity kernel for phases extracted from ambient noise can be simplified as follows:

$$K^c(r,\omega) = Im(\frac{2k^2 R'' e^{(-i(k(\Delta'+\Delta''-\Delta)+\pi/4))}}{R\sqrt{8\pi k(|sin\Delta'||sin\Delta''|/|sin\Delta|)}}) \cdot exp(\frac{-\omega r(\Delta'+\Delta''-\Delta)}{2QC}), \tag{5.2}$$

where k is the wavenumber of the surface wave, Δ' is the distance from the "virtual" source to a scatter of phase velocity heterogeneities, Δ'' is the distance from the scatter to the receiver, Δ is the distance from the "virtual" source to the receiver, R and R'' are the receiver polarization vectors for the direct wave and scattered wave respectively. For the vertical components of Rayleigh wave, R'' and R are equal (Yang & Forsyth, 2006). r is the radius of the earth, Q the quality factor and C the group velocity.

For measuring phase delays of Rayleigh waves from NCFs, a series of narrow band-pass filters centered at individual frequencies are used. To take into account the effects of the finite bandwidth of narrow band-pass filters on measuring phase, sensitivity kernels for individual frequencies within each narrow band filter are averaged to represent the overall 2-D sensitivity kernel for the central frequency of each narrow band filter. The calculation of the effective sensitivity kernel is similar to that of Yang & Forsyth (2006) for earthquake surface waves. Figure 5.6 shows the 40 s and 100 s Rayleigh wave phase sensitivity kernels between stations TA.117A and TA.B17A. These kernels are smoothed using a 2-D Gaussian function with a characteristic length of 65 km.

A standard, iterative and linearized inversion technique (Tarantola & Valette, 1982) is used to invert the phase delays for phase velocity perturbations. The solution for the general non-linear least-squares problem is given as:

$$\Delta m = (G^T C_{nn}^{-1} G + C_{mm}^{-1})^{-1} (G^T C_{nn}^{-1} \Delta d - C_{mm}^{-1} [m - m_0]), \tag{5.3}$$

where m_0 is the starting phase velocity model, m is the current phase velocity model, Δm is the change of phase velocity relative to the current model, Δd is the difference between the observed and predicted phase delays for the current model, G is the partial derivative of the phase delay with respect to the perturbation of phase velocity i.e. the phase sensitivity kernel (Equation 5.2), and C_{nn} and C_{mm} are the phase data covariance matrix and prior model covariance matrix, respectively.

The inversion is carried out in three steps. First, we obtain the average phase velocity of the whole study region by assuming the phase velocity of the whole study area is homogeneous. The average phase velocity is then taken as the reference velocity for calculating the 2-D sensitivity kernel and as the initial model for the inversion in the second step. Secondly, phase velocity coefficients were inverted at all grid nodes by representing phase velocities at geographic points as 2-D Gaussian functions of the phase velocity coefficients. The characteristic length of the 2-D Gaussian function here is the same as the one used to smooth the sensitivity kernels, which is equivalent to inverting for a smoothed phase velocity map with a characteristic length of 65 km. In this step, data with phase travel time misfits larger than 2 s was discarded. Then we do the inversion again using the updated data to get the final phase velocity coefficients at all grid nodes. Third, phase velocity at any geographic point was obtained by averaging the phase velocity coefficients at surrounding grid nodes. The weights for the averaging are defined by the 2-D Gaussian function centered at that geographic point. The details of the parametrization and regularization in the tomography are similar to those described by Yang & Forsyth (2006).

5.5 Phase velocity maps

Examples of the phase velocity maps are presented in Figure 5.7, Figure 5.8, and Figure 5.9 respectively. At longer periods, more irregularities appear at the edges of the research area due to less dense ray path coverage at there edges. The other reason is that phase kernel for the station pairs near the edges extend outside the study region, thus the edges are not well constrained. Discussion of the tomographic maps is guided by the surface wave sensitivity kernels of shear wave velocity. Surface waves are most sensitive to the structure at depth of about 1/3 wavelength. For example, the 20 s surface wave samples the structure of the middle crust about 20-30 km, and 100 s surface waves is sensitive to depths of about 100-150 km.

The phase velocity maps show many velocity anomalies that correlate remarkably well with the geological features. For example, the phase velocities from 10 to 40 s (Figure 5.7) mainly represent middle and lower crust and uppermost mantle velocity structures. Slow anomalies are geographically correlated with the Yellowstone hotspot, the Snake River Plain, Mississippi Embayment, as well as the vicinity of the High Lava Plains. Meanwhile, low velocity anomalies are also observed at the edges of the Basin and Range province, notably along the western edge adjacent to the Sierra Nevada mountain range, and the eastern edge extending from the Wasatch Front through the transition to the western Colorado Plateau. The large scale high velocities (with anomaly of above 4%) in the east are correlated with the Big Plain Basin. At long periods (>50 s) (Figure 5.8, Figure 5.9), the velocity in the west is much slower compared to that in the east. This is probably because the western part is a tectonically active region, where the subduction of Farallon plate has shaped the geologic history for over the past 150 million years (Savage & Silver, 1993). The eastern part of America is a tectonically stable region, and shows faster velocities.

To illustrate that the finite-frequency broadband ANT method is effective in mapping phase velocities, we compare our phase velocity maps with other maps generated by using

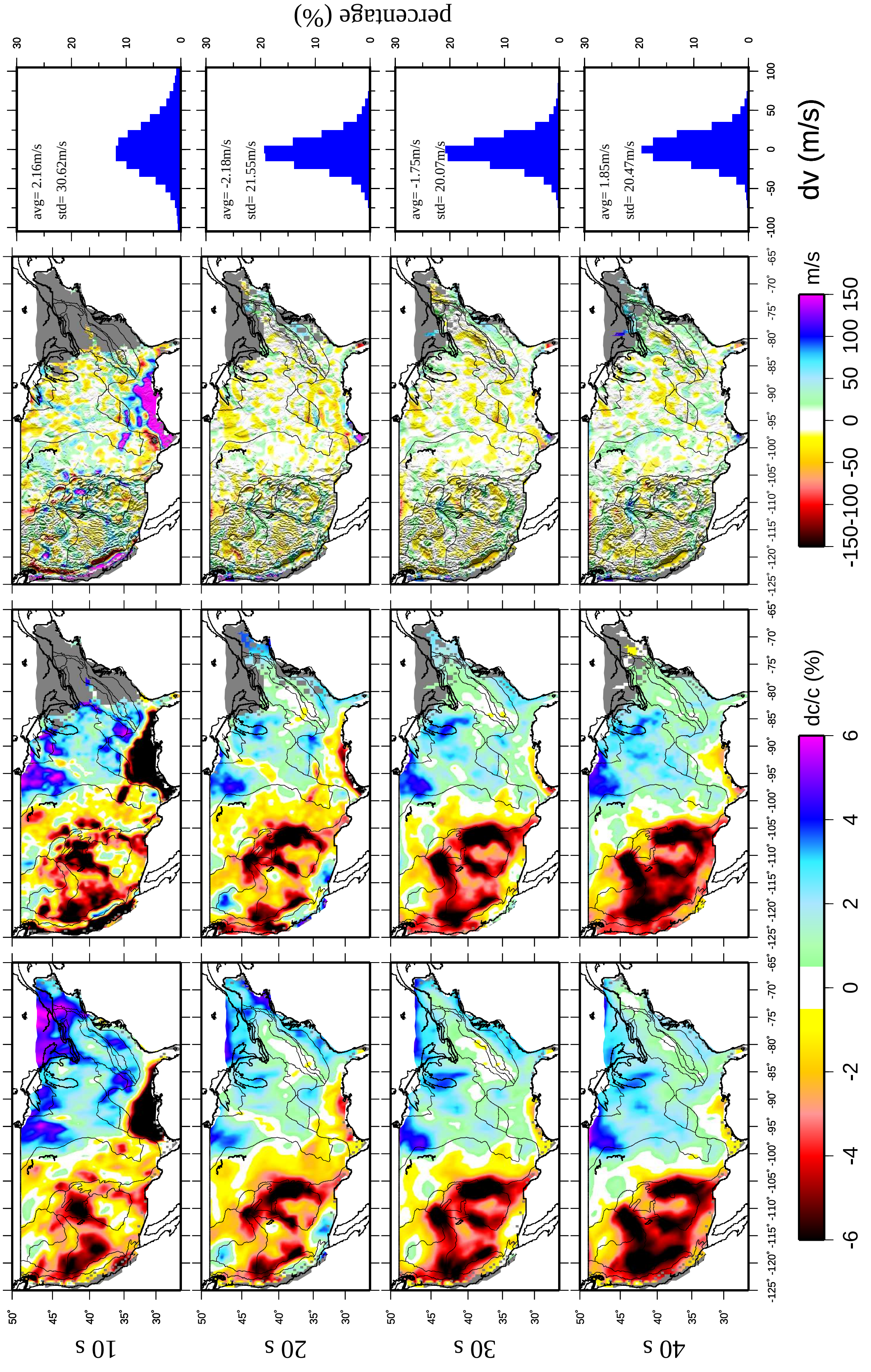
10 s
20 s
30 s
40 s
avg= 2.16m/s
std= 30.62m/s
avg= -2.18m/s
std= 21.55m/s
avg= -1.75m/s
std= 20.07m/s
avg= 1.85m/s
std= 20.47m/s
percentage (%)
dv (m/s)
m/s
dc/c (%)
-6 -4 -2 0 2 4 6
-150 -100 -50 0 50 100 150
-100 -50 0 50 100
0 10 20 30
50° 45° 40° 35° 30°
-125° -120° -115° -110° -105° -100° -95° -90° -85° -80° -75° -70° -65°

Figure 5.7: Phase velocity maps at periods from 10 to 40 s. The first column is our result based on ray theory tomography method; The second is from Ekström (2014), which is also constructed using ambient noise data; the third column is the difference between this two data sets; the fourth column is the statistical distribution of the difference with the mean and standard deviations showing on the top left corner.

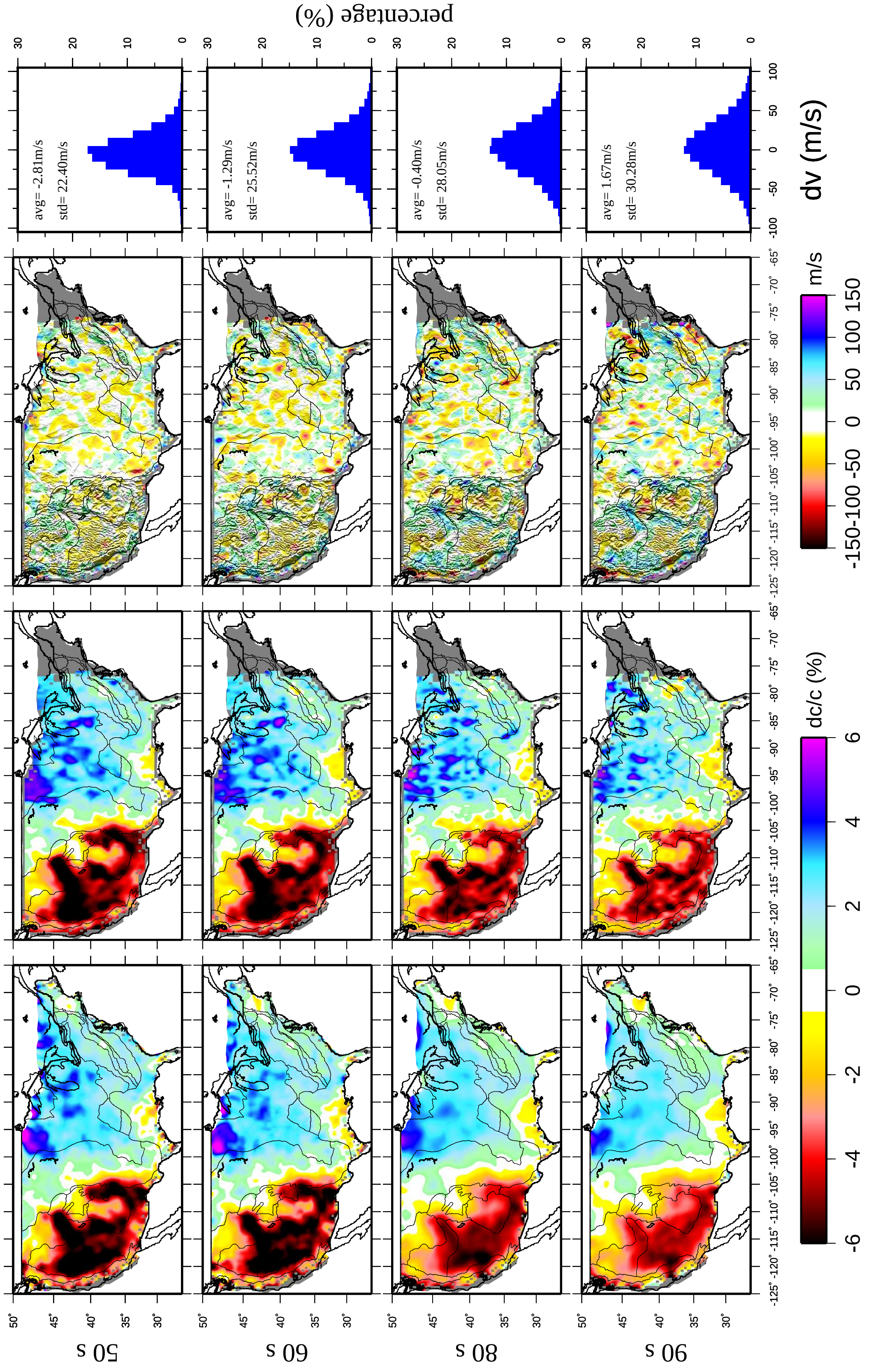
50 s
60 s
80 s
90 s
avg= -2.81m/s
std= 22.40m/s
avg= -1.29m/s
std= 25.52m/s
avg= -0.40m/s
std= 28.05m/s
avg= 1.67m/s
std= 30.28m/s
percentage (%)
dv (m/s)
dc/c (%)
m/s
-6 -4 -2 0 2 4 6
-150 -100 -50 0 50 100 150
-100 -50 0 50 100
0 10 20 30
-125° -120° -115° -110° -105° -100° -95° -90° -85° -80° -75° -70° -65°
30° 35° 40° 45° 50°

FIGURE 5.8: Phase velocity maps at periods from 50 to 90 s. The first column is our result based on finite frequency tomography method; the second is from Shen *et al.* (2013), and they have extend the result to the east of US (personal conmunication), which is Helmholtz tomography based on earthquake data; the third column is the difference between this two data sets; the fourth column is the statistical distribution of the differences with the mean and standard deviations showing on the top left corner.

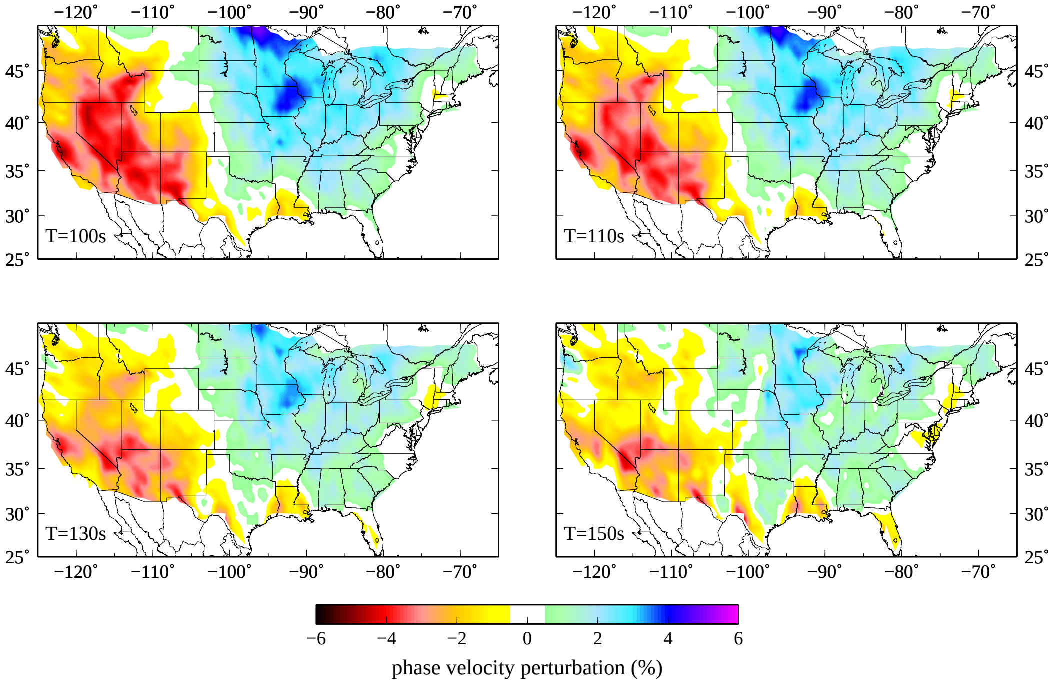

FIGURE 5.9: Phase velocity maps at periods from 100 to 150 s.

ambient noise data at short periods and earthquake data at intermediate/long periods. At the short periods of 10 s and 40 s, phase velocity maps from this study is compared with those from Ekström (2014) which are constructed using ANT method based on ray theory. At the intermediate/long periods from 50 s to 90 s, the phase velocity maps from this study are compared with those obtained from earthquake surface waves using Helmholtz tomography Shen *et al.* (2013). Helmholtz tomography constructs localized phase velocities by solving the Helmholtz equation at each geographic point via tracking the lateral variations of surface wave phase travel times and amplitudes from earthquakes. This method implicitly considers the finite-frequency effects in constructing the phase velocities (Lin & Ritzwoller, 2011).

At all periods, the differences of phase velocity are small in most of the study region where the path coverage is dense. To quantify the differences, histograms of differences are presented in the right-hand column of Figure 5.7 and Figure 5.8, and the mean and standard deviations are calculated. The differences in phase velocity nearly follow Gaussian distributions. The mean of differences are 2.18 m/s and 1.75 m/s, and the standard deviations are 21.55 m/s and 20.07 m/s at 20 and 30 s periods respectively. At the longer periods of 60 s

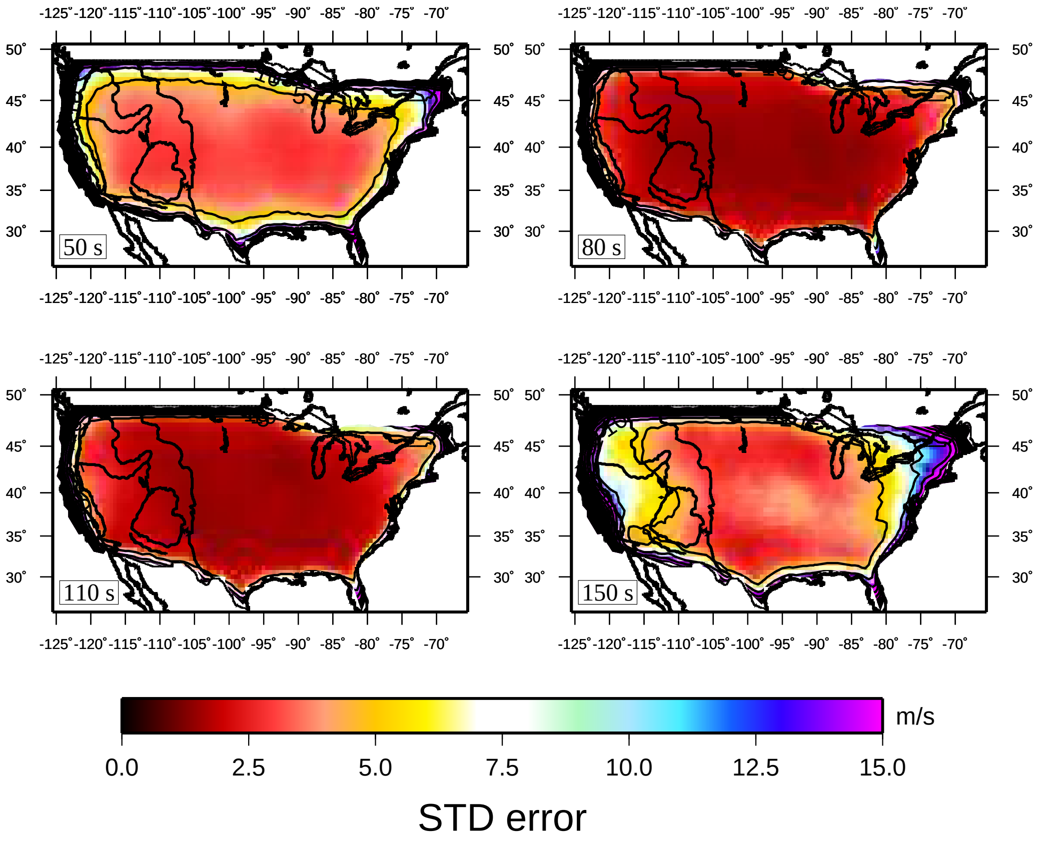

FIGURE 5.10: The standard error of the tomography at periods of 50, 80, 110 and 150 s respectively. The standard error at 150 s is larger than that of other periods which is probably due to much sparser ray coverage at this period.

and 70 s, the means of differences are ~2 m/s, and the standard deviations are ~25 m/s.

We estimate the resolution of the tomographic image with a checkerboard test. The checkerboard input model is discretized into a 0.5° × 0.5° grid. The size of alternatively high and low velocity cell is 2° × 2° and 1° × 1°, and the velocity perturbation is ±6% (Figure 5.11) with an average velocity of 3.5 km/s. The synthetic data of phase velocities are calculated according to the actual station pairs at 50 s and 100 s periods, respectively. During the inversion, the grid size is also set to be 0.5° × 0.5°. We can see that the anomalies can be well recovered in most part of the region, especially in the western and central part. From the resolution test, we can say that the resolving power is generally good in most of the part of US, and the lateral resolution is estimated to be at least 1°.

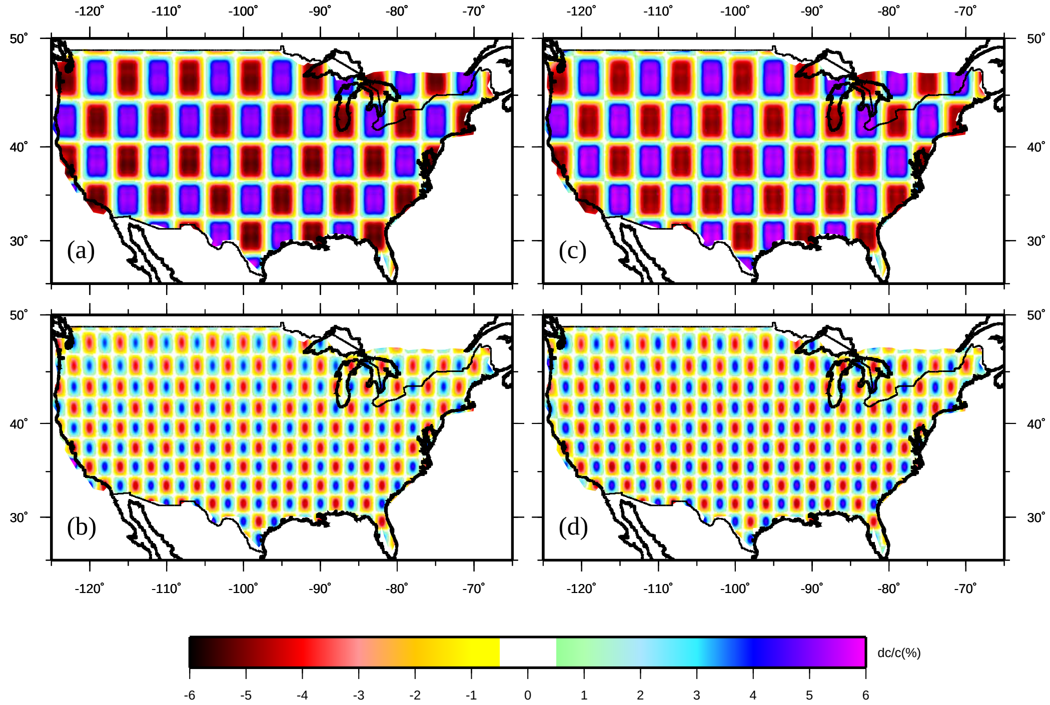

FIGURE 5.11: Recovered checkerboard models using finite frequency tomography. The left column is for 50 s period , and the right is for 100 s period. The size of the alternatively high and low velocity cells in the top and bottom figures is 2° × 2° and 1° × 1°, respectively.

5.6 3D shear model construction

The resulted phase velocity maps only reflect the integrated information of structure and do not infer the velocity structures at specific depths. In order to construct the 3D shear wave velocity, we invert local dispersion curves extracted from the resulting phase velocity maps for the 1D depth shear wave velocity profiles at all grid nodes. We then assemble all of the 1D depth profile to form the final 3D model.

5.6.1 Model Parameterization

At each grid point we obtain the local dispersion curve from 10 to 150 s with associated uncertainties from the phase velocity maps. The Rayleigh wave phase velocity at this period band of 10-150 s is sensitive to the V_{sv} at depths from the surface to depth of ~300 km (Figure 5.12).

For the gridpoint with a sediment layer thickness greater than 2 km (from crust1.0 (Laske

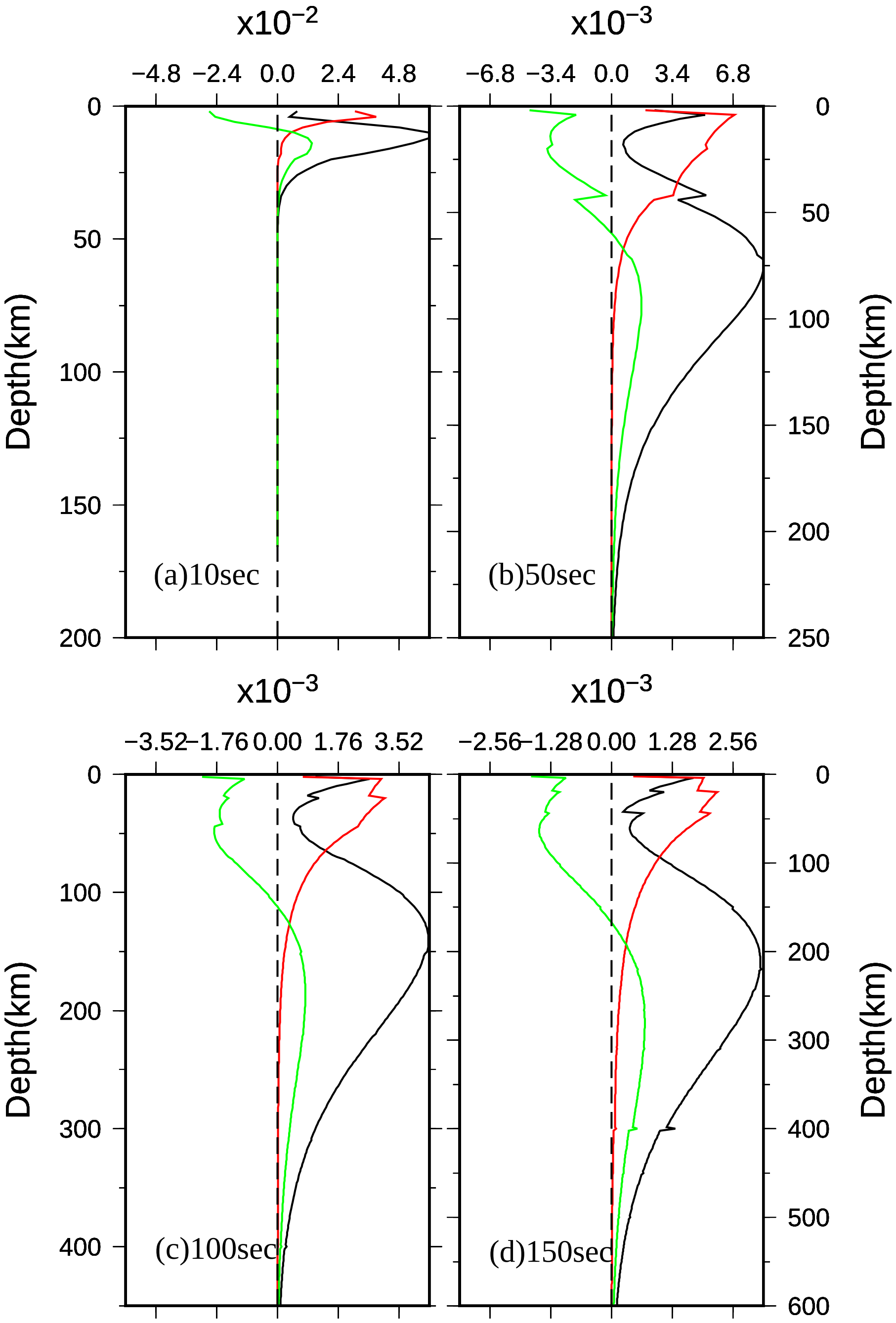

FIGURE 5.12: Phase velocity depth sensitivity kernels of V_{sv} (black curves), V_p (red curves) and ρ (green curves) at different periods of (a) 10 s, (b) 50 s, (c) 100 s, (d) 150 s.

et al. , 2013)), we use 3 parameters to model the sedimentary layer as Shen *et al.* (2012a), including the velocities at the top and the bottom of the sediment layer and the sedimentary layer thickness. If the sedimentary layer is thinner than 2 km, we do not parameter it but treat it as a part of top crust because our surface wave data cannot constrain such thin layer. The velocity in the sedimentary layer is constrained to monotonically increase.

Because the dispersion curves are sensitive to mean velocity model, we use four B-spline to parameterize the crystalline crust and five B-spline in the mantle according to Shen *et al.* (2013). The 1D sensitivity kernels (Figure 5.12) show that the phase velocity is primarily sensitive to V_{sv}, followed by compression wave velocity (V_p) and density (ρ). These three physical properties have different sensitivity depths; for example, at period of 50 s (Figure 5.12) the V_{sv} at depth of about 70 km contributes mostly to the phase velocity variation, while V_p and ρ reach to their maximum sensitivity at depth about 30 km; and in the crust they have similar amplitude. Using only dispersion curves to simultaneously invert for all the three parameters usually gives non-unique results, due to the strong trade-off between each two of the parameters. To avoid this, we scale V_p and ρ to V_s by using empirical relation, so that only V_s is allowed to vary and the scaling relation is from Shen *et al.* (2013). In the sedimentary layer, V_p/V_s is 2, and $\rho = 1.74V_s^{0.25}$ while in the crystalline crust and upper mantle, V_p/V_s is fixed to 1.75 and $\rho = 0.541 + 0.3601V_s$ in the crust and upper mantle. Here we use the model of Shen *et al.* (2013) in the western and central part of US and Crust1.0 (Laske *et al.* , 2013) in the eastern part of US as the reference Moho depth model. The inversion scheme searches the real Moho depth within ±5 km of the reference value.

5.6.2 Inversion scheme

At each grid point a total number of 10 or 13 parameters are inverted for depending on whether sedimentary layer is included or not. We use a non-linear MCMC method to invert the local dispersion curves for the parameters mentioned above. The non-linear inversion method searches for the acceptable model that fits the data. The forward modelling method (dispersion curve calculation) is based on normal modes with code Minos (Masters *et al.* , 2007) modified by Guo *et al.* (2015).

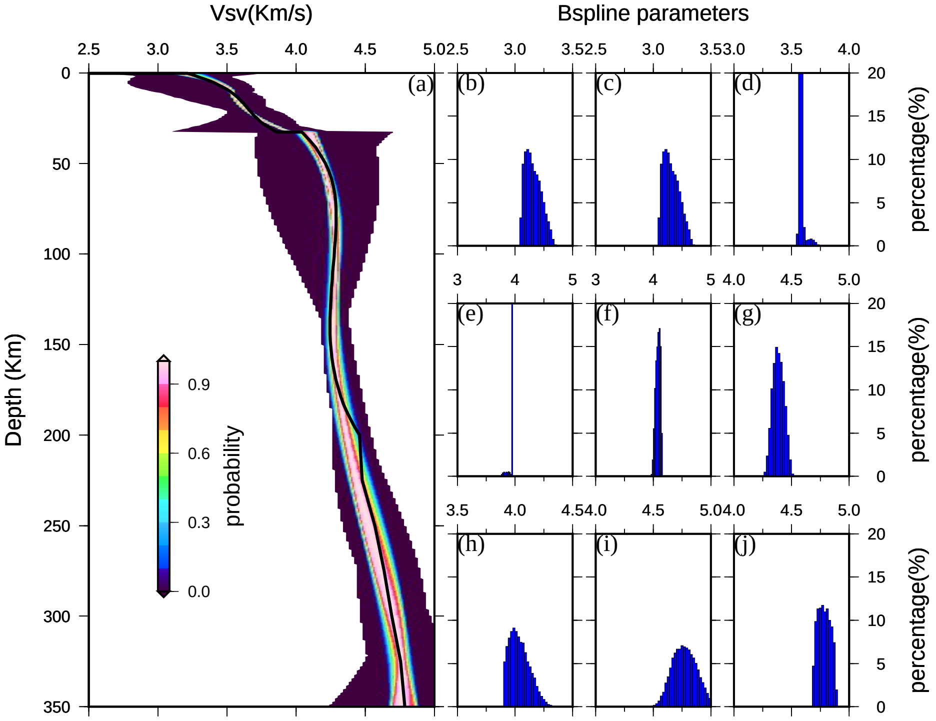

FIGURE 5.13: (a) The 1D velocity profile at (-120°, 30°) resulted from the probabilistic inversion method of MCMC. The reference model at this point below 200 km is from Schaeffer & Lebedev (2014). (b)-(j) are posteriori post distribution of the 9 B-spline parameters. We use the mean value of each parameter as the reference value.

The misfit function is defined as

$$Misfit = \frac{1}{N}\sum_{i=1}^{N}(V_{obs}(i) - V_{syn}(i))^2/\sigma^2(i), \tag{5.4}$$

where N is the number of the period, which is 18 in our case, V_{obs} is the measured phase velocity, V_{syn} is the synthetic phase velocity and σ is the standard error at each period provided by the tomography method. We use a delay rejection adaptive Metropolis algorithm (Haario *et al.* , 2006) to search for acceptable model in the model space and the method generates an ensemble of acceptable models to represent the posterior Probability Distribution Function (PDF) of the earth structure constrained by the observations. Many previous studies have applied this method to inverting for V_s structures (e.g., Afonso *et al.* , 2013b; Bodin *et al.* , 2012; Guo *et al.* , 2015, 2016). During the inversion, the best 3000 accepted models were used to calculate the mean and uncertainties for each depth.

Having prior information about the structures in the study area makes it possible to better constrain the model. Here, a prior model for the MCMC sampling is defined relative to a reference model subject to allowed perturbations and model constraints. This reference model (m0) includes the 9 B-spline parameters and 4 other parameters (thickness of sediment, up and bottom velocity of the sediment and Moho depth). The velocity of the model is constrain to monotonically increase in the sedimentary layers and crust. Additionally, the velocity is constrain to be smaller than 5.2 km/s throughout the model. We run the MCMC twice during the inversion. For the first time, we invert for the 9 B-spline parameters using MCMC method by fitting the reference model (Figure 5.13). In the crust and upper mantle, the model of Shen *et al.* (2013) is used as reference model in the Western and central part of US, and the model of Bensen *et al.* (2009) is used as reference model in the Eastern part of US. However, the depth of both models only extends down to 200 km, so the model SL2013NA (Schaeffer & Lebedev, 2014) is used as the reference model from 200 km to 350 km depth.

After the values of m0 (9 B-spline parameters) are determined, MCMC method is used again to perform a second inversion to search for the acceptable models. During the second inversion, the 9 parameters are allowed to vary within ±0.5 km/s around the determined value of m0 from the first step, and the Moho depth is allowed to vary within ±5 km around the reference value.

5.7 3D Vs model and discussion

We construct our 3D shear wave velocity model by assembling all of the 1D profile at each gridpoint, and we discuss the reliability of this model by comparing the large-scale features with those in other published models. The other models used for comparison are models from Bensen *et al.* (2009) (denoted as USB2009), US-CrustVs-2015 (from Schmandt *et al.* (2015), denoted as USS2015) and US-Crust-Upper-mantle-Vs.Porter.Liu.Holt.2015 (from Porter *et al.* (2016), denoted as USP2016).

USB2009 is also constructed using surface waves from ambient noise. The longest period of the surface waves they extracted is 70 s and a total of 203 stations were used (Bensen *et al.* , 2009). This restricted their model to a depth of 200 km. USS2015 is constructed from the joint inversion of Rayleigh wave dispersion curve and ellipticity measurements. USP2016 is an isotropic shear wave velocity model generated using ambient noise tomography and wave gradiometry of earthquake surface waves (Porter *et al.* , 2016).

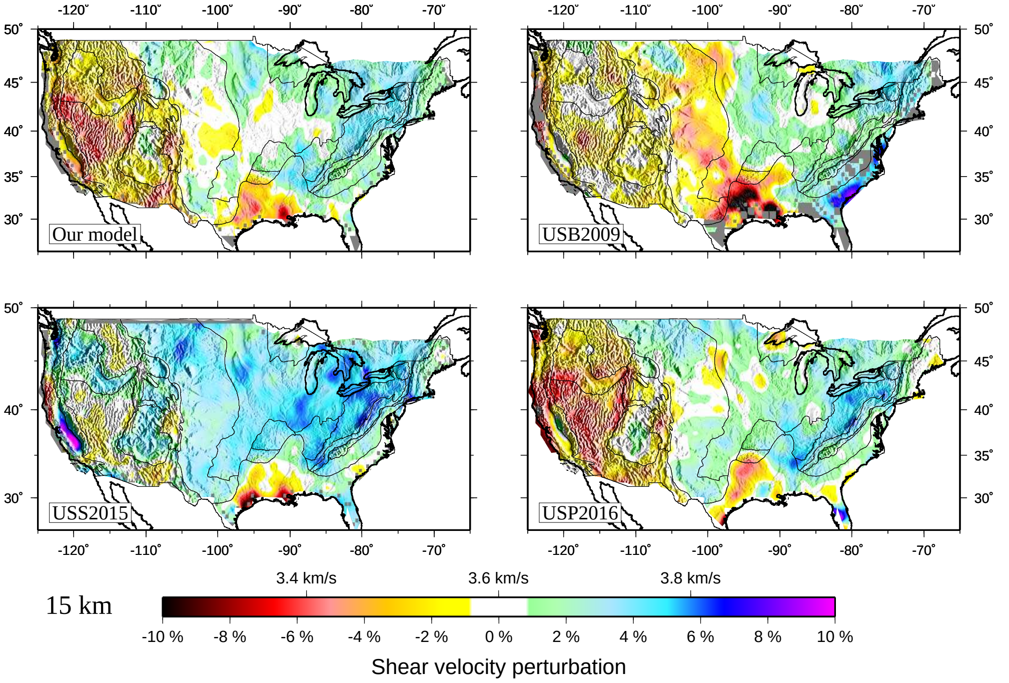

FIGURE 5.14: Comparison of our shear wave velocities at the depth of 15 km with the models of USB2009 (Bensen *et al.* , 2009), USS2015 (Schmandt *et al.* , 2015) and USP2016 (Porter *et al.* , 2016).

Depth slices of the shear wave velocity at 15 km (upper crust) are shown in Figure 5.14. There are many common features among these models such as the low velocity anomaly at the Mississippi Embayment and around Basin and Range in the west and northeast of Colombia Plateau. The high velocity anomaly regions coincides with Colorado Plateau and Appalachian Plateaus. The high velocity in the Appalachian Mountains is associated with the overthrusted Precambrian basement rocks (Liang & Langston, 2009). The shear wave velocity at this depth varies among different models. The mean velocity value for model USS2015 (Schmandt *et al.* , 2015) is higher than the others.

The depth slices of our 3D Vs model compared with the other three models at 80 km are shown in Figure 5.15. The main pattern of the model is consistent with others. For example, the sharp contrast of the tectonically active low-velocity western US and the high-velocity cratonic eastern US is clearly visible at this lithospheric depth. However, the model from this study reveals more detailed structures. For example, the low velocity anomaly beneath

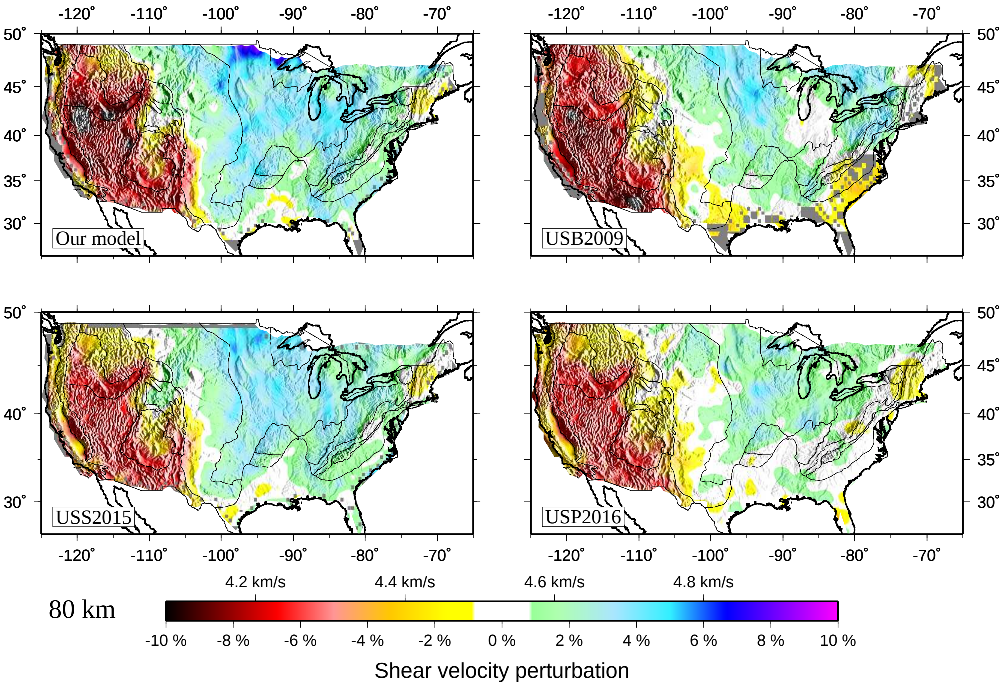

Figure 5.15: The distribution of shear wave velocities at the depth of 80 km (similar to Figure 5.14).

the Rocky Mountain, Northwest of Basin and Range and the Snake River Plain. Likewise, the main lithospheric core of the craton can be seen clearly, with high velocity anomaly of about 5% at this depth. This is consistent with the model SL2013NA (Schaeffer & Lebedev, 2014). However, in other models, the craton is not that obvious, especially at the depth of 150 km. In the mantle, the model from this study reveals a distinctive fast anomaly in the northern Colombia Plateau and a rounded spot in the southeastern part of Colombia Plateau.

From the depth slices shown in Figure 5.16, we can observe velocity changes along the depth. The high velocity anomalies corresponding to the stable cratonic regions are confined to the eastern part of Rocky Mountain from the uppermost mantle to a depth of about 250 km. And the low velocity anomaly beneath the Yellowstone Snake River Plain extends from the upper most mantle to the depth of about 150 km.

Figure 5.17 and Figure 5.18 show some transects of our 3D Vs model. The East-West velocity dichotomy is also clear in the vertical transects (Figure 5.17). This shear wave velocity dichotomy can be observed from the crust to a depth of 200-250 km. The imaged

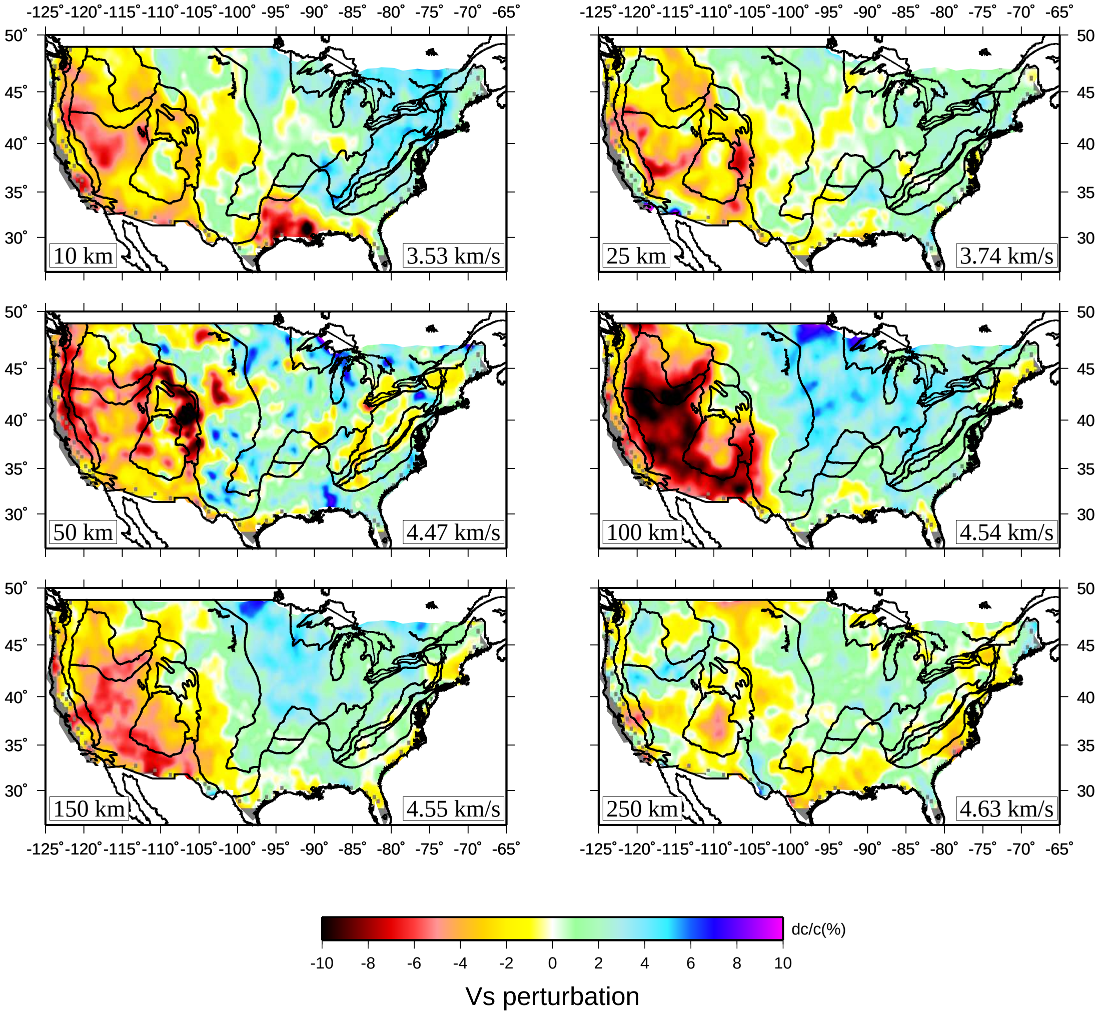
-125° -120° -115° -110° -105° -100° -95° -90° -85° -80° -75° -70° -65°
50°
45°
40°
35°
30°
10 km
3.53 km/s
25 km
3.74 km/s
50 km
4.47 km/s
100 km
4.54 km/s
150 km
4.55 km/s
250 km
4.63 km/s
dc/c(%)
-10 -8 -6 -4 -2 0 2 4 6 8 10
Vs perturbation

FIGURE 5.16: Shear wave velocity maps at depths of 10, 25, 50, 100, 150 and 250 km respectively. The color represents velocity perturbations respect to the mean of each depth, which is labeled in the bottom.

boundary of the East-West dichotomy is consistent with previous models. The low velocity anomaly in western US is about 10% lower than the average velocity. This indicates both thermal and composition differences between the cratonic region in the Eastern part and the western US. The parabolic shape of the slow velocity anomaly beneath Yellowstone (Figure 5.18) is consistent with the regional model DNA10-S (Obrebski *et al.* , 2011). It supports the interpretation of hot and buoyant whole mantle plume that feeds the volcanism in the Yellowstone-Snake River Plain region (Obrebski *et al.* , 2011).

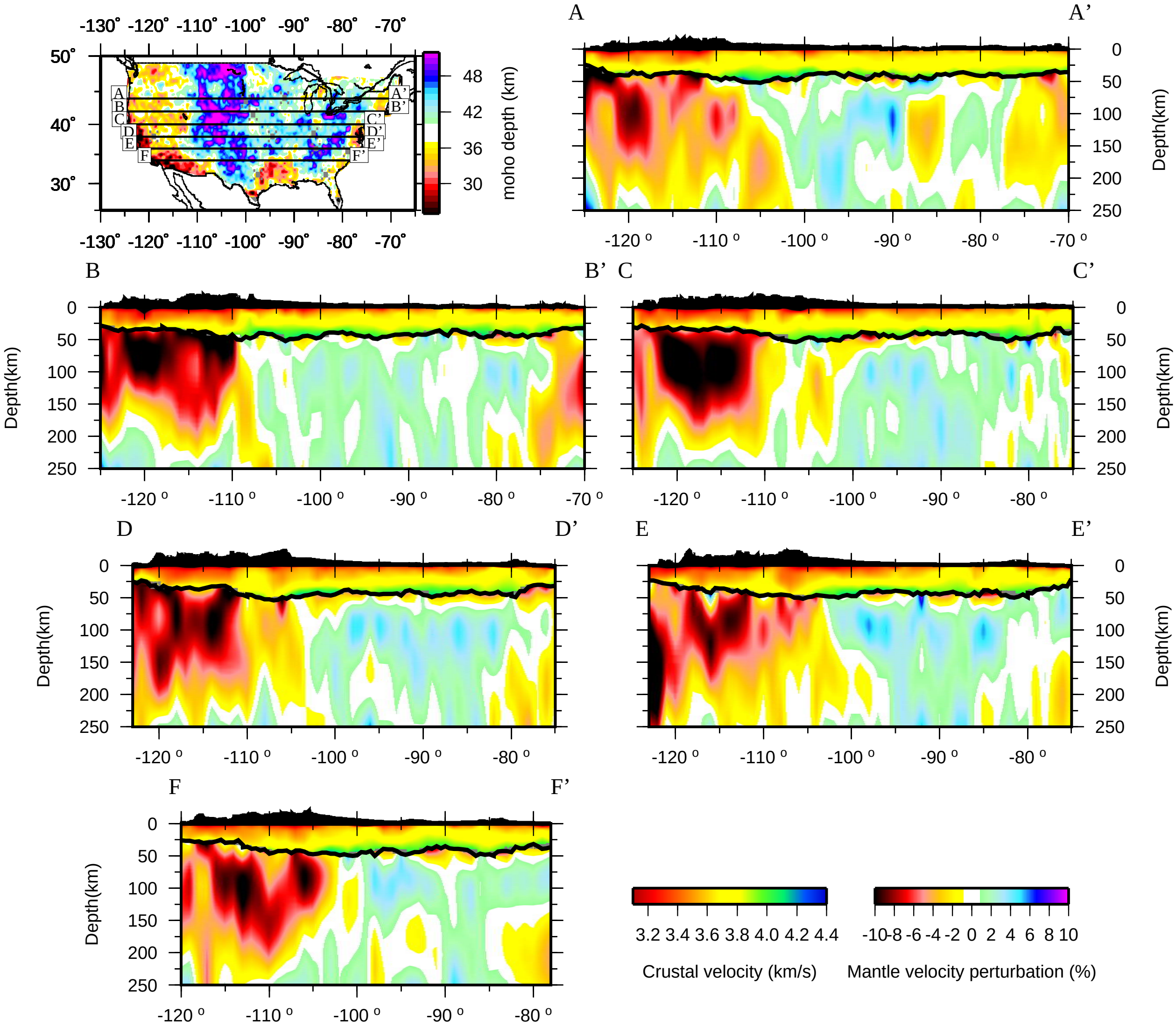

Figure 5.17: Vertical cross sections across the US continent along with the Moho depth distribution from our MCMC inversion.

5.8 Conclusion

In this chapter, we extract broadband (10 s to 150 s) surface waves from ambient seismic noise data recorded by 1895 stations across the contiguous United States. Rayleigh wave phase velocity tomography is then performed based on Born/Rytov approximation sensitivity kernel. The phase velocity maps are consistent with other published models. A new US 3D shear wave velocity model is constructed based on MCMC method. This study, for the first time, extracts long period (up to 150 s) phase velocity from ambient noise to perform

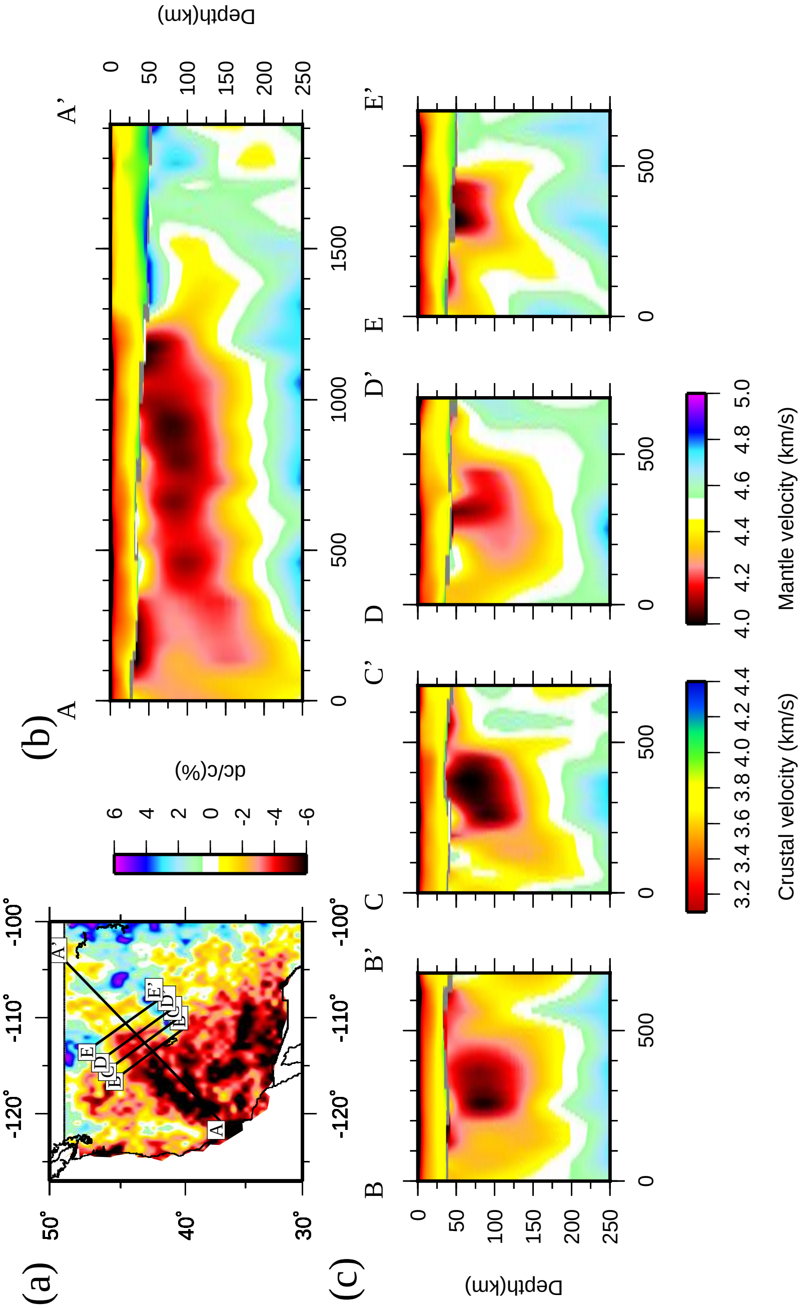

FIGURE 5.18: Vertical cross sections along and across the Yellowstone-Snake River Plain along with the Moho depth distribution from our MCMC inversion.

tomography on continental scale, and the successful application suggests that long period (above 50 s) surface wave from ambient noise can be used for tomography on continental scales. With broadband surface wave observations, we construct a new 3D V_{sv} model of the crust and upper mantle. The 3D structure is evaluated by comparison with other published models in the study area to demonstrate the reliability and accuracy of tomography using long period surface wave from ambient noise.

Local broadband dispersion curves from our broadband phase velocity maps can also be jointly inverted with other geophysical data, such as heat flow, geoid and gravity data, to constrain the thermal and compositional structure of the Earth's crust and upper mantle using Monte Carlo-based multi-observable probabilistic inversion methods (e.g., Afonso *et al.* , 2013a,b).

6

Accuracy of earthquake location based on group travel time of surface wave from ambient noise

6.1 Summery

In this chapter, we review earthquake location methods using ambient noise. Three methods proposed by different groups are discussed. The method based on group travel time (Xie *et al.* , 2011) is the most effective one, because this method works well even in seismic regions without dense coverage of seismic stations, while the other two methods only work in cases in which there is a dense seismic array in the source regions (Barmin *et al.* , 2011) or a well-resolved source mechanism (Zhan *et al.* , 2011). We use data from a small seismic array in Australia to investigate the location error of the travel time-based method. In doing so, each stations from the array is treated as a virtual source and the rest as reference stations successively. Our results show that the location error using this method is ∼2 km, and the location error is almost independent on the distance between the reference station and the source.

6.2 Introduction

Locating earthquakes is one of the first-order questions in seismology and seismic hazard studies. The improvement in the precision of locating natural and artificial events is beneficial to the study of the Earth's structure, and vice versa. To achieve this, significant efforts have been made by the seismology community to provide a standard database of reference events with accurate and well-defined locations. Among them, IASPEI has collected and validated many events provided by global institutions named as ground truth events with high accuracy (<10 km) (Bondár & McLaughlin, 2009). Ground Truth events (referred to as GT, hereafter) can be used as input data to benchmark geophysical inversions, such as Yang *et al.* (2004) and Murphy *et al.* (2005). Meanwhile, the calibrations obtained from GT events can also be used to improve event locations (Flanagan *et al.* , 2007). Most of the GT0/GT2 events (the number trailing GT means the location accuracy in kilometers) are nuclear and chemical explosions, which are limited in quantity (∼1000) (Bennett *et al.* , 2010). Traditional methods of obtaining natural GT events depend on dense seismic network that is situated close to the hypocenter. Bondár *et al.* (2008) proposed a hybrid multiple-event location method to determine GT events, and this method has been widely adopted. However, this method based on seismic travel times usually requires stations with close spacing in order to mitigate the errors caused by the Earth's 3D heterogeneity and/or cross-overs of Pn and Pg waves.

Recently, many research groups have successfully used the InSAR method to compute near source displacement fields of large and moderate earthquakes (Dawson *et al.* , 2008; Fialko *et al.* , 2005; Massonnet & Feigl, 1998; Zha *et al.* , 2009). This geodesy method provides important constraints on the focal mechanism as well as centroid locations. By using this method, Dawson *et al.* (2008) successfully identified a very shallow and moderate earthquake that occurred in western Australia. Meanwhile, the synergy of seismic and InSAR methods has also been used to detect GT events in Asia and Middle East (Saikia *et al.* , 2002). However, one disadvantage of this method is that it does not work well in areas with forest coverage, neither for events with small (MW<5.0) magnitude and deep focuses. In addition, the perturbations in the atmosphere and post-seismic deformation can also affect the precision of the InSAR method.

Beseides the travel time measurements from body wave phases, surface wave waveforms also contain information about source parameters. Tan *et al.* (2006) proposed a hybrid method of using P wave travel time and calibration from surface waves to obtain GT5 events. In addition to that, three research groups have developed three different methods to calibrate earthquake locations using ambient noise data. Method developed by Barmin *et al.* (2011) (Method 1) requires a dense seismic array for optimal performance, which is not usually available in most seismic regions of the Earth, while method of Zhan *et al.* (2011) (Method 2) can effectively overcome this problem. However, both of the two methods are based on waveform measurements, thereby suffering from the uncertainties of source location. Instead, Method 3, which is proposed by Xie *et al.* (2011), is based on travel time measurements. It can be used to determine shallow earthquake locations without a prior knowledge of the centroid moment tensor.

Barmin *et al.* (2011) demonstrated that their method can achieve a location accuracy of ∼1 km, while the location error with method 2 can be close to 1-3 km according to Zhan *et al.* (2011). However, the accuracy of method 3 remains unknown. In this chapter, the accuracy of earthquake location using method 3 is investigated. We then discuss the relationship between the distance of the reference station and the location error, which is of great importance to station deployment in locating earthquakes in future studies.

6.3 Calibration of earthquake based on ambient Noise Cross-correlation Function

In the traditional methods of locating earthquakes, the misfits between synthetic and observational waveforms/arrival times are minimized in order to locate earthquakes accurately. Therefore, the error of the earthquake locations can rise from the errors of structure model, thus the uncertainties of the source parameter (the moment tenser) and the original time of the earthquake. Among the model errors, the dominant effect comes from the strong velocity heterogeneities of the Earth's interior. This can be reduced by two approaches. The first one, developed by Richards *et al.* (2006), uses differential times between multiple events by cross-correlating Lg waves to improve the relative location; the other method uses either empirical calibration (Zhu *et al.* , 2006) or calibration derived from 3D models (Yang *et al.* , 2004) to obtain high-precision absolute location.

The idea behind earthquake calibration using NCFs is quite simple. The only condition required by this method is that there must be a seismometer located very close to the earthquake, which continuously records long-duration ambient noise data. This seismometer can be installed either before or after the occurrence of the earthquake. Compared with traditional earthquake location methods, the method based on NCFs does not suffer from the uncertainties of the Earth's model. In addition, because NCFs are dominated by surface waves, which usually have higher SNR than their body wave counterparts, NCFs are very useful for locating earthquakes with small magnitudes. In the following section, the three earthquake location methods based on NCF are reviewed.

If there is a local station located close to an earthquake, the ray path between the source and a remote station is close to the ray path between the local station and the remote station. Under this condition, the effect of the velocity models on the propagation of surface waves either from earthquakes or from ambient noise is almost identical, and such propagation effects can also be considered during the minimization of the misfit between the recorded (earthquake records and NCFs) and synthetic waveforms. For NCFs, the differences between the observed and synthetic waveforms reflect the difference in the 3D model which is employed for calibration. Apart from such structural effect, synthetic earthquake waveforms are also affected by other two terms including the earthquake location and focal mechanism. If a reliable focal mechanism can be obtained, the remaining difference between the observations and synthetics is due to the source location. And a grid search algorithm can be used to obtain an optimal location that generates the minimum misfit.

Barmin *et al.* (2011) is the first study that developed earthquake location method using NCFs. They constructed synthetic NCFs between hypothetical locations and remote stations based on the NCFs between many local stations and remote stations. Then, the differential time is obtained by cross-correlation, before the amplitude of the waveforms is normalized. This method can reach a high location accuracy (<1 km). However, it requires a dense temporal/permanent network in the source region, which is usually not available in most occasions.

$$\begin{aligned} dT_{eq} &= T_{eq} - T_{syn_{eq}} = dT_{loc_{err}} + dT_{fm_{err}} + dT_{3d}, \\ dT_{NCF} &= T_{NCF} - T_{syn_{NCF}} = dT_{3d}, \\ Misfit &= dT_{eq} - dT_{NCF}. \end{aligned} \tag{6.1}$$

Zhan *et al.* (2011) proposed another approach towards locating earthquakes using NCFs, which invokes the use of synthetic earthquakes and NCF waveforms in a double difference form. The theoretical basis of this method is summarized in Equation 6.1 , where the subscript "eq" denotes the earthquake terms while the NCF terms are marked by "NCF". The differential time "dT" is the time difference between these two sets of waveforms, calculated by the cross-correlation between the two waveforms. T_{eq} is the measured earthquake travel time; W$T_{syn_{eq}}$ is the synthetic earthquake travel time; $dT_{loc_{err}}$ is the error caused by uncertainty of location, $dT_{fm_{err}}$ is the error caused by unclear of the focal mechanism, dT_{3d} is the error caused by velocity model. T_{NCF} is the travel time of NCF and $T_{syn_{NCF}}$ is the travel time of synthetic NCF. When we substract the waveform or arrival time difference between the synthetic Green's function and the real EGF, the error introduced by the structure model is eliminated. One advantage of this method is that it only requires the presence of a temporal station near the source. Zhan *et al.* (2011) used this method to successfully locate the Chino Hills earthquake in south California, with an error of about 1-3 km when well-established focal mechanism is used. However, when the uncertainty of the focal mechanism is large, this method tends to generate locations with large errors (Xie *et al.* , 2011).

$$Misfit = \frac{1}{N}\sum_{station}\sum_{period}|T_{station}^{period} - \frac{D(X_{source}, R_{station})}{U_{station}^{period}}|. \qquad (6.2)$$

In the other hand, the group arrival time of short period surface wave is almost independent of the focal mechanism (Levshin *et al.* , 1999). Therefore, by using the group arrival time, the effect of focal mechanism on the location error can be elliminated. Xie *et al.* (2011) defined a new NCF calibration based on the group velocity of inter-station Rayleigh wave in NCF. This velocity is equal to the average velocity of the path linking the reference station and remote stations, which is almost the same as that of the path linking the source and the stations. Although the principle of this calibration is quite similar to the waveform-based one, the adoption of group arrival time ensures that the effects from the uncertainty of the focal mechanism have been eliminated during the inversion. The new misfit function is defined as Equation 6.2, where the group travel time (T) equals to the distance divided by the group velocity. X and R are the location of the grid search source and the receivers.

6.4 Accuracy of earthquake location using travel time-based method and its relationship with the distance of the reference station

The traveltime-based method (method 3) is independent of focal mechanism, and it also takes the origin time into account during the inversion. However, the accuracy of this method is uncertain. In the meantime, how the location error is related to the distance between the reference station and the earthquake is also unknown. Therefore, it is necessary to investigate the accuracy of earthquake location using traveltime-based method and its relationship with the distance of the reference station in order to guide station deployment in future studies.

To test how the distance between the reference station and the earthquake affects the

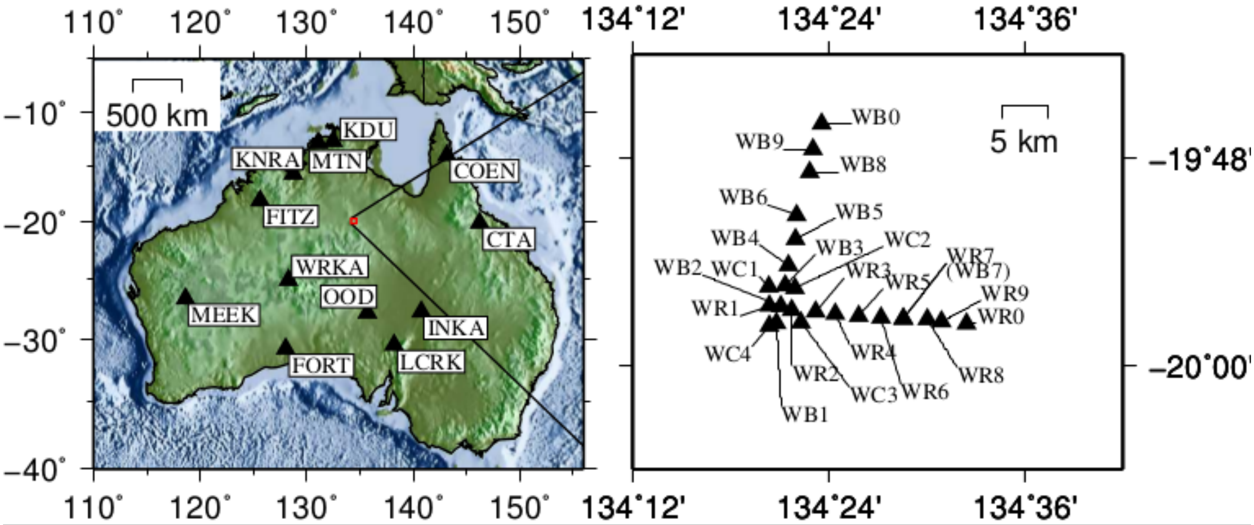
110°
120°
130°
140°
150°
−10°
−20°
−30°
−40°
500 km
KDU
KNRA
MTN
COEN
FITZ
CTA
WRKA
OOD
MEEK
INKA
FORT
LCRK
134°12'
134°24'
134°36'
−19°48'
−20°00'
5 km
WB0
WB9
WB8
WB6
WB5
WB4
WB3
WC2
WB2
WC1
WR3
WR5
WR7
(WB7)
WR9
WR0
WR1
WC4
WR4
WR2
WC3
WR6
WR8
WB1

Figure 6.1: The distribution of the small seismic array in Australia used in this study. This so-called Warramunga array has 24 stations, which are located to the centre of the continent. The 12 remote stations used here have a distance of about 800 km away from the array.

accuracy of the location, a seismic array is needed to perform a statistical analysis. To achieve this, we use a small seismic array in Australia (Figure 6.1). This array consists of 24 stations with small station spacing (right in Figure 6.1). Each of stations in this array can be treated as a "virtual" earthquake source and the others as reference stations. With a good distribution of remote stations, we can locate these "virtual" sources.

We collect vertical-component of ambient seismic noise data recorded in 2013-2014 by these 36 stations (Figure 6.1) from IRIS/DMC. NCFs are calculated between these 24 stations with 12 remote stations following the standard ambient noise processing procedures described in Chapter 2. First, the continuous seismic records are cut into two-hour long segments and the sampling rate is decimated to 1 Hz. Then, the trend, mean and instrumental response are removed. After that, the two-hour segments are cross-correlated and linearly stacked to form the final NCFs (Figure 6.2). The group velocities in the period band of 5-25 s are then extracted using FTAN (Bensen *et al.* , 2007) from the symmetric components of NCFs (an example is shown in Figure 6.3).

Each of the stations in the sub-array can be treated as the reference station to locate the other stations using a grid search method (Xie *et al.* , 2011). An example of the result taking

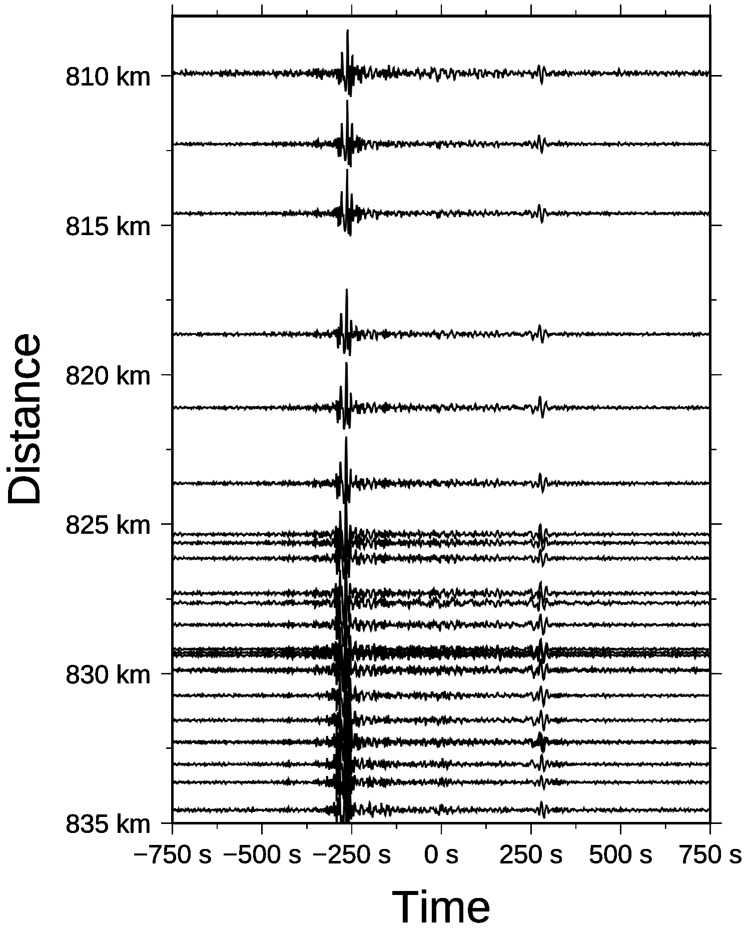

Figure 6.2: NCFs between COEN and the stations of the array. The waveforms are band-pass filtered in the period bands of 10-30 s. The negative time lag of the NCF represents the signal traveling from COEN to the array. Since the COEN is close to the coastline, the main energy is from COEN to the array. Thus the amplitude in the negative lag is stronger than that of the positive lag.

WB0 as a reference station to locate station WB1 is shown in Figure 6.4. The blue star is the estimated location of WB1, and the black star is the true location. Here REF=15.87 km refers to the distance between WB0 and WB1, while ERR=0.72 km represents the location error.

The reference distance (REF) versus location error (ERR) is shown in Figure 6.5. Excluding stations WB7, WB2 and WR8, the location errors of other stations are all below 4 km, and the errors are almost irrelevant to the reference distance. It is possible that stations WB7, WB2 and WB8 are problematic as seen from their dispersion curves (e.g.,6.3). We calculate the mean (1.42 km) and standard deviation of the errors (0.81 km). The small

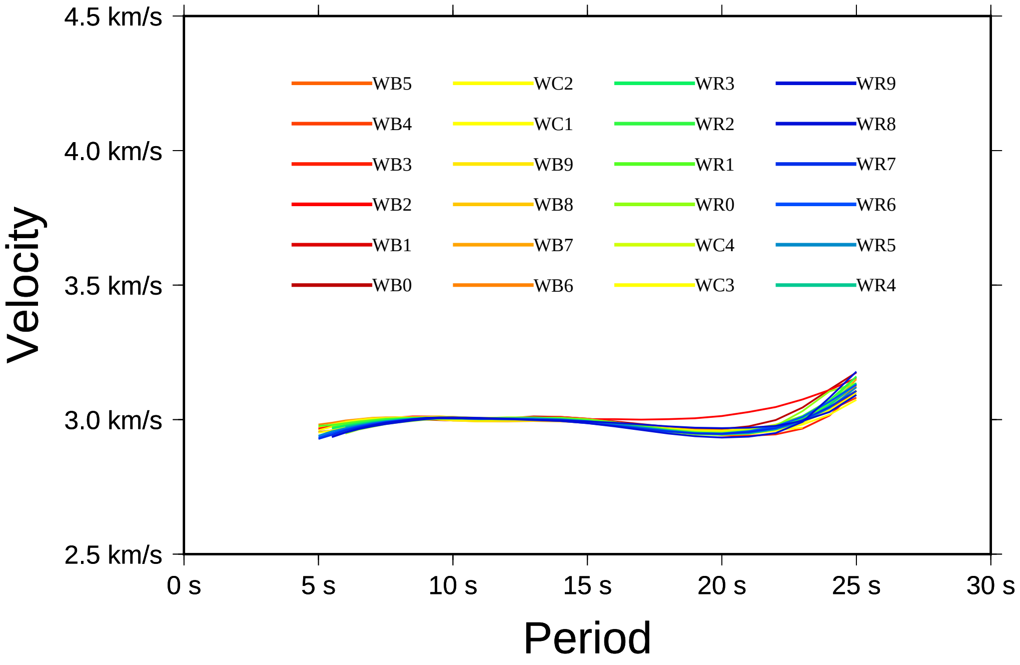

Figure 6.3: Group velocity dispersion curves computed from all symmetrical components of the NCFs in Figure 6.2 using FTAN (Bensen *et al.* , 2007).

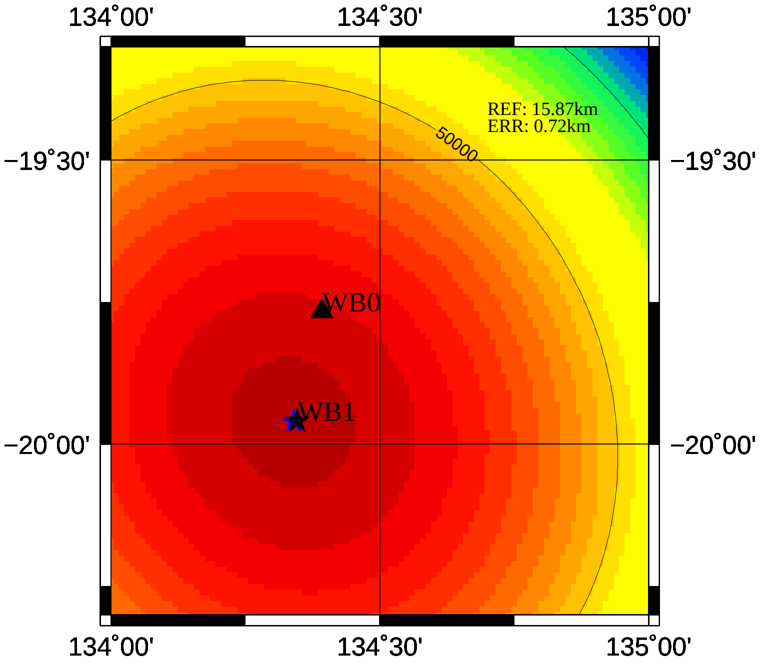

134˚00'
134˚30'
135˚00'
−19˚30'
−20˚00'
REF: 15.87km
ERR: 0.72km
50000
WB0
WB1

Figure 6.4: Location of WB1 (blue star) when taking WB0 (black triangular) as the reference station and using all of the 12 remote stations. Black star is the real location of WB1. REF is the distance between WB0 and WB1, and ERR is the location error, which is ~0.42 km.

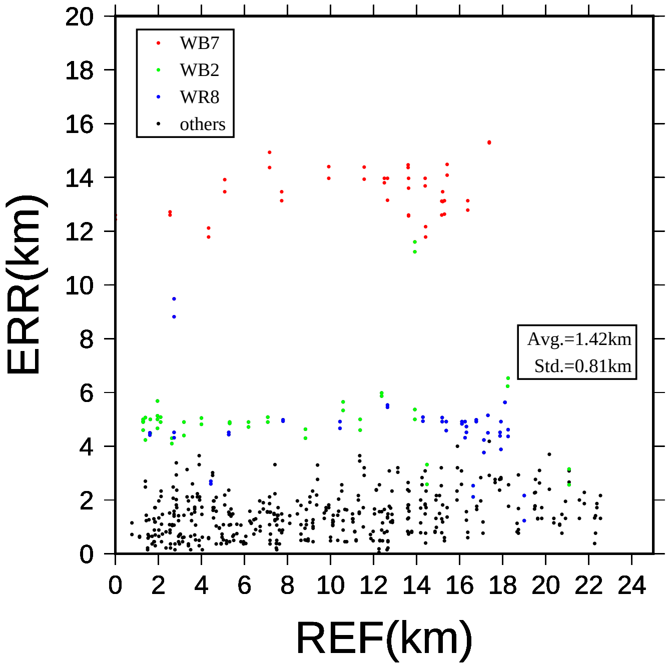

Figure 6.5: The relation between the distance of the reference station and the location error. The horizontal axis is the distance between the reference station and the target station, and vertical axis is the location error. All of the remote stations are used (Figure 5.2) for the locating. The mean of the location error is 1.42 km and the standard error is 0.81 km. When calculating the mean and standard deviation, the station WB7, WB2 and WR8 are included, meaning that the real mean and standard error should be smaller.

values of the mean and standard deviation indicates that the location error of this method is less than 2 km under the condition that the reference station is less than 20 km and the remote stations are well distributed.

Then, we do another test using only four well-distributed stations (Figure 6.6), the location error is larger (Figure 6.6) compared to that achieved with many well-distributed stations, and the location error increases with the reference distance. It appears that the relationship between the error and the reference station distance is not that obvious. However, the trend shows that with reference station become further, the location error is slightly bigger and has larger standard error, especially when the station is sparsely distributed.

However, when the reference station is less than 15 km to the virtual source, the location error is always below 4 km. We also test that, when using only three well-distributed stations (Figure 6.7). The location error is much larger compared to those with many well-distributed stations, and the location error increases with the reference distance. But when the reference

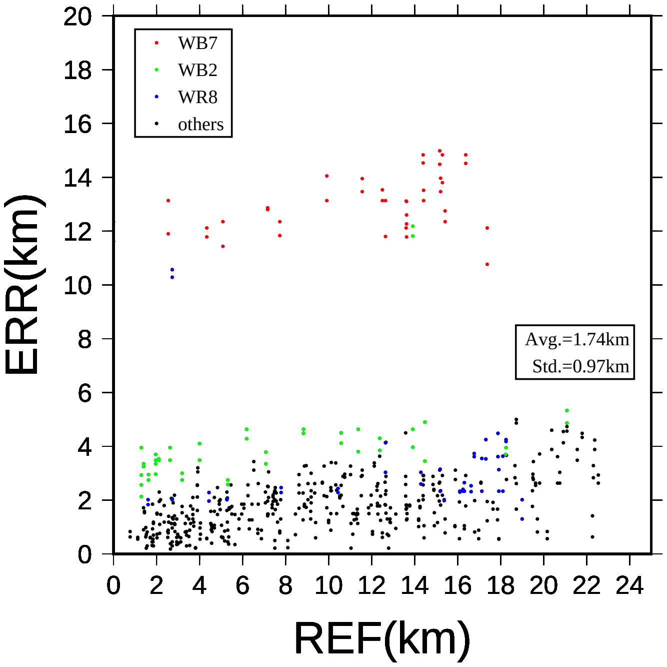

Figure 6.6: The same as Figure 6.5, but with only four remote stations: KNRA, COEN, WRKA and INKA. The four remote stations are evenly distributed in four directions of the small array.

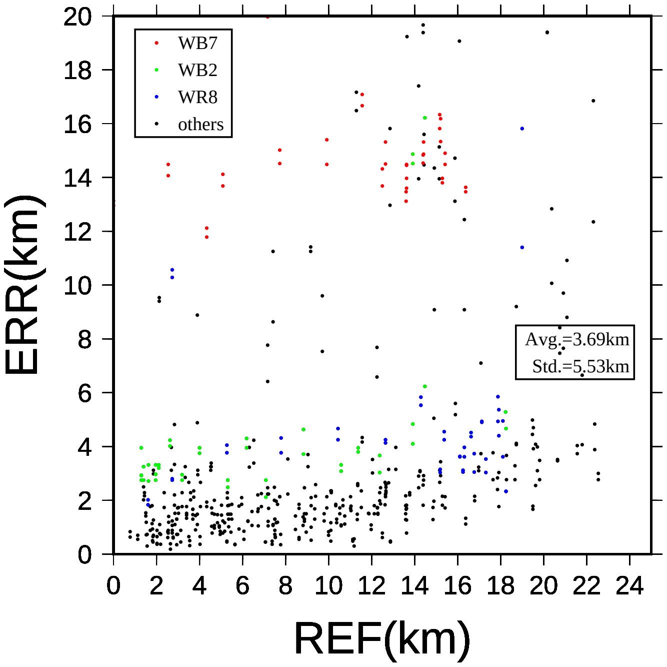

Figure 6.7: The same as Figure 6.5 but with only three stations: FITZ, COEN and INKA.

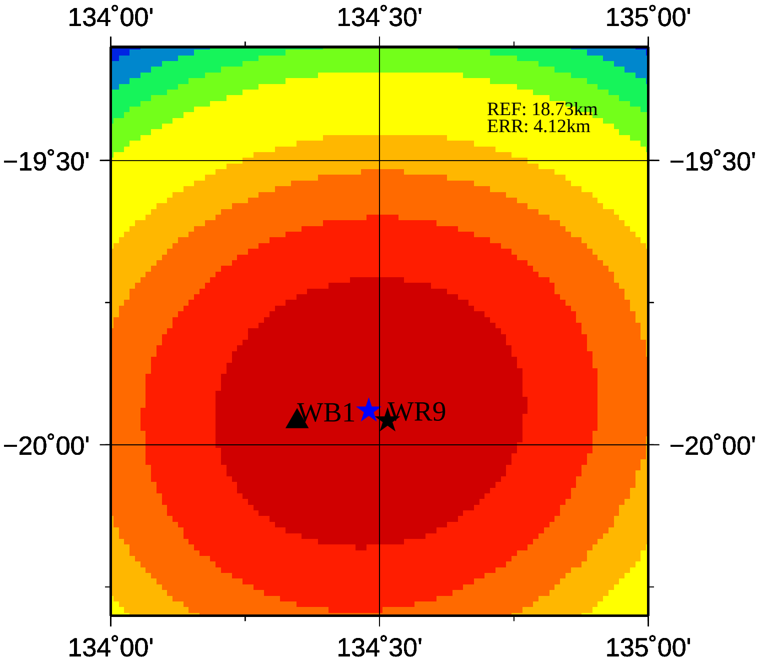

Figure 6.8: Location of WB1 (blue star) when taking WR9 (black triangular) as the reference station and using only two remote stations of WRKA and INKA.

station is located within 15 km of the virtual source, the location error is always less than 4 km. A case of using only two (Figure 6.8) well distributed stations is also tested, the location results are also good. However, when the remote stations are badly distributed (e.g., a situation in which events and reference station are situated along a line), the result is bad due to the lack of vertical resolution.

6.5 Conclusion

In this chapter, we first review three different earthquake location methods based on ambient noise. Although the Method 1 (Barmin *et al.* , 2011) gives the best earthquake location, it requires a dense seismic array within the source region, which is usually unavailable. Compared with Method 1, Method 2 does not rely on a dense array. However, it requires an accurate focal mechanism. Compared to the first two methods, Method 3 has fewer requirements and, at the same time, it has the least accuracy. When an earthquake occurs in a shallow crust and is recorded only at a few remote stations, we can use Method 3 to initially locate it before the focal mechanism is determined. When the focal mechanism is well constrained, we can then use Method 2 to better relocate it. If we intend to get an even more accurate source location, we can deploy a dense seismic array in the source region and use method 1.

Earthquake location using ambient noise can achieve high accuracy and it can be used to locate historical earthquakes as well. Using the seismic array in the central Australia, we test the accuracy of method 3 and we find that when the distribution of the remote station is good and the reference station is located less than 20 km away from the source, the location error is less than 2 km. In addition, the location error is not strongly related to the distance between the reference station and the source. Therefore, this method can be used to obtain GT2 event locations in region with sparsely distributed remote stations on condition in regions with sparesely distributed remote stations. However, this method can only be used to determine locations of shallow earthquakes.

7

Conclusion

In this thesis, we carry out a series of seismic studies on the verification and application of surface waves from ambient noise. These studies include 1) investigating the accuracy of surface wave dispersion curves at both short (10-30 s) and long (50-250 s) periods from ambient noise; 2) constructing crustal and upper mantle shear velocity structure of the entire US using broadband surface waves from ambient noise; and 3) investigating the accuracy of earthquake location based on surface wave from ambient noise. These studies altogether demonstrate the significance and accuracy of using ambient noise data for seismic studies. The specific conclusions of each chapter are listed below.

In Chapter 2, we review both the theoretic background and processing procedures for retrieving empirical Green's function (EGF) from ambient noise cross correlations. We test the effects of stacking techniques on recovering the signals contaminated by different types of noise. We find that nonlinear stacking methods (tf_PWS) can distort the original signals at periods longer than 50 s, although they can significantly improve the Signal-to-Noise Ratio (SNR). The accuracy of using nonlinear stacking methods to extract useful signals therefore still requires further investigation especially for long periods. In this thesis, we use the conventional linear stacking method to stack the Noise Cross-correlation Functions (NCFs).

In Chapter 3, we design an experiment to validate the accuracy of the short period surface waves dispersion curves (10-30 s) from ambient noise. To do this, we first choose a M5 and well-located shallow earthquake that occurred in the Sichuan Basin, China. Then we set up a broadband seismometer close to the earthquake epicenter to record ambient noise data. We compare the NCFs between this station and the remote stations with the corresponding earthquake signals. We find that the group velocity dispersion measured from EGFs at large interstation distances (>500 km) are consistent with measurements from earthquake. At shorter interstation distances, the match between noise and earthquake dispersion is good for most stations, although mismatches are observed for a few stations. The mismatch is probably caused by low SNR of NCFs or not completely diffuse noise wavefield at short distances.

In Chapter 4, we investigate the accuracy of dispersion measurements of long period (50-250 s) surface wave from ambient noise by conducting a series of comparative studies. They are 1) checking the waveform consistency between the EGF and the M6 well-located earthquake event; 2) comparing phase velocity measurements from NCFs with those from a global data set of earthquakes; 3) comparing the phase velocities from NCFs with those from earthquakes using two-station method in the central and western US. All of the three comparisons demonstrate that the waveforms and phase velocities from ambient noise data are consistent with those from earthquake data, indicating that the travel time of the long period surface wave from ambient noise is as accurate as that of the long period surface wave from earthquakes. Therefore, the long period surface wave from ambient noise can be used in tomography, and can provide more constraints on the lithospheric and asthenospheric structures.

In Chapter 5, by collecting ambient noise data from 1895 stations across the US continent, we construct a new 3-D shear velocity model purely from ambient noise from the surface down to 300 km depth beneath the USA. We extract broadband (10-150 s) surface waves phase velocities from NCFs. Then we use these dispersion curves to generate phase velocity maps at 10-150 s periods. Phase velocity dispersion curves are extracted at each grid point and inverted for 1D velocity profile using a nonlinear MCMC method. Finally, the 1D velocity models are assembled to form the final 3D model. The resulting 3D velocity model solely based on ambient noise is consistent with previous models constructed using earthquake data, confirming that long period surface wave from ambient noise can be used to study the lithospheric and asthenospheric structures of the Earth.

In Chapter 6, we test the reliability of using NCFs to calibrate earthquake location. Out of the three methods, we find that the group travel time-based method is the most suitable method when the stations are sparsely distributed. Using a small seismic array in the central Australia, we demonstrate that this method has a location error of ∼2 km, and such location error is not related to the distance between the reference station and the earthquake epicenter. However, it should be noted that we simplify the processing procedures by ignoring the epicenter depth, which needs to be taken into account for more accurate studies in the future.

Upon the verification and application of surface wave from ambient noise in this thesis, we believe that surface wave from ambient noise will continue to play an important and popular role in investigating the Earth's structure, relocating earthquake locations as well as many other seismological related fields.

The verification work we present in the thesis demonstrates that the dispersion measurements from long-period surface wave of EGFs are as accurate as those from earthquake data. These data provide us complementary data to image lithospheric and asthenospheric structures in both global or regional scales. They can improve the path coverage in tomography, especially in aseismic areas. In addition, these long-period surface waves can be extracted from station pairs with short interstation distances, like one or two wavelengths, thus providing more data to better constrain the small-scale deep structures. Joint inversion of the phase velocities from ambient noise and other geophysical data, such as gravidity, heat flow and geoid data, can provide better constraints on the thermal and compositional structure of the Earths lithosphere and asthenosphere.

However, to get high-quality long-period surface wave from ambient noise, at least two years of continous seismic records are needed. It takes a lot of computation times to calculate a large number of NCFs among thousands of (or even more) seismic stations (e.g. USArray). Luckily enough, the improvement of computational facilitie, such as clouding computation, modern CPU clusters (or GPU) will shorten the computational time. Thus, using global stations and performing teleseismic cross-correlations among them, we can obtain global phase velocity maps and furthermore use them to construct a global model of crust and upper mantle.

References

Afonso, J. C., Fullea, J., Yang, Y., Connolly, J. a. D., & Jones, A. G. 2013a. 3-D multi-observable probabilistic inversion for the compositional and thermal structure of the lithosphere and upper mantle. II: General methodology and resolution analysis. *Journal of geophysical research. Solid earth*, **118**(4), 1650–1676.

Afonso, J. C., Fullea, J., Griffin, W. L., Yang, Y., Jones, A. G., D. Connolly, J. A., & O'Reilly, S. Y. 2013b. 3-D multiobservable probabilistic inversion for the compositional and thermal structure of the lithosphere and upper mantle. I: a priori petrological information and geophysical observables. *Journal of Geophysical Research: Solid Earth*, **118**(5), 2586–2617.

Aki, Keiiti. 1957. Space and Time Spectra of Stationary Stochastic Waves, with Special Reference to Microtremors. *Bull. Earthq. Res. Inst.*, **35**(3), 415–456.

Ardhuin, Fabrice, & Herbers, T. H. C. 2013. Noise generation in the solid Earth, oceans and atmosphere, from nonlinear interacting surface gravity waves in finite depth. *Journal of Fluid Mechanics*, **716**(Feb.), 316–348.

Ardhuin, Fabrice, Stutzmann, Eleonore, Schimmel, Martin, & Mangeney, Anne. 2011. Ocean wave sources of seismic noise. *Journal of Geophysical Research: Oceans*, **116**(C9), C09004. 00111.

Ardhuin, Fabrice, Gualtieri, Lucia, & Stutzmann, Elonore. 2015. How ocean waves rock the

Earth: Two mechanisms explain microseisms with periods 3 to 300s. *Geophysical Research Letters*, **42**(3), 2014GL062782.

Asten, Michael W. 1978. Geological control on the three-component spectra of Rayleigh-wave microseisms. *Bulletin of the Seismological Society of America*, **68**(6), 1623–1636.

Backus, Milo, Burg, John, Baldwin, Dick, & Bryan, Ed. 1964. Wide-band extraction of mantle P waves from ambient noise. *Geophysics*, **29**(5), 672–692.

Baig, A. M., Campillo, M., & Brenguier, F. 2009. Denoising seismic noise cross correlations. *Journal of Geophysical Research: Solid Earth*, **114**(B8), B08310. 00020.

Bakulin, A., Mateeva, A., Mehta, K., Jorgensen, P., Ferrandis, J., Herhold, I., & Lopez, J. 2007. Virtual source applications to imaging and reservoir monitoring. *The Leading Edge*, **26**(6), 732–740.

Barmin, M. P., Levshin, A. L., Yang, Y., & Ritzwoller, M. H. 2011. Epicentral location based on Rayleigh wave Empirical Green's Functions from ambient seismic noise. *Geophysical Journal International*, **184**(2), 869–884.

Bassin, C, Laske, G, & Masters, G. 2000. The Current Limits of Resolution for Surface Wave Tomography in North America. *Eos*, **81**. 00929.

Bennett, T. J., Oancea, V., Barker, B. W., Kung, Y.-L., Bahavar, M., Kohl, B. C., Murphy, J. R., & Bondar, I. K. 2010. The Nuclear Explosion Database (NEDB): A New Database and Web Site for Accessing Nuclear Explosion Source Information and Waveforms. *Seismological Research Letters*, **81**(1), 12–25.

Bensen, G. D., Ritzwoller, M. H., Barmin, M. P., Levshin, A. L., Lin, F., Moschetti, M. P., Shapiro, N. M., & Yang, Y. 2007. Processing seismic ambient noise data to obtain reliable broad-band surface wave dispersion measurements. *Geophysical Journal International*, **169**(3), 1239–1260.

Bensen, G. D., Ritzwoller, M. H., & Shapiro, N. M. 2008. Broadband ambient noise surface wave tomography across the United States. *Journal of Geophysical Research (Solid Earth)*, **113**(May), B05306.

Bensen, G. D., Ritzwoller, M. H., & Yang, Y. 2009. A 3-D shear velocity model of the crust and uppermost mantle beneath the United States from ambient seismic noise. *Geophysical Journal International*, **177**(3), 1177–1196.

Berger, Jonathan, Davis, Peter, & Ekström, Göran. 2004. Ambient Earth noise: A survey of the Global Seismographic Network. *Journal of Geophysical Research (Solid Earth)*, **109**(Nov.), B11307.

Bettig, B., Bard, P. Y., Scherbaum, F., Riepl, J., Cotton, F., Cornou, C., & Hatzfeld, D. 2001. Analysis of dense array noise measurements using the modified spatial auto-correlation method (SPAC): application to the Grenoble area. *Bollettino di Geofisica Teorica ed Applicata*, **42**(3-4), 281–304.

Bodin, T., Sambridge, M., Tkali, H., Arroucau, P., Gallagher, K., & Rawlinson, N. 2012. Transdimensional inversion of receiver functions and surface wave dispersion. *Journal of Geophysical Research: Solid Earth*, **117**(B2), B02301.

Bondár, I., & McLaughlin, K. L. 2009. A New Ground Truth Data Set For Seismic Studies. *Seismological Research Letters*, **80**(3), 465–472.

Bondár, István, Bergman, Eric, Engdahl, E. Robert, Kohl, Ben, Kung, Yu-Long, & McLaughlin, Keith. 2008. A hybrid multiple event location technique to obtain ground truth event locations. *Geophysical Journal International*, **175**(1), 185–201.

Bonnefoy-Claudet, Sylvette, Cotton, Fabrice, & Bard, Pierre-Yves. 2006. The nature of noise wavefield and its applications for site effects studies: A literature review. *Earth-Science Reviews*, **79**(3), 205–227.

Brenguier, F., Campillo, M., Hadziioannou, C., Shapiro, NM, Nadeau, R.M., & Larose, E. 2008. Postseismic relaxation along the San Andreas fault at Parkfield from continuous seismological observations. *Science*, **321**(5895), 1478.

Bromirski, P. D. 2009. Earth vibrations. *Science*, **324**(5930), 1026–1027.

Campillo, Michel, & Paul, Anne. 2003. Long-Range Correlations in the Diffuse Seismic Coda. *Science*, **299**(5606), 547–549.

Chen, Curtis W., & Zebker, Howard A. 2000. Network approaches to two-dimensional phase unwrapping: intractability and two new algorithms. *Journal of the Optical Society of America A: Optics, Image Science, and Vision, Volume 17, Issue 3, March 2000, pp.401-414*, **17**(Mar.), 401–414.

Cirella, A., Piatanesi, A., Cocco, M., Tinti, E., Scognamiglio, L., Michelini, A., Lomax, A., & Boschi, E. 2009. Rupture history of the 2009 L'Aquila (Italy) earthquake from non-linear joint inversion of strong motion and GPS data. *Geophysical Research Letters*, **36**(19), L19304.

Claerbout, J. 1968. Synthesis of a layered medium from its acoustic transmission response. *GEOPHYSICS*, **33**(2), 264–269.

Crotwell, H. Philip, & Owens, Thomas J. 2005. Automated Receiver Function Processing. *Seismological Research Letters*, **76**(6), 702–709.

Dawson, John, Cummins, Phil, Tregoning, Paul, & Leonard, Mark. 2008. Shallow intraplate earthquakes in Western Australia observed by Interferometric Synthetic Aperture Radar. *Journal of Geophysical Research: Solid Earth*, **113**(B11), B11408.

Dias, Rafaela Carreiro, Julià, Jordi, & Schimmel, Martin. 2014. Rayleigh-Wave, Group-Velocity Tomography of the Borborema Province, NE Brazil, from Ambient Seismic Noise. *Pure and Applied Geophysics*, **172**(6), 1429–1449.

Draganov, Deyan, Wapenaar, Kees, Mulder, Wim, Singer, Johannes, & Verdel, Arie. 2007. Retrieval of reflections from seismic background-noise measurements. *Geophysical Research Letters*, **34**(4), L04305.

Duputel, Zacharie, Ferrazzini, Valrie, Brenguier, Florent, Shapiro, Nikolai, Campillo, Michel, & Nercessian, Alexandre. 2009. Real time monitoring of relative velocity changes using ambient seismic noise at the Piton de la Fournaise volcano (La Runion) from January 2006 to June 2007. *Journal of Volcanology and Geothermal Research*, **184**(12), 164–173.

Dziewonski, A. M., Chou, T.-A., & Woodhouse, J. H. 1981. Determination of earthquake source parameters from waveform data for studies of global and regional seismicity. *Journal of Geophysical Research: Solid Earth*, **86**(B4), 2825–2852.

Dziewonski, Adam M., & Anderson, Don L. 1981. Preliminary reference Earth model. *Physics of the Earth and Planetary Interiors*, **25**(4), 297–356. 06342.

Ekström, G. 2014. Love and Rayleigh phase-velocity maps, 540 s, of the western and central USA from USArray data. *Earth and Planetary Science Letters*, **402**(Sept.), 42–49.

Ekström, Göran. 2011. A global model of Love and Rayleigh surface wave dispersion and anisotropy, 25250s. *Geophysical Journal International*, **187**(3), 1668–1686.

Fialko, Yuri, Sandwell, David, Simons, Mark, & Rosen, Paul. 2005. Three-dimensional deformation caused by the Bam, Iran, earthquake and the origin of shallow slip deficit. *Nature*, **435**(7040), 295–299.

Flanagan, Megan P., Myers, Stephen C., & Koper, Keith D. 2007. Regional Travel-Time Uncertainty and Seismic Location Improvement Using a Three-Dimensional a priori Velocity Model. *Bulletin of the Seismological Society of America*, **97**(3), 804–825.

Foster, Anna, Ekström, Göran, & Nettles, Meredith. 2014. Surface wave phase velocities of the Western United States from a two-station method. *Geophysical journal international*, **196**(2), 1189–1206.

Frantti, G. E. 1963. The nature of high-frequency earth noise spectra. *Geophysics*, **28**(4), 547–562.

Frantti, G. E., Willis, D. E., & Wilson, James T. 1962. The spectrum of seismic noise. *Bulletin of the Seismological Society of America*, **52**(1), 113–121.

Friedrich, A., Krüger, F., & Klinge, K. 1998. Ocean-generated microseismic noise located with the Grfenberg array. *Journal of Seismology*, **2**(1), 47–64.

Fukao, Yoshio, Nishida, Kiwamu, & Kobayashi, Naoki. 2010. Seafloor topography, ocean infragravity waves, and background Love and Rayleigh waves. *Journal of Geophysical Research: Solid Earth*, **115**(B4).

Gilmore, Marion H. 1946. Microseisms and ocean storms. *Bulletin of the Seismological Society of America*, **36**(2), 89–119.

Godey, Stphanie, Snieder, Roel, Villaseor, Antonio, & Benz, Harley M. 2003. Surface wave tomography of North America and the Caribbean using global and regional broad-band networks: phase velocity maps and limitations of ray theory. *Geophysical Journal International*, **152**(3), 620–632.

Guo, Zhen, Chen, Y. John, Ning, Jieyuan, Feng, Yongge, Grand, Stephen P., Niu, Fenglin, Kawakatsu, Hitoshi, Tanaka, Satoru, Obayashi, Masayuki, & Ni, James. 2015. High resolution 3-D crustal structure beneath NE China from joint inversion of ambient noise and receiver functions using NECESSArray data. *Earth and Planetary Science Letters*, **416**(Apr.), 1–11.

Guo, Zhen, Chen, Y. John, Ning, Jieyuan, Yang, Yingjie, Afonso, Juan Carlos, & Tang, Youcai. 2016. Seismic evidence of on-going sublithosphere upper mantle convection for intra-plate volcanism in Northeast China. *Earth and Planetary Science Letters*, **433**(Jan.), 31–43.

Gutenberg, B. 1911. *Die seismische bodenunruhe*. University of Gottigen. Phd thesis.

Gutenberg, B. 1931. Microseisms in North America. *Bulletin of the Seismological Society of America*, **21**(1), 1–24.

Gutenberg, B. 1958. Microseisms. *Advances in Geophysics*, **5**, 53–92.

Haario, Heikki, Laine, Marko, Mira, Antonietta, & Saksman, Eero. 2006. DRAM: Efficient adaptive MCMC. *Statistics and Computing*, **16**(4), 339–354.

Hadziioannou, Céline, Larose, Eric, Coutant, Olivier, Roux, Philippe, & Campillo, Michel. 2009. Stability of monitoring weak changes in multiply scattering media with ambient noise correlation: Laboratory experiments. *The Journal of the Acoustical Society of America*, **125**(6), 3688–3695.

Haubrich, R. A., Munk, W. H., & Snodgrass, F. E. 1963. Comparative spectra of microseisms and swell. *Bulletin of the Seismological Society of America*, **53**(1), 27–37.

Herrmann, R. B., & Ammon, C. J. 2002. Computer programs in seismology: Surface waves, receiver functions and crustal structure. *St. Louis University, St. Louis, MO.*

Jarvis, A, Reuter, H. I., Nelson, A., & Guevara, E. 2008. *Hole-filled SRTM for the globe, version 4.* http://srtm.csi.cgiar.org (last accessed April 2014), CGIAR Consortium for Spatial Information.

Kanai, Kiyoshi. 1961. On microtremors, VIII. *Bull. Earthq. Res. Inst.*, **39**, 97–114.

Kedar, Sharon, Longuet-Higgins, Michael, Webb, Frank, Graham, Nicholas, Clayton, Robert, & Jones, Cathleen. 2008. The origin of deep ocean microseisms in the North Atlantic Ocean. *Proceedings of the Royal Society of London A: Mathematical, Physical and Engineering Sciences*, **464**(2091), 777–793.

Kobayashi, Naoki, & Nishida, Kiwamu. 1998. Continuous excitation of planetary free oscillations by atmospheric disturbances. *Nature*, **395**(6700), 357–360.

Koper, Keith D., Seats, Kevin, & Benz, Harley. 2010. On the composition of Earths short-period seismic noise field. *Bulletin of the Seismological Society of America*, **100**(2), 606–617.

Kustowski, B., Ekström, G., & Dziewoski, A. M. 2008. Anisotropic shear-wave velocity structure of the Earth's mantle: A global model. *Journal of Geophysical Research: Solid Earth*, **113**(B6), B06306. 00160.

Larose, Eric, Derode, Arnaud, Campillo, Michel, & Fink, Mathias. 2004. Imaging from one-bit correlations of wideband diffuse wave fields. *Journal of Applied Physics*, **95**(12), 8393–8399.

Laske, Gabi, Masters, Guy, Ma, Zhitu, & Pasyanos, Mike. 2013 (Apr.). Update on CRUST1.0 - A 1-degree Global Model of Earth's Crust. vol. 15.

Lee, A. W. 1932. The Effect of Geological Structure Upon Microseismic Disturbance. *Geophysical Journal*, **3**(May), 83–105.

Levshin, Anatoli L, Ritzwoller, Michael H, & Resovsky, Joe S. 1999. Source effects on surface wave group travel times and group velocity maps. *Physics of the Earth and Planetary Interiors*, **115**(34), 293–312.

Li, Zhenhong, Elliott, John R., Feng, Wanpeng, Jackson, James A., Parsons, Barry E., & Walters, Richard J. 2011. The 2010 MW 6.8 Yushu (Qinghai, China) earthquake: Constraints provided by InSAR and body wave seismology. *Journal of Geophysical Research: Solid Earth*, **116**(B10), B10302.

Liang, Chuntao, & Langston, Charles A. 2009. Three-dimensional crustal structure of eastern North America extracted from ambient noise. *Journal of Geophysical Research: Solid Earth*, **114**(B3), B03310.

Lin, Fan-Chi, & Ritzwoller, Michael H. 2011. Helmholtz surface wave tomography for isotropic and azimuthally anisotropic structure. *Geophysical Journal International*, **186**(3), 1104–1120.

Lin, Fan-Chi, Moschetti, Morgan P., & Ritzwoller, Michael H. 2008. Surface wave tomography of the western United States from ambient seismic noise: Rayleigh and Love wave phase velocity maps. *Geophysical Journal International*, **173**(1), 281–298.

Lobkis, Oleg I., & Weaver, Richard L. 2001. On the emergence of the Greens function in the correlations of a diffuse field. *The Journal of the Acoustical Society of America*, **110**(6), 3011–3017.

Lohman, Rowena B., Simons, Mark, & Savage, Brian. 2002. Location and mechanism of the Little Skull Mountain earthquake as constrained by satellite radar interferometry and seismic waveform modeling. *Journal of Geophysical Research: Solid Earth*, **107**(B6), ETG 7–1.

Longuet-Higgins, M. S. 1950. A Theory of the Origin of Microseisms. *Philosophical Transactions of the Royal Society of London A: Mathematical, Physical and Engineering Sciences*, **243**(857), 1–35.

Luo, Yan, Ni, SiDao, Zeng, XiangFang, Xie, Jun, Chen, Yong, & Long, Feng. 2011. The M5.0 Suining-Tongnan (China) earthquake of 31 January 2010: A destructive earthquake occurring in sedimentary cover. *Chinese Science Bulletin*, **56**(6), 521–525.

Luo, Yinhe, Xu, Yixian, & Yang, Yingjie. 2012. Crustal structure beneath the Dabie orogenic belt from ambient noise tomography. *Earth and Planetary Science Letters*, **313314**(Jan.), 12–22.

Luo, Yinhe, Yang, Yingjie, Xu, Yixian, Xu, Hongrui, Zhao, Kaifeng, & Wang, Kai. 2015. On the limitations of interstation distances in ambient noise tomography. *Geophysical Journal International*, **201**(2), 652–661.

Ma, Shuo, Prieto, Germán A., & Beroza, Gregory C. 2008. Testing Community Velocity Models for Southern California Using the Ambient Seismic Field. *Bulletin of the Seismological Society of America*, **98**(6), 2694–2714. 00028.

Malcolm, Alison E., Scales, John A., & van Tiggelen, Bart A. 2004. Extracting the Green function from diffuse, equipartitioned waves. *Physical Review E*, **70**(1), 015601.

Massonnet, Didier, & Feigl, Kurt L. 1998. Radar interferometry and its application to changes in the Earth's surface. *Reviews of Geophysics*, **36**(Nov.), 441–500.

Masters, G., Barmine, M. P., & Kientz, S. 2007. Mineos users manual. *Computational Infrastructure for Geodynamics.*

McNamara, Daniel E., & Buland, Raymond P. 2004. Ambient noise levels in the continental United States. *Bulletin of the seismological society of America*, **94**(4), 1517–1527. 00225.

Meier, Ueli, Shapiro, Nikolai M., & Brenguier, Florent. 2010. Detecting seasonal variations in seismic velocities within Los Angeles basin from correlations of ambient seismic noise. *Geophysical Journal International*, **181**(2), 985–996.

Moschetti, M. P., Ritzwoller, M. H., Lin, F.-C., & Yang, Y. 2010. Crustal shear wave velocity structure of the western United States inferred from ambient seismic noise and earthquake data. *Journal of Geophysical Research: Solid Earth*, **115**(B10), B10306.

Murphy, J. R., Rodi, W., Johnson, M., Sultanov, D. D., Bennett, T. J., Toksöz, M. N., Ovtchinnikov, V., Barker, B. W., Reiter, D. T., Rosca, A. C., & Shchukin, Y. 2005. Calibration of International Monitoring System (ims) Stations in Central and Eastern Asia for Improved Seismic Event Location. *Bulletin of the Seismological Society of America*, **95**(4), 1535–1560.

Nawa, K., Suda, N., Fukao, Y., Sato, T., Aoyama, Y., & Shibuya, K. 1998. Incessant excitation of the Earth's free oscillations. *Earth, Planets, and Space*, **50**(Jan.), 3–8.

Nishida, Kiwamu. 2011. Two-dimensional sensitivity kernels for cross-correlation functions of background surface waves. *Comptes Rendus Geoscience*, **343**(89), 584–590.

Nishida, Kiwamu. 2013. Earth's Background Free Oscillations. *Annual Review of Earth and Planetary Sciences*, **41**(1), 719–740.

Nishida, Kiwamu, Kobayashi, Naoki, & Fukao, Yoshio. 2000. Resonant Oscillations Between the Solid Earth and the Atmosphere. *Science*, **287**(5461), 2244–2246.

Nishida, Kiwamu, Montagner, Jean-Paul, & Kawakatsu, Hitoshi. 2009. Global Surface Wave Tomography Using Seismic Hum. *Science*, **326**(5949), 112–112.

Obrebski, Mathias, Allen, Richard M., Pollitz, Fred, & Hung, Shu-Huei. 2011. Lithosphere-asthenosphere interaction beneath the western United States from the joint inversion of body-wave traveltimes and surface-wave phase velocities. *Geophysical Journal International*, **185**(2), 1003–1021.

P. Moschetti, M., H. Ritzwoller, M., & M. Shapiro, N. 2007. Surface wave tomography of the western United States from ambient seismic noise: Rayleigh wave group velocity maps. *Geochemistry Geophysics Geosystems*, **8**, Q08010.

Peterson, Jon R. 1993. *Observations and Modeling of Seismic Background Noise.* USGS Numbered Series 93-322. Geological Survey (U.S.).

Pino, Nicola Alessandro, & Di Luccio, Francesca. 2009. Source complexity of the 6 April 2009 L'Aquila (central Italy) earthquake and its strongest aftershock revealed by elementary seismological analysis. *Geophysical Research Letters*, **36**(Dec.), L23305.

Porter, Ryan, Liu, Yuanyuan, & Holt, William E. 2016. Lithospheric records of orogeny within the continental U.S. *Geophysical Research Letters*, **43**(1), 144–153.

Ramirez, J. Emilio. 1940. An experimental investigation of the nature and origin of microseisms at St. Louis, Missouri Part one. *Bulletin of the Seismological Society of America*, **30**(1), 35–84.

Rhie, Junkee, & Romanowicz, Barbara. 2004. Excitation of Earth's continuous free oscillations by atmosphereoceanseafloor coupling. *Nature*, **431**(7008), 552–556. 00230.

Rhie, Junkee, & Romanowicz, Barbara. 2006. A study of the relation between ocean storms and the Earth's hum. *Geochemistry, Geophysics, Geosystems*, **7**(10), Q10004.

Richards, Paul G., Waldhauser, Felix, Schaff, David, & Kim, Won-Young. 2006. The Applicability of Modern Methods of Earthquake Location. *pure and applied geophysics*, **163**(2-3), 351–372.

Rickett, J., & Claerbout, J. 1999. Acoustic daylight imaging via spectral factorization: Helioseismology and reservoir monitoring. *The Leading Edge*, **18**(8), 957–960.

Ritzwoller, Michael H., Shapiro, Nikolai M., Barmin, Mikhail P., & Levshin, Anatoli L. 2002. Global surface wave diffraction tomography. *Journal of Geophysical Research: Solid Earth*, **107**(B12), 2335.

Ritzwoller, Michael H., Lin, Fan-Chi, & Shen, Weisen. 2011. Ambient noise tomography with a large seismic array. *Comptes Rendus Geoscience*, **343**(89), 558–570.

Rosen, Paul A., Henley, Scott, Peltzer, Gilles, & Simons, Mark. 2004. Update Repeat Orbit Interferometry Package Released. *EOS Transactions*, **85**(Feb.), 47–47.

Roult, Genevive, & Crawford, Wayne. 2000. Analysis of background free oscillations and how to improve resolution by subtracting the atmospheric pressure signal. *Physics of the Earth and Planetary Interiors*, **121**(34), 325–338.

Roux, Philippe, Kuperman, W. A., & Group, the NPAL. 2004. Extracting coherent wave fronts from acoustic ambient noise in the ocean. *The Journal of the Acoustical Society of America*, **116**(4), 1995–2003.

Roux, Philippe, Sabra, Karim G., Kuperman, W. A., & Roux, Andre. 2005. Ambient noise cross correlation in free space: Theoretical approach. *The Journal of the Acoustical Society of America*, **117**(1), 79–84.

Sabra, Karim G., Roux, Philippe, & Kuperman, W. A. 2005a. Arrival-time structure of the time-averaged ambient noise cross-correlation function in an oceanic waveguide. *Acoustical Society of America Journal*, **117**(Jan.), 164–174.

Sabra, Karim G., Gerstoft, Peter, Roux, Philippe, Kuperman, W. A., & Fehler, Michael C. 2005b. Extracting time-domain Green's function estimates from ambient seismic noise. *Geophysical Research Letters*, **32**(3), L03310.

Sabra, Karim G., Winkel, Eric S., Bourgoyne, Dwayne A., Elbing, Brian R., Ceccio, Steve L., Perlin, Marc, & Dowling, David R. 2007. Using cross correlations of turbulent flow-induced ambient vibrations to estimate the structural impulse response. Application to structural health monitoring. *Acoustical Society of America Journal*, **121**, 1987.

Saikia, C. K., Lohman, R., Ichinose, G., Helmberger, D. V., Simons, M., & Rosen, P. 2002. GROUND TRUTH LOCATIONS-A SYNERGY OF SEISMIC AND SYNTHETIC APERTURE RADAR INTERFEROMETRIC METHODS. *In: Proc. 24th Seism Res. Rev.*

Savage, Martha Kane, & Silver, Paul G. 1993. Mantle deformation and tectonics: constraints from seismic anisotropy in the western United States. *Physics of the Earth and Planetary Interiors*, **78**(3), 207–227.

Schaeffer, A. J., & Lebedev, S. 2014. Imaging the North American continent using waveform inversion of global and USArray data. *Earth and Planetary Science Letters*, **402**(Sept.), 26–41.

Schimmel, M., & Gallart, J. 2007. Frequency-dependent phase coherence for noise suppression in seismic array data. *Journal of Geophysical Research: Solid Earth*, **112**(B4), B04303.

Schimmel, M., Stutzmann, E., & Gallart, J. 2011. Using instantaneous phase coherence for signal extraction from ambient noise data at a local to a global scale. *Geophysical Journal International*, **184**(1), 494–506.

Schimmel, Martin. 1999. Phase cross-correlations: Design, comparisons, and applications. *Bulletin of the Seismological Society of America*, **89**(5), 1366–1378.

Schimmel, Martin, & Paulssen, Hanneke. 1997. Noise reduction and detection of weak, coherent signals through phase-weighted stacks. *Geophysical Journal International*, **130**(2), 497–505.

Schmandt, Brandon, Lin, Fan-Chi, & Karlstrom, Karl E. 2015. Distinct crustal isostasy trends east and west of the Rocky Mountain Front. *Geophysical Research Letters*, **42**(23), 2015GL066593.

Schuster, G. T., Yu, J., Sheng, J., & Rickett, J. 2004. Interferometric/daylight seismic imaging. *Geophysical Journal International*, **157**(2), 838–852.

Seats, Kevin J., Lawrence, Jesse F., & Prieto, German A. 2012. Improved ambient noise correlation functions using Welchs method. *Geophysical Journal International*, **188**(2), 513–523.

Shapiro, N. M., & Campillo, M. 2004. Emergence of broadband Rayleigh waves from correlations of the ambient seismic noise. *Geophysical Research Letters*, **31**(7), L07614.

Shapiro, N. M., Ritzwoller, M. H., & Bensen, G. D. 2006. Source location of the 26 sec microseism from cross-correlations of ambient seismic noise. *Geophysical Research Letters*, **33**(Sept.), L18310.

Shapiro, Nikolai M., Campillo, Michel, Stehly, Laurent, & Ritzwoller, Michael H. 2005. High-Resolution Surface-Wave Tomography from Ambient Seismic Noise. *Science*, **307**(5715), 1615–1618.

Shen, Weisen, Ritzwoller, Michael H., Schulte-Pelkum, Vera, & Lin, Fan-Chi. 2012a. Joint inversion of surface wave dispersion and receiver functions: a Bayesian Monte-Carlo approach. *Geophysical Journal International*, Nov., ggs050.

Shen, Weisen, Ritzwoller, Michael H., & Schulte-Pelkum, Vera. 2013. A 3-D model of the crust and uppermost mantle beneath the Central and Western US by joint inversion of receiver functions and surface wave dispersion. *Journal of Geophysical Research: Solid Earth*, **118**(1), 262–276.

Shen, Yang, Ren, Yong, Gao, Haiying, & Savage, Brian. 2012b. An Improved Method to Extract VeryBroadband Empirical Greens Functions from Ambient Seismic Noise. *Bulletin of the Seismological Society of America*, **102**(4), 1872–1877.

Snieder, Roel. 2004. Extracting the Green's function from the correlation of coda waves: A derivation based on stationary phase. *Physical Review E*, **69**(4), 046610.

Snieder, Roel, & afak, Erdal. 2006. Extracting the Building Response Using Seismic Interferometry: Theory and Application to the Millikan Library in Pasadena, California. *Bulletin of the Seismological Society of America*, **96**(2), 586–598.

Stehly, L., Campillo, M., & Shapiro, N. M. 2006. A study of the seismic noise from its long-range correlation properties. *Journal of Geophysical Research (Solid Earth)*, **111**(Oct.), B10306.

Stehly, L., Campillo, M., & Shapiro, N. M. 2007. Traveltime measurements from noise correlation: stability and detection of instrumental time-shifts. *Geophysical Journal International*, **171**(1), 223–230.

Stutzmann, Eléonore, Roult, Geneviève, & Astiz, Luciana. 2000. GEOSCOPE Station Noise Levels. *Bulletin of the Seismological Society of America*, **90**(3), 690–701.

Suda, Naoki, Nawa, Kazunari, & Fukao, Yoshio. 1998. Earth's Background Free Oscillations. *Science*, **279**(5359), 2089–2091.

Tan, Ying, Zhu, Lupei, Helmberger, Donald V., & Saikia, Chandan K. 2006. Locating and modeling regional earthquakes with two stations. *Journal of Geophysical Research: Solid Earth*, **111**(B1), B01306.

Tanimoto, T. 2005. The oceanic excitation hypothesis for the continuous oscillations of the Earth. *Geophysical Journal International*, **160**(1), 276–288.

Tarantola, Albert, & Valette, Bernard. 1982. Generalized nonlinear inverse problems solved using the least squares criterion. *Reviews of Geophysics*, **20**(2), 219–232.

Tibuleac, Ileana M., & Seggern, David von. 2012. Crust-mantle boundary reflectors in Nevada from ambient seismic noise autocorrelations. *Geophysical Journal International*, **189**(1), 493–500.

Trampert, Jeannot, & Woodhouse, John H. 2003. Global anisotropic phase velocity maps for fundamental mode surface waves between 40 and 150 s. *Geophysical Journal International*, **154**(1), 154–165.

Tromp, Jeroen, Komatitsch, Dimitri, & Liu, Qinya. 2008. Spectral-Element and Adjoint Methods in Seismology. *Communications in Computational Physics*, **3**(1), 1–32.

Tsai, Victor C., & Moschetti, Morgan P. 2010. An explicit relationship between time-domain noise correlation and spatial autocorrelation (SPAC) results. *Geophysical Journal International*, **182**(1), 454–460.

van Tiggelen, B. A. 2003. Green Function Retrieval and Time Reversal in a Disordered World. *Physical Review Letters*, **91**(24), 243904.

Vos, Denise de, Paulssen, Hanneke, & Fichtner, Andreas. 2013. Finite-frequency sensitivity kernels for two-station surface wave measurements. *Geophysical Journal International*, **194**(2), 1042–1049. 00001.

Walters, R. J., Elliott, J. R., D'Agostino, N., England, P. C., Hunstad, I., Jackson, J. A., Parsons, B., Phillips, R. J., & Roberts, G. 2009. The 2009 L'Aquila earthquake (central Italy): A source mechanism and implications for seismic hazard. *Geophysical Research Letters*, **36**(17), L17312.

Wapenaar, Kees. 2004. Retrieving the Elastodynamic Green's Function of an Arbitrary Inhomogeneous Medium by Cross Correlation. *Physical Review Letters*, **93**(25), 254301.

Weaver, Richard L., & Lobkis, Oleg I. 2001. Ultrasonics without a source: Thermal fluctuation correlations at MHz frequencies. *Physical Review Letters*, **87**(13), 134301.

Weaver, Richard L., & Lobkis, Oleg I. 2003. Elastic wave thermal fluctuations, ultrasonic waveforms by correlation of thermal phonons. *The Journal of the Acoustical Society of America*, **113**(5), 2611–2621.

Webb, Spahr C. 2007. The Earths hum is driven by ocean waves over the continental shelves. *Nature*, **445**(7129), 754–756.

Webb, Spahr C. 2008. The Earth's hum: the excitation of Earth normal modes by ocean waves. *Geophysical Journal International*, **174**(2), 542–566.

Whipple, F. J. W., & Lee, A. W. 1935. Notes on the Theory of Microseisms. *Geophysical Journal International*, **3**(Dec.), 287–297.

Wu, Ru-Shan. 1985. Multiple scattering and energy transfer of seismic waves separation of scattering effect from intrinsic attenuation I. Theoretical modelling. *Geophysical Journal International*, **82**(1), 57–80.

Xia, Yingjie, Ni, Sidao, & Zeng, Xiangfang. 2013. Twin enigmatic microseismic sources in the Gulf of Guinea observed on intercontinental seismic stations. *Geophysical journal international*, **194**(1), 362–366.

Xia, Yingjie, Ni, Sidao, Zeng, Xiangfang, Xie, Jun, Wang, Baoshan, & Yuan, Songyong. 2015. Synchronizing Intercontinental Seismic Networks Using the 26 s Persistent Localized Microseismic Source. *Bulletin of the Seismological Society of America*, **105**(4), 2101–2108.

Xie, Jun, Zeng, Xiangfang, Chen, Weiwen, & Zhan, Zhongwen. 2011. Comparison of ground truth location of earthquake from InSAR and from ambient seismic noise: A case study of the 1998 Zhangbei earthquake. *Earthquake Science*, **24**(2), 239–247.

Xie, Jun, Ni, Si-dao, & Zeng, Xiang-fang. 2012. 1D shear wave velocity structure of the shallow upper crust in central Sichuan Basin. *Earthq. Res. Sichuan*, **143**(2), 20–24.

Yamamoto, Hidekazu. 2000. Estimation of shallow S-wave velocity structures from phase velocities of Love-and Rayleigh-waves in microtremors. *Proceedings of the 12th World Conference on Earthquake Engineering.*

Yang, Xiaoping, Bondr, Istvn, Bhattacharyya, Joydeep, Ritzwoller, Michael, Shapiro, Nikolai, Antolik, Michael, Ekstrm, Gran, Israelsson, Hans, & McLaughlin, Keith. 2004. Validation of Regional and Teleseismic Travel-Time Models by Relocating Ground-Truth Events. *Bulletin of the Seismological Society of America*, **94**(3), 897–919.

Yang, Yingjie. 2014. Application of teleseismic long-period surface waves from ambient noise in regional surface wave tomography: a case study in western USA. *Geophysical Journal International*, **198**(3), 1644–1652. 00000.

Yang, Yingjie, & Forsyth, Donald W. 2006. Regional tomographic inversion of the amplitude and phase of Rayleigh waves with 2-D sensitivity kernels. *Geophysical Journal International*, **166**(3), 1148–1160.

Yang, Yingjie, & Ritzwoller, Michael H. 2008. Characteristics of ambient seismic noise as a source for surface wave tomography. *Geochemistry, Geophysics, Geosystems*, **9**(2), Q02008.

Yang, Yingjie, Ritzwoller, Michael H., Levshin, Anatoli L., & Shapiro, Nikolai M. 2007. Ambient noise Rayleigh wave tomography across Europe. *Geophysical Journal International*, **168**(1), 259–274.

Yang, Yingjie, Ritzwoller, Michael H., & Jones, Craig H. 2011. Crustal structure determined from ambient noise tomography near the magmatic centers of the Coso region, southeastern California. *Geochemistry Geophysics Geosystems*, **12**(2). 00017.

Yao, H., Beghein, C., & Van Der Hilst, R. D. 2008. Surface wave array tomography in SE Tibet from ambient seismic noise and two-station analysisII. Crustal and upper-mantle structure. *Geophysical Journal International*, **173**(1), 205–219.

Yao, Huajian, Hilst, Robert D. van Der, & Hoop, Maarten V. de. 2006. Surface-wave array tomography in SE Tibet from ambient seismic noise and two-station analysis I. Phase velocity maps. *Geophysical Journal International*, **166**(2), 732–744.

Yokoi, Toshiaki, & Margaryan, Sos. 2008. Consistency of the spatial autocorrelation method with seismic interferometry and its consequence. *Geophysical Prospecting*, **56**(3), 435–451.

Young, I. R. 1999. Seasonal variability of the global ocean wind and wave climate. *International journal of climatology*, **19**(9), 931–950.

Zeng, Xiangfang, & Ni, Sidao. 2010. A persistent localized microseismic source near the Kyushu Island, Japan. *Geophysical Research Letters*, **37**(24), L24307.

Zeng, Xiangfang, Xie, Jun, & Ni, Sidao. 2014. Ground Truth Location of Earthquakes by Use of Ambient Seismic Noise From a Sparse Seismic Network: A Case Study in Western Australia. *Pure and Applied Geophysics*, **172**(6), 1397–1407.

Zha, Xianjie, Fu, Rongshan, Dai, Zhiyang, Jing, Ping, Ni, Sidao, & Huang, Jinshui. 2009. Applying InSAR technique to accurately relocate the epicentre for the 1999 Ms = 5.6 Kuqa earthquake in Xinjiang province, China. *Geophysical Journal International*, **176**(1), 107–112.

Zhan, Zhongwen, Ni, Sidao, Helmberger, Don V., & Clayton, Robert W. 2010. Retrieval of Moho-reflected shear wave arrivals from ambient seismic noise. *Geophysical Journal International*, **182**(1), 408–420.

Zhan, Zhongwen, Wei, Shengji, Ni, Sidao, & Helmberger, Don. 2011. Earthquake Centroid Locations Using Calibration from Ambient Seismic Noise. *Bulletin of the Seismological Society of America*, **101**(3), 1438–1445.

Zhou, Longquan, Xie, Jiayi, Shen, Weisen, Zheng, Yong, Yang, Yingjie, Shi, Haixia, & Ritzwoller, Michael H. 2012. The structure of the crust and uppermost mantle beneath South China from ambient noise and earthquake tomography. *Geophysical Journal International*, **189**(3), 1565–1583.

Zhou, Ying, Dahlen, F. A., & Nolet, Guust. 2004. Three-dimensional sensitivity kernels for surface wave observables. *Geophysical Journal International*, **158**(1), 142–168.

Zhu, Lupei, Tan, Ying, Helmberger, Donald V., & Saikia, Chandan K. 2006. Calibration of the Tibetan Plateau Using Regional Seismic Waveforms. *pure and applied geophysics*, **163**(7), 1193–1213.